Resonant Power Converter Control for Industrial Magnetron

Nourdeen Abdulslam Abodhir, MSc (Distinction)

Submitted to the University of Nottingham for the degree
of Doctor of Philosophy

September 2016

__In loving memory of my beloved father__

ACKNOWLEDGEMENTS

ABSTRACT

High voltage DC power supplies have been used in a wide range of applications such as Radio Frequency (RF) tube drives, industrial, military, aerospace, medical, and domestic applications. Recently as a result of advances in power electronics and magnetic materials, development of compact high voltage DC power supplies has become an active area of research, and resonant power converters have been introduced as a promising solution, owing to their potential for high efficiency and high power density. Several resonant converter topologies have been investigated to be used as modulators for supplying RF tubes (i.e. Magnetrons, Klystrons, and Traveling Wave Tubes) for various applications.

The main aim of this study is to develop a control methodology for maintaining soft switching of a series resonant series loaded (SRSL) power converter based modulator for driving an industrial magnetron with variable load conditions.

This thesis considers the design of a high voltage, high frequency, compact power supply for applications where the load is variable and/or nonlinear. One particular application where this is the case is when driving an industrial magnetron with a variable output RF energy requirement. The magnetron appears to the resonant converter as a variable load which can negatively affect the efficiency of the power conversion unless control of the converter is carefully considered.

A compact power supply based on the SRSL resonant converter with an extended combined phase and frequency control is proposed. A novel control method based on three dimensional (3D) lookup tables has been developed, in order to control the load resonant converter whilst maintaining soft switching under variable load conditions. A direct quadrature (DQ) based modelling approach is used to develop a suitable model of the converter for control design. Based on the characteristics of the magnetron, an emulator prototype is also

proposed to represent the magnetron load behaviour in a low voltage laboratory environment. A detailed design and implementation procedure is presented, including the hardware design and control of the resonant power converter and the magnetron emulator.

Simulation and experimental results are provided to validate the approach and in order to demonstrate the feasibility of the proposed converter modelling approach and control strategy. A good correlation between simulation and experimental results is obtained.

Chapter 1

INTRODUCTION

1.1 Introduction

In the past decades, high voltage DC power supplies have been used in a wide range of applications including scientific research, industrial, military, aerospace, medical and domestic applications. Moreover, the use of high power radio frequency RF for mineral extraction, industrial heating and particle accelerators requires high voltage DC power supplies [1, 2]. Traditional drive systems for high power radio frequency RF applications such as magnetrons and klystrons have been based on voltage scaling using 50/60 Hz line frequency components [2, 3]. These drives utilise large transformers and filter components and can present low power quality [4, 5].

Recently, different topologies of resonant power converters have been introduced in the literature in order to optimise size, efficiency and power quality. Among these topologies are load resonant converters. Load resonant converters have been investigated for use as modulators for supplying RF tubes (Magnetrons, Klystrons, and Traveling Wave Tubes) in order to replace the traditional drive systems for RF applications [3, 6, 7]. The use of load resonant converters with a high operating frequency offers reduced size of the transformers and filter components and, as a result, high power density and compact power supplies can be developed [4, 5]. Moreover, they offer lower switching losses compared to the traditional hard switching pulse width modulation (PWM) converters due to the use of soft switching techniques. As a result, higher efficiency can be obtained [8]. In addition, high power quality can be achieved with small output filters compared to the use of traditional drive systems.[9]

Different resonant tank topologies have been introduced in [10-13] to ensure that the semiconductor devices operate with zero-current switching (ZCS) or zero-voltage switching (ZVS) for high conversion efficiency. For a given application there are many resonant converter topologies that can be applied where each one

has its own features. Good understanding of the load characteristics helps to choose the correct converter configuration. The load types could be fixed, variable, pulsed, linear or nonlinear. Many studies have been carried out by PEMC at The University of Nottingham in the design of an efficient and compact high voltage power supplies for different applications such as industrial high power Radio Frequency RF applications.

In industrial high power RF applications, high voltage DC power supplies are used to drive microwave devices such as industrial magnetrons, klystrons and travelling wave tubes. Industrial magnetrons are used in a wide range of applications such as in production of food-stuffs, chemicals, textiles, paper and wood materials [14]. Recently, as a result of environmental regulations and the high costs of industrial heating processes using fossil fuels, significant research has been carried out in the application of industrial magnetrons in these areas.

The high voltage DC power supplies in these applications are better known as modulators. These modulators can be divided into two types namely Pulse modulators and Continuous Wave (CW) modulators [15, 16] . Pulse modulator can produce a high power pulse while a CW modulator continuously supplies power to the microwave device. The latter could be based on a load resonant converter in an effort to achieve a compact and efficient CW modulator. There are several challenging issues related to the design of the resonant converters. One of these challenges is maintaining soft switching when the load is variable or nonlinear.

In this study a high voltage DC power supply is designed to supply a magnetron with variable load conditions. Since the quality of the produced RF energy is a function of magnetron's Anode current, a controllable current source can be formed using a series resonant series loaded (SRSL) topology [14]. One of the main advantages of the SRSL converter is that the series resonant capacitor blocks any generated DC offset; and consequently it prevents high voltage (HV) transformer saturation. Another advantage of SRSL converter in contrast to series resonant parallel loaded (SRPL) topology is that the device current varies in time with the output power, reducing the conduction losses at low power and improving efficiency. Moreover, on the output side a simple capacitive filter is

sufficient; avoiding some potential undesirable conditions associated with second order filters such as the transfer of significant energy into the tube when it stops conducting abruptly.

A combined frequency and phase shift modulation (CFPM) has been developed in [7] to control the load resonant converter whilst achieving soft switching with variable voltage gains, but assuming constant quality factor Q. The CFPM is based on the derivation of a relationship between the converter voltage and operating frequency using the fundamental mode approximation. This relationship is nonlinear and can be approximated using a 4th order curve fit in order to minimise computational effort. However, under variable load conditions, such as a magnetron with variable output RF energy requirements, the relationship becomes inaccurate as a result of the assumption that Q is constant in its derivation. This assumption means that it can be difficult to ensure zero current switching (ZCS) via phase and frequency control when the load varies. The variable output RF energy requirements are seen by the converter as a variable resistance (variable Q) which could negatively affect the converter control and the soft switching scheme.

With the aim of overcoming the aforementioned limitations, a novel control method based on three dimensional (3D) lookup tables and surface fitting approximations has been developed in order to control the load resonant converter whilst maintaining soft switching under variable load conditions. In this method the soft switching points for Q ranging from 2 to 5 are pre-calculated and represented in a 3D lookup table. Hence, during the converter modulation, the soft switching point can be tracked by obtaining the online value of the variable load resistance and the control actuation signal. The modelling process plays a very important role in the dynamic analysis and the design of resonant converters. Several techniques to model such resonant converters have been proposed in scientific literature. Based on the overview in [3, 17, 18] a direct quadrature rotation frame (DQ) model has been developed for the SRSL converter. The state space description of the resonant converter has been created and the system transfer function was obtained for control design.

The novelty in this study is that a variable load converter is designed which is able to achieve ZCS over a range of values of Q (2 to 5). This is vital when the magnetron is used in heating applications where the RF output power may vary. This study presents the control strategy and modelling technique for maintaining soft switching of the SRSL converter driving a magnetron with variable load conditions. Moreover, the closed loop control aspects are considered in this study. The overall objective of the research is to develop a potentially compact power supply with high efficiency and high power density to drive the magnetron with variable load. The SRSL power converter design and its control strategies are introduced. A novel method is developed and validated in order to ensure that the SRSL DC-DC resonant converter maintains soft switching under variable load conditions. Simulation and experimental results are provided to demonstrate effectiveness of the novel method.

1.2 Thesis Outline

Chapter two provides an overview of magnetron characteristics and the principles of operation. Magnetron applications are also discussed.

Chapter three presents an overview of radio frequency modulators. This chapter focuses on load resonant converters which are used to produce high voltage power supplies. Moreover, the previous work in this area is discussed to address the features of each applicable topology.

Chapter four presents the proposed DC-DC SRSL resonant converter. The advantages of the proposed DC-DC SRSL resonant converter are highlighted. Then, the power converter is analysed and designed.

Chapter five presents the modulation methods and the simulation results. A novel variable Q based CFPM modulation is introduced to control the proposed converter and to apply the zero current switching (ZCS) while the load varies. Detailed simulation results, in PLECS, are used to investigate the approaches considered.

Chapter six presents details of the DQ modelling technique for the proposed converter. The DQ model for the resonant converter is developed and state-space representations are formulated. Based on this, the system transfer function is obtained, which is utilised in closed loop control design. A suitable PI controller is designed based on the transfer function obtained. Two reduced scale

power electronic prototypes are proposed to emulate the magnetron characteristics in order to avoid the safety issues associated with using real magnetrons in the power electronic laboratory. Detailed simulation results, in PLECS, are used to validate the approach considered.

Chapter seven presents the entire experimental system, including power converters, control platform and resonant tank, which is used to verify the feasibility of the converter topology and the control methodology.

Chapter eight presents the experimental results obtained during the experimental validation of the proposed control.

Chapter nine concludes the research work undertaken and discusses the possible further developments.

1.3 The Project Objectives

The aim of this project was to study the control of a series resonant converter when driving variable load. Thus, this project considered the following objectives:

- Develop a high DC voltage, high power and variable load resonant power converter for high voltage DC application.

- Highlight the issues associated with the use of these new approaches in applications with variable load characteristics.

- Design a novel control strategy for the SRSL DC-DC resonant power converters in order to maintain soft switching under variable and nonlinear loads (industrial magnetrons).

- Emulate the magnetron characteristics by using power electronic converters.

- Investigate the suitability of the novel control strategy by simulation and experiment verification.

1.4 Contributions

The main contributions to knowledge for this work are

- Compact and efficient Converter topology for supplying the industrial magnetron.

- A novel variable Q based CFPM modulation technique for variable load applications.
- DQ modelling technique for SRSL converter.
- Reduced scale laboratory magnetron emulator for verifying the novel modulation technique and the feedback control strategy in a low voltage power electronic laboratory.

Chapter 2

MAGNETRONS AND INDUSTRIAL APPLICATIONS

2.1 Introduction

A magnetron device can be defined as a device that converts electrical energy in form of a direct current into high frequency electromagnetic energy of a certain wavelength. Radio waves and microwaves are forms of electromagnetic energy that are collectively described by the term "Radio Frequency" [19]. Magnetrons were invented before the second world war for radar applications [19]. These magnetrons were capable of generating many kilowatts of electromagnetic power at low frequencies. In the post war years, magnetrons have been extensively developed to cover a very wide frequency range in a wide range of power outputs [20].

Magnetrons are used not only for ground, sea and airborne radar systems but also for linear accelerators and industrial heating appliances [21]. Moreover, the continuous wave (CW) magnetrons have become common in their use in domestic microwave ovens. Recently, the industrial magnetron has become increasingly important in the production of food-stuffs, chemicals, textiles, paper and wood materials. It can be also used in making certain applications more environmentally friendly. Recently, due to the high oil prices and environmental regulations, research on efficient, high power, industrial magnetrons has increased [22]. Over recent years, magnetrons have gradually become lower cost, smaller, lighter, less bulky and more efficient devices compared to those invented during the war [20].

The following sections will introduce the industrial magnetron. First, the structure and characteristics of the industrial magnetron will be introduced, including the magnetron principle of operation and the required hardware to drive the industrial magnetron. The performance chart for an Industrial magnetron will then be considered. Finally, a review of the applications for an industrial magnetron will be made.

2.2 Magnetron Operation

2.2.1 Main Components and Principle of Operation

A cross-sectional view of an industrial magnetron is illustrated figure 2.1. The magnetron consists of the following components:

• A cylindrical heated cathode which produces electrons used in the energy conversion process.

• Concentric anode which surrounds the cathode, the main function of the anode is to control the frequency and convert direct current into *RF* energy. The anode comprises an array of radial slots forming resonators turned to the desired operation frequency.

• A sidearm, which is used to support the cathode and heater structures and interfaces with external electrical inputs.

• The output is a probe antenna or slots coupled to the resonator sealed by a microwave transparent material to deliver the RF power from the anode to the external load.

• A filament power supply is used to heat the cathode to the correct temperature for electron emission.

• A magnet power supply to produce a magnetic field aligned axially to the anode-cathode assembly. It is used to control the electron trajectory.

• A high voltage supply applied between the anode and the cathode. It is used to generate an electric field between the anode and cathode.
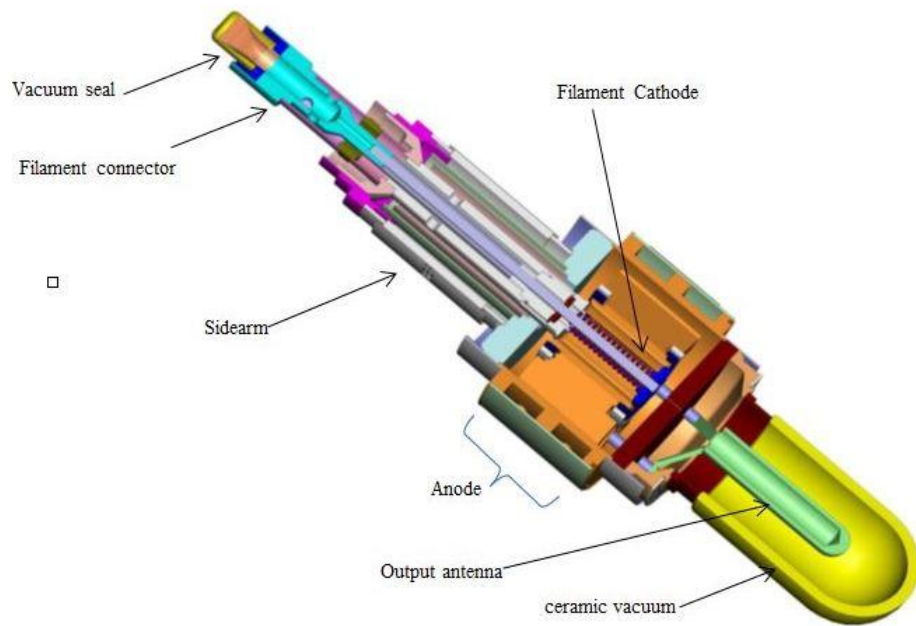
Figure 2.1 a cross-sectional view of an industrial magnetron [e2v]

The magnetron function is based on converting the potential energy of an electron cloud near the cathode into microwave energy.

In operation, a high current is injected by the filament power supply, which heats up the cathode to produce a cloud of electrons in the interaction region between the anode and the cathode as shown in figure 2.2.
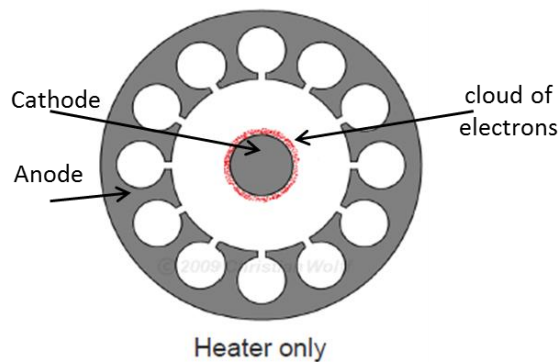
Figure 2.2 an electron cloud in interaction region [e2v]

These electrons are drawn from the heated cathode by the electric field produced from the high voltage DC supply. Due to the presence of the magnetic field, the electrons will be travelling to the anode in a spiral path instead of radial path and will oscillate at a frequency which is determined by the number and the dimensions of the cavities in the anode as shown in figure 2.3.
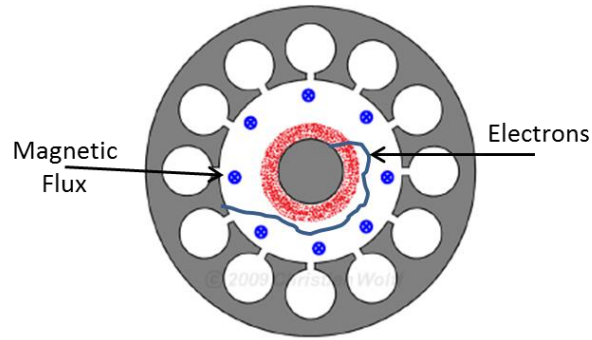
Figure 2.3 electrons travelling to the anode in a spiral path [e2v]

 Due to the current around cavity and the electric fields between vanes as shown in figure 2.4, microwave energy is generated and transmitted from inside through the probe antenna.

oscillating magnetic and electric
fields produced in the cavity

electric fields between vanes
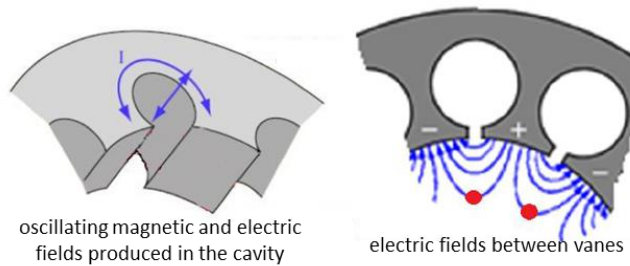
Figure 2.4 the current around cavity and the electric fields between vanes [e2v]

A waveguide is utilised to carry this microwave power to the microwave heating system or other *RF* load [23]. Figure 2.5 shows a detailed structure and operation of a magnetron.
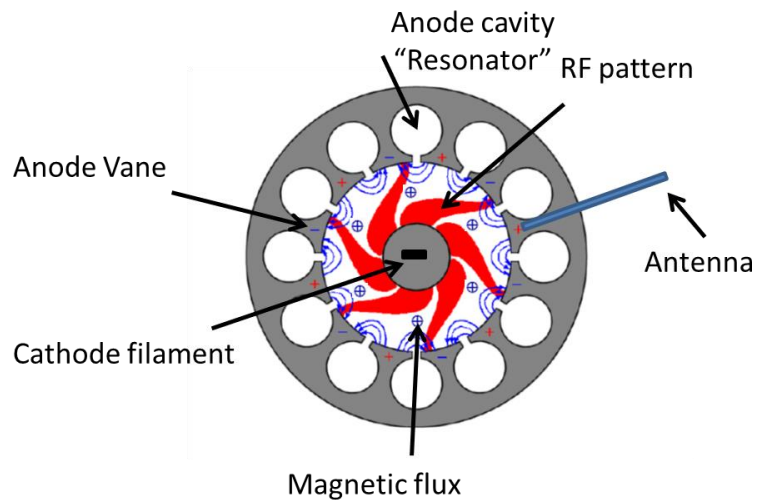
Figure 2.5 detailed structure and operation of a magnetron [e2v]

For a given magnetic field, the voltage at which the electron just touches the anode is called Hull's cut-off voltage or knee voltage.

The most desired mode of operation for the magnetron is called the π-mode. The number of repeats of the *RF* pattern (shown in figure 2.5) around the structure is known as the mode number. For example, in the 12 segment resonator system (such as that depicted in figure 2.5) there are 1, 2,3,4,5 or 6 repeats (or spokes) of the *RF* pattern; the mode which has 6 of *RF* repeats is called the π-mode. The other *RF* pattern at other frequencies have 5, 4, 3, etc. repeats: the first of these is called (*π-1*)-mode and it is undesired, as are all the rest. In the π-mode the *RF* voltages on the adjacent vanes are 180° or π out of phase [23, 24].

2.2.2 Electrical Inputs

Figure 2.6 shows three different kinds of power supplies which are required in order to drive the industrial magnetron, including the filament power supply which is required to heat the cathode to correct temperature for electron emission, the magnet power supply which is required to produce a magnetic field to control the electron trajectory and the high-voltage power supply which is used to generate the electric field required to produce high-power microwaves [14, 22]. In this study, the high voltage DC power supply is considered.
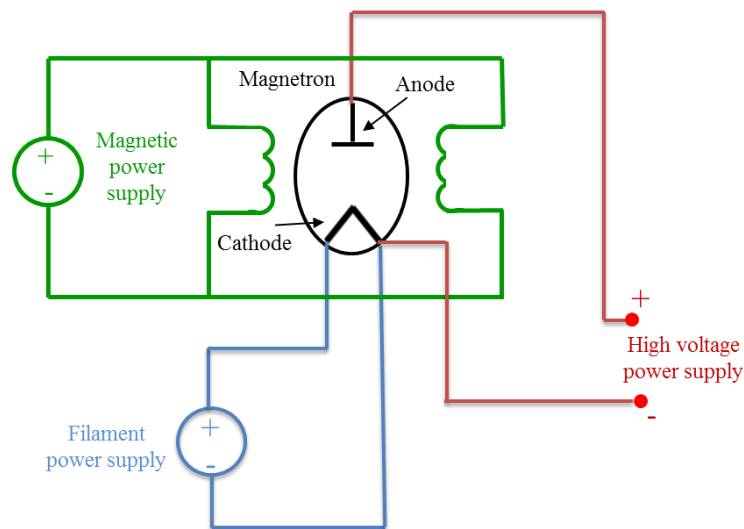
Figure 2.6 the input power supplies for the magnetron [14, 22]

Magnetrons are microwave energy generators. ''The heart of any microwave energy generator is a high voltage DC power supply'' [25]; it is used to generate microwave energy. For most commercial magnetrons, which are used in

microwave ovens, the required high voltage is provided by a half wave doubler's power supply circuit [26]. In this type of circuit a capacitor and diode combination is used to double the voltage supplied by a transformer. For industrial microwave ovens or magnetrons, a number of techniques are utilised to produce the high electric field required for power operation [20].

The first technique; variable voltage supply, comprises a line frequency transformer driving a bridge rectifier to provide the anode EHT (Extra High Tension or high voltage DC supply) via a smoothing inductor. The anode current in this technique is stabilised by anode voltage control. Adjusting the anode voltage is possible by using a variable transformer ratio or thyristor-phase-angle control [20] as shown in figure (2.7). The variable voltage supply operates at the line frequency which means these supplies are large and bulky. Moreover, crowbar protection systems are required to protect the magnetron from damage in the event of a tube fault. The crowbars limit the amount of energy that can be delivered from the filter assembly into the tube in the event of the fault [27].
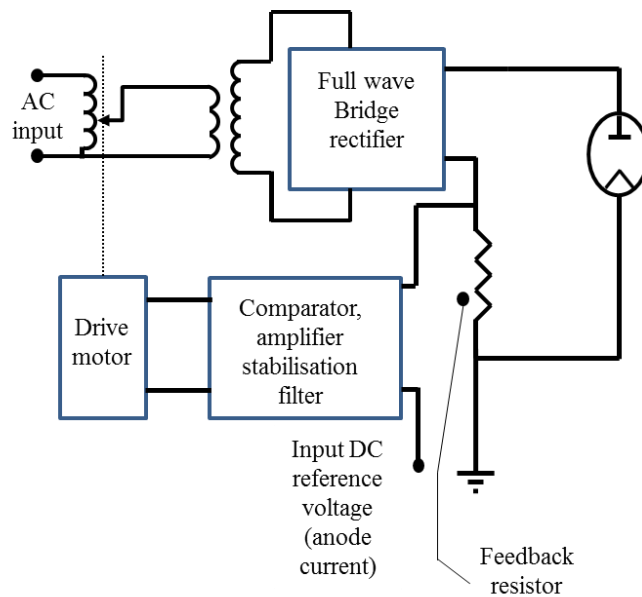
Figure 2.7 variable voltage supply technique

The second technique; variable magnetic field supply , this power supply is for magnetrons of more than 15kW rated power with electromagnets [20] , where the magnetic field of the magnetron is adjusted to control the output power. This kind of supply has a convenient control system because the control requires a

low power circuit only. However, the EHT produced by this magnetron supply is still achieved using line frequency transformers. Consequently the risk of damage under fault conditions at a high power rating rises significantly due to the use of very large transformers and high voltage energy storage [7].

The third technique uses modern switched mode power supply methods in an effort to reduce the size of magnetic components. This technique has been enabled by recent advances in power electronics and magnetic materials. With a high switching frequency the energy dissipated in the magnetron under fault conditions is limited due to the low stored energy in the switch-mode converters. Moreover, the power supply becomes smaller due to the use of the high frequency instead of the line frequency components [7]. Resonant converters are considered in this work in order to make the advantages of the high frequency operation with lower switching losses. This will be detailed in later chapters.

2.2.3 Industrial Magnetron Performance Characteristics

"The performance chart is the most useful way to present the operating characteristics of a magnetron" [24]. It is crucial to ensure that magnetrons are operated within the limits of the specifications given by the magnetron manufacturer. Failure at control may result in damage to the magnetron. Figure 2.8 shows a performance chart for a typical e2v Technologies BM100L Series Continuous Wave Magnetron. The chart shows a number of curves of voltage against the current at different magnetic fields. Constant power and efficiency contours are superimposed on the curves [24].
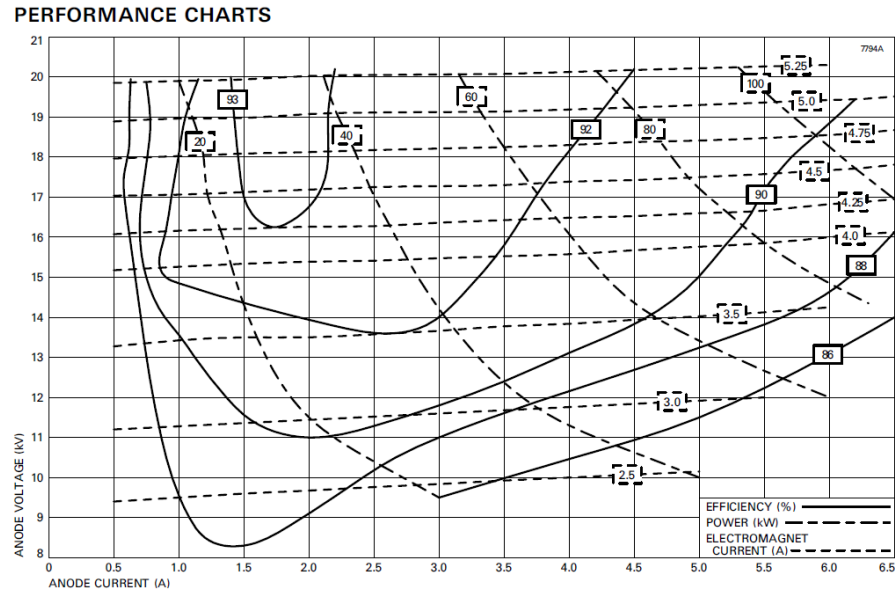
Figure 2.8 Magnetron I-V characteristic [24]

"It has been customary to plot the anode voltage in kilovolts along the ordinate and anode current in amperes along the abscissa" [19] . On such a graph the lines of constant magnetic field (in this performance chart, the magnetic field is represented by the term electromagnet current in Amperes) appear as more or less parallel lines which slope upward to the right [19, 24].

If the magnetron is operated at a constant electromagnet current, say 5.0 Amps, the relations between anode voltage and anode current are given by points on the electromagnet current = 5.0 Amps line (at 19.2 kV, the anode current drawn will be 4.5 A). Lines of constant power output are plotted on the same chart. Thus at 19.2kV anode voltage and 4.5A anode current, the power output is 80kW. In addition, if the anode voltage is decreased from 19.2kV to 19 kV at a constant electromagnet current (5.0 Amps), the anode current will be experience a relative decrease (from 4.5A to 1.5A). This characterises the magnetron as a low dynamic impedance.

From the figure 2.8 it can be seen that the same power can be obtained at 16kV and 5.4A with a magnetic current a little higher than 4.0 Amps.
Contours of constant efficiency are also shown in figure 2.8. Increasing the anode current while keeping magnetic field constant results in a decrease in efficiency. However, increasing the magnetic field at constant anode current could increase the efficiency. In both cases the output power increases but the

former case decreases the efficiency and the latter increases it. Moreover, in these cases (changing the magnetic field at constant anode current or changing the anode current while keeping the magnetic field constant) the magnetron is ''seen'' by the modulator as a variable resistive load. In this work, the modulator used to drive the magnetron is a load resonant converter. Conventional modulation techniques cannot ensure soft-switching operation under variable load conditions, this will be discussed in more detail in later chapters. The efficiency (η) with which the magnetron converts the input power into *RF* power is given by

$$\eta = \frac{(inputpower - losses)}{inputpower} \tag{2.1}$$

"The source of losses is the bombardment of the anode by the electrons and also is the circulating *RF* currents which produce I^2R losses in the copper and other materials" [19].

2.3 Magnetron Applications

The magnetron is a microwave generator. Recently, industrial microwave applications have increased dramatically due to their potential use in certain areas such as the food processing, coal processing, extraction of oil from oil sands, waste processing, minerals processing, activated carbon regeneration and oil-contaminated drill cuttings [28, 29]. Microwave energy is extremely efficient in the selective heating of materials so less energy is wasted. This is a clear advantage that microwave heating has compared to the conventional methods (bulk heating in furnaces).

In food processing, industrial microwaves are commonly used in pasteurization, sterilization, drying, tempering meat or fish blocks and precooking meat patties [30]. The main advantages of using the industrial microwaves in these applications are that they "shorten processing times, reduce floor space, and improve product quality compared to conventional methods" [31].

It is well known that coal is most prevalent fossil fuel in the world. It is used to fire power plants to generate electricity. Coal is also a very important resource in production of steel. Recent research reports that improving the efficiency of

coal utilisation can make a significant contribution to world carbon dioxide CO_2 emission reduction. Industrial microwaves are introduced for pre-treatment as a potential upgrading process to remove minerals or water prior to combustion, or to improve grind ability, thus saving on energy costs and reducing harmful emissions [32].

Industrial microwaves can also be used to extract the oil from oil sand. This process can also be upgraded to remove organics from contaminated soils. In both cases, microwaves are used to heat the water phase selectively and convert it to steam, this acts as an in-situ mass transfer media that strips or desorbs the hydrocarbons from the host solid. Energy is only required to heat the water phase, and is not required to heat the entire bulk material thus saving energy. Heating water phase selectively requires only one-fifth of the energy of their conventional heating counterparts [33].

In waste processing, microwave heating has significant advantages in the treatment of many mixed wastes. This includes the ability to treat wastes in situ, enhance chemical reaction, and improve safety, (example, including reduction in personnel exposure to potentially hazardous chemicals or materials for processing and disposition). Moreover, microwave heating can be selective and is a rapid and flexible process that can also be made remote. It is a cleaner energy source compared to conventional systems. Microwaves are applicable in many sludge treatment processes and sterilisation of hospital wastes [28].

In mineral processing, various applications of microwave heating have been proposed. For example, the reduction of grinding costs through a phenomenon known as thermally assisted comminution. This phenomenon is the heating and quenching of ores to reduce lattice strength, therefore, reducing grinding costs. Conventionally, thermally assisted liberation of minerals requires large heat inputs. Using microwave heating in mineral processes has several attractions including that less energy is wasted, only responsive phases within the material are heated, and there is no need to heat the material to high temperatures. It allows selective material heating, energy transfer, not heat transfer, non-contact heating, volumetric heating and higher level of safety and automation compared to traditional thermally assisted comminution [28].

Drilling activities carried out in the exploration and extraction of oil and natural gas result in oil-contaminated drill cuttings. The drill part is lubricated using drilling fluids known as the 'muds'. Previously, the separated cuttings were discharged directly into the sea without further treatment. This caused hydrocarbon contamination which lead to the degradation of the marine environment around the platform. The UK's Environmental Legislation now stipulates that oil levels in the cuttings must be <1% by weight before discharge can take place. In contrast, the limits for discharge in the Gulf of Mexico are 5%. Drill cutting samples obtained from the North Sea which were produced using oil-based muds (OBM) can contain 5-15% oil. These cuttings require further treatment before they can be disposed. An offshore treatment process for the cuttings has become desirable due to recent landfill directives and concerns about transporting these cuttings to shore. A technology identified as a potential candidate to achieve this is microwave treatment [34]. The applied microwave power and the residence time within the microwave cavity determine the effectiveness of the removal of the contaminated oil. The residual oil levels can be reduced to below the threshold of 1%, thus allowing for environmental discharge. These oil levels can be further reduced to below 0.1% under continuous microwave heating conditions. When compared to equivalent batch processes, the continuous microwave heating conditions has shown that it is capable of producing higher levels of remediation using lower energy inputs, thus making it more efficient[34].

2.4 Conclusions

In this chapter, the principle of operation of the industrial magnetron and its performance chart were discussed. Furthermore, three types of electrical inputs which are used to drive the industrial magnetron (filament power supply, magnetic power supply high voltage power supply) were introduced. The high-voltage power supply which is required to generate a high electric field in the magnetron was discussed. This gives a good idea about the types of power supply required to drive the industrial magnetron for heating applications. From the magnetron performance characteristics it can be seen that in order to fulfil some requirements such as improving the efficiency or to work at different power conditions the magnetron will be seen by power supply as a variable

resistive load which will make it difficult for the resonant power supplies to drive the magnetron under these conditions without excessive losses.

In addition, in this chapter some microwave heating applications were discussed. The adoption of microwave heating applications could potentially reduce processing time and also reduce the amount of energy consumed in these processes. Microwave assisted processes do not benefit solely from a reduced energy consumption (input) and reduced processing times. They can also potentially benefit from the production of an increased yield, thus increasing efficiency (minimum input - maximum output). Moreover, when utilised, microwave assisted processes are much more environmentally friendly when compared to the processes which are currently in use, thus making them more environmentally compatible. These benefits make this technology an ideal candidate for further development.

Chapter 3

CONVERTERS FOR RF TUBES

3.1 Introduction

Recently, radio frequency RF tubes have been widely used in both scientific research and industry [35]. Some scientific research applications include work at scientific research centres such as Los Alamos National Laboratory (LANL), European Organization for Nuclear Research (CERN) and Oak Ridge National Laboratory (ORNL) and have focused on high energy physics experiments and particle physics research.

As previously discussed in chapter 2, industrial applications of high power RF include the use of microwaves for food processing, extraction of minerals and treatment of oil-contaminated drill cuttings. A High Voltage Power Supply is required to convert standard AC distribution voltages to regulated high voltage in order to power the RF tubes (which include Magnetrons, Klystrons, Inductive Output Tubes (IOT) and Travelling Wave Amplifier (TWA)). These high voltage power supplies are known as modulators [35].

3.2 Radio Frequency Modulators

Generally, there are two principle types of *RF* modulators: Pulse modulators and Continuous Wave (CW) modulators [15, 16]. The type of modulator used is dependent on the application that it will be used for. For example, the primary applications for pulsed RF tubes are radar and medical linear accelerators while CW modulators for CW magnetrons are typically used in industrial drying and heating applications requiring CW microwave energy [36].

3.2.1 Traditional Pulse Modulators

Pulse modulators are used to produce high-voltage, high-power pulses in small durations (milliseconds) [37]. A conventional pulse power modulator approach is shown in figure 3.1. It comprises of large inductive and capacitive filters to smooth the rectified voltage which is supplied from a line frequency high

19

voltage transformer. Moreover, Pulse transformer is required to match the load voltage specifications and isolation requirements. The size of this transformer is proportional to the pulse length. In order to ensure the output pulse remains flat as energy is removed from the capacitor bank an additional "bouncer" circuit is required [27]. In addition, crowbars are needed for protection in order to limit arc damage in the event of a tube fault [7].
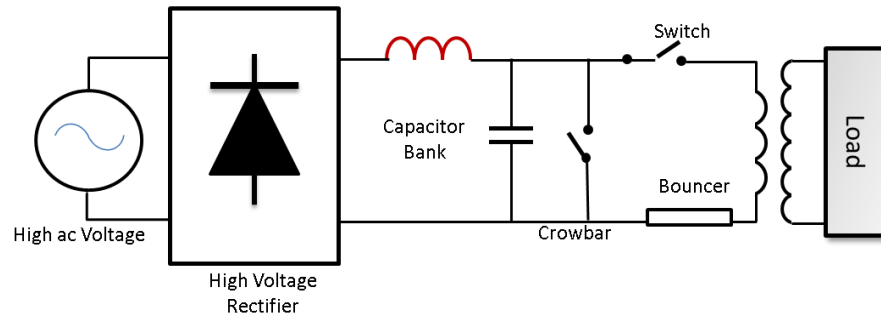
Figure 3.1 conventional pulse power modulator general scheme

One of the main advantages of this topology is that these pulse modulators have been used for decades, many potential sources of fault have already been identified and remedied, and it is known to be reliable. However, this approach uses the line frequency technique which requires very large magnetics and filter components. Furthermore the current waveform drawn from the grid by the pulse modulator is poor as the converter principally operates as a line frequency rectifier. In addition, harmonic filters and traps are required in order to meet a grid connection code, such as Engineering Recommendation G5/4, at the power levels considered [38].

3.2.2 Traditional Continuous Wave (CW) Modulator

Continuous Wave modulators are typically used as the *RF* source for particle accelerators. In the RF system, the power supply reliability is important to the overall RF system availability, and the efficiency of the modulators is significant in determining the operating cost of the system. The cost of the CW RF modulators is the single largest percentage of the total RF system cost [15].
The CW modulator is traditionally used to convert the line frequency supply voltage to regulated high voltage DC [39]. An example of the conventional CW modulator is shown in figure 3.2. The CW modulator comprises of a line

transformer driving a bridge rectifier via a large DC filter assembly which provides the filtering of the output DC voltage, moreover, a pair of thyristors are used to provide variable supply voltage by controlling the phase angle of the firing angle [20].
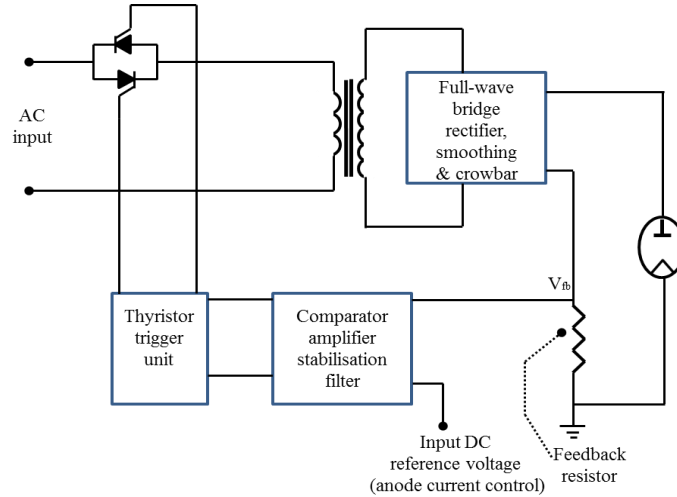
Figure 3.2 conventional CW modulator

This approach has been used for many years to generate high voltage DC. It is simple to design and reliable. However, the transformer uses the line frequency and consequently the filter assembly (inductive and capacitive filter) and the transformer are large. Additional protection circuits such as crowbars are required in these kinds of converters for protection in the event of a tube fault. Crowbars are used to limit the amount of energy discharged by the filter assembly into the tube in the event of a fault [27].

3.3 Development of RF Modulators

Following on from previous sections, it is important to note that the conventional topologies of both pulse and CW modulators are suffering from several disadvantages where low frequency AC transformers and rectifiers are used. This results in a large reactive power component requirements. Moreover, very large transformers are required. Additional protection of the load under fault conditions is required due to the use of high energy storage components; the use of a crowbar is an example of this protection.

In recent years, various approaches have been proposed in order to develop high performance and cost effective RF modulators [40]. The development of high

frequency resonant inverter type switching mode DC-DC power conversion circuits and systems has generated an interest for their use in RF modulators, this is due to advances in power semiconductor switching devices, such as IGBTs, together with advances in high frequency passive circuit components [25].

As a result of industry pressures for increased controllability and smaller footprints for RF source modulators, new topologies based on high frequency resonant circuits have been proposed for pulse and CW applications [38, 39, 41, 42]. These topologies offer many benefits including:

-   Significant reduction in the footprint of the modulator hardware.
-   A dramatic reduction in the volume of magnetic material required to transfer energy at the same power.
-   Possibility to operate the semiconductors at high frequency without compromising the converter efficiency when resonant soft switching circuits are used.
-   Crowbars are not required due to the smaller filter components used resulting in a reduction in the stored energy.
-   Capability to meet more demanding load specifications.

3.3.1 Resonant Power Converters

It is well known that conventional hard switched circuits (pulse width modulation (PWM) converters) produce switching loss which is exacerbated with the increase of the switching frequency. Resonant converter techniques attempt to eliminate switching loss by using the properties of resonant circuits to arrange for switching device voltage or current to be zero at the instant of switching. Resonant converters can be classified into two main groups: resonant switch and load resonant converters.

The first main type, resonant switch converters, involve the use of an additional resonant network associated with each switch to give (ZVS) or (ZCS) [43, 44]. This family of converters have been used to improve efficiency and reduce the size of low power DC-DC converters [5].

The second main type is load resonant converters. In these converters, the resonant network is used to couple the power converter with the load and it is inserted between the inverter and the load in a series connection, a parallel connection or in a combination series and parallel connection scheme. The oscillating load voltage or current waveforms creates soft switching conditions for the main converter switches[5]. Over the past 30 years, load resonant converters have been considered at powers less than 1kW, however, recently these converters have been considered for use in high power, high voltage applications [38].

A block diagram of a high voltage DC power supply derived using a resonant circuit is shown in Figure 3.3. It is formed by cascading a load resonant DC-AC inverter and a high frequency rectifier, where the H-Bridge excites the resonant circuit with a high frequency square-wave waveform. Between the resonant tank and the output rectifier arrangement, a high frequency transformer can be included for isolation and voltage scaling. A rectifier and filter are utilised to obtain a filtered DC output.
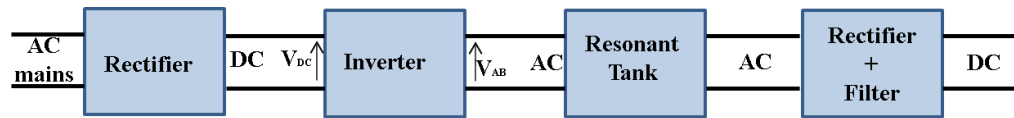
Figure 3.3 basic structure of a load resonant dc-dc converter

DC-DC load resonant converters have two main topologies, series resonant series loaded (SRSL) and series resonant parallel loaded (SRPL). Hybrid versions of these two is also often proposed. Since load resonant converters being used in resonant modulators, the following sub-sections consider the main DC-DC load resonant topologies in more detail.

3.3.1.1 Series Resonant Series Loaded Converter

A SRSL DC-DC converter is shown in figure 3.4. This topology consists of a series resonant tank (It is named a resonant "tank" because the energy oscillates between L and C) with quasi-square input voltage which is derived from the H-Bridge inverter. A high frequency transformer is connected between the converter and the output stage (rectifier, filter and DC load) for scaling and isolation. In this configuration the load appears in series with the resonant

"tank". Resonant frequency, ω_o, and resonant circuit quality factor, Q, are two important quantities which can be derived for this circuit. Here, the resonant frequency is described as the frequency at which operation changes from capacitive load to inductive load for the SRSL circuit, while the quality factor Q is defined as the ratio of energy stored in the tank to that delivered to the load resistance of the circuit. If Q is chosen relatively high then the tank currents will be almost perfectly sinusoidal, however, large Q indicates significant energy storage in the resonant tank and therefore large tank components. On the other hand, if low Q is selected the tank currents will not be perfectly sinusoidal [45] making circuit analysis difficult. Thus, for power converters, a Q range 3-5 is preferred [38].
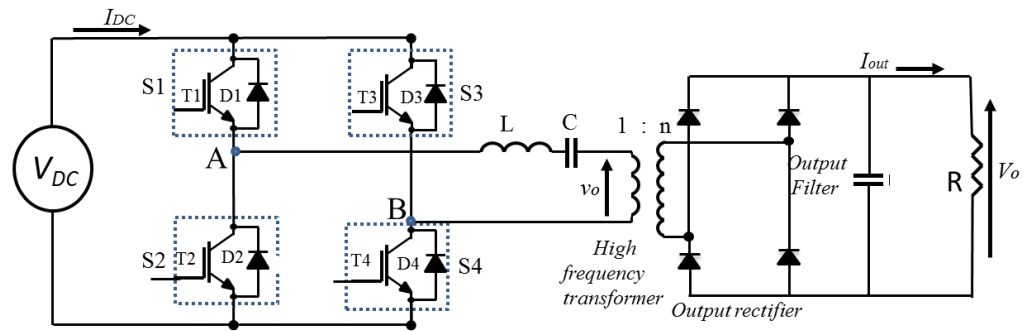
Figure 3.4 the SRSL DC-DC converter

The resonant frequency of the LC circuit and the circuit quality factor are given as in equations (3.1) and (3.2).

$$\omega_o = \frac{1}{\sqrt{LC}} \tag{3.1}$$

$$Q = \frac{\omega_o L}{R_{eq}} \tag{3.2}$$

Where, R_{eq} is the equivalent AC side resistance of the output stage (rectifier, filter and DC load), L and C are the tank parameters.

A square or quasi-square voltage across the resonant circuit is produced by switching the H-Bridge while the current in the tank is assumed to be sinusoidal when $Q>2.5$. The Fundamental Mode Approximation (FMA) can be applied to analyse the circuit as a result of the highly selective nature of the frequency

response of the resonant circuit. The voltage gain, $\dfrac{v_o}{V_{AB}}$, and the resonant tank

phase shift, φ, (angle between the applied voltage and current) can be derived

as:

$$\frac{v_o}{V_{AB}} = \frac{1}{\sqrt{1+Q^2\left[(F)-(F^{-1})\right]^2}}$$ (3.3)

$$\varphi = \arctan[Q.(F-F^{-1})]$$ (3.4)

Where F is the normalised operating frequency and given as:

$$F = \frac{\omega}{\omega_o}$$ (3.5)

Where, ω here is the switching frequency. Note that when F=1, the resonant tank
phase shift will be zero and the voltage gain is maximum. Figure (3.5) shows
the voltage gain and the resonant tank phase shift when Q=3 and, ω_o=20 kHz.
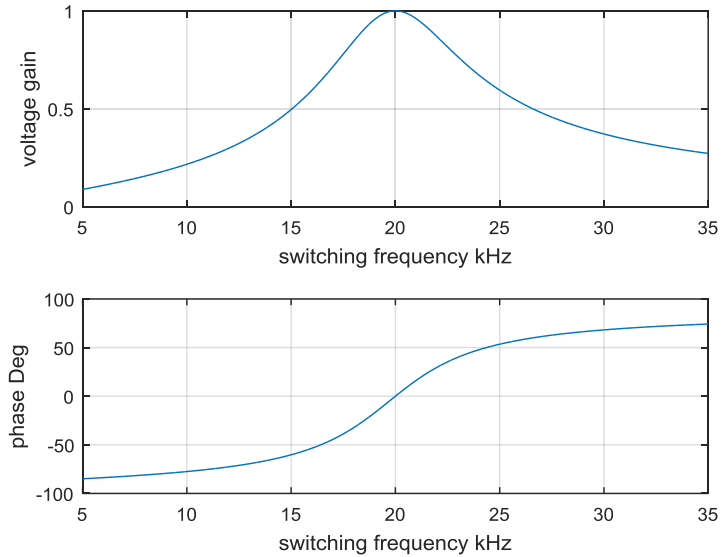
Figure (3.5) voltage gain and resonant tank phase shift at 20 kHz and Q=3

It is important to note that when operating below resonance, the circuit exhibits
the characteristics of a capacitive circuit, while when operating above resonance,
the circuit appears inductive. In an SRSL converter, the output voltage or the

tank current can be controlled by varying the operating frequency away from the resonant frequency in either direction.

It is preferable to operate the converter above the resonant frequency where all commutations are soft switching occurrences except one. This one is due to the IGBT turning OFF whilst carrying significant current [5]. In order to reduce the loss associated with this commutation, capacitive snubbers are utilised [7].

With regard to operation below the resonant frequency, a significant switching loss occurs due to the commutation from the diode to the active switch in the same converter leg (diode reverse recovery stress). Thus, in general this method of operation is avoided [5] .

One of the main advantages of the SRSL converters is their simplicity and their high efficiency at reduced loads due to the current in the power devices being proportional to the load current. This decreases power device conduction losses as the load decreases. In addition, the series connection between the resonant capacitor and the load eliminates the DC components in the load current, thus avoiding transformer saturation, which allows the use of a matching transformer for various required levels of a load voltage.

However, it is well known that significant parasitic inductance and capacitance exist in a practical high voltage, high frequency transformer. In SRSL converters the parasitic inductance can be included in the tank elements, but the parasitic capacitance cannot be included. "Well known transformer winding techniques can be used to minimize parasitic capacitance in step-up transformers. The basic technique is to wind the secondary layers in a manner that minimizes the voltage difference between adjacent layers" [46]. Authors in [47-50] use higher order tank configuration (LCLC and LCC) in order to allow the converter to use the transformer leakage inductance and inter-winding capacitance to be as a part of the tank elements. This has not been considered further in this work but could be the subject of future research.

Another disadvantage of the SRSL converters that , in short circuit operation a significant high and destructive current will flow through the circuit "since at resonance the only resistance in the circuit apart from the load is parasitic" [38].

For this reason, this operation mode must be avoided. Moreover, in case of no load operation, the output voltage cannot be regulated.

The SRSL converter is suitable for applications where a high voltage low current is required and where a no load application is not required. Radio frequency generators, (magnetrons, klystrons) and electrostatic precipitators can make use of these advantages [9, 10].

3.3.1.2 Series Resonant Parallel loaded (SRPL) converter

The circuit of the series resonant parallel loaded converter with a DC load represented by a resistance, *R*, is shown in Figure (3.6).
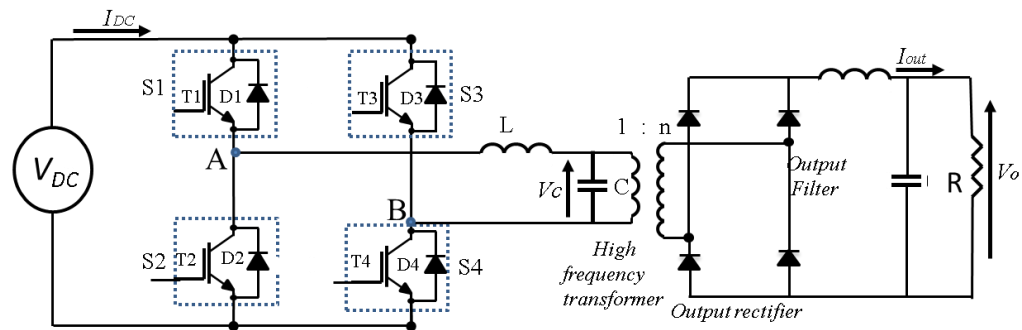
Figure 3.6 SRPL DC-DC converter

 In this configuration, the load is connected across the resonant capacitor, C, and the resonant "tank" is connected in parallel with the load. In addition, a high frequency transformer can be employed to provide a galvanic isolation between the load and the converter as required by the application and also to scale up or down the output voltage if required [51]. Unlike the SRSL converter, this topology is more complicated to analyse as the load is connected in parallel with the resonant capacitor. The voltage gain of the SRPL converter is given as:

$$\frac{V_c}{V_{AB}} = \frac{Q}{\sqrt{Q^2\left[1-(F)\right]^2 + \left[(F)\right]^2}}$$
(3.6)

From this equation, it can be observed that the output voltage is equal to Q times the input voltage at resonance (F=1). When the circuit is implemented to generate high voltage, the turns ratio required by the transformer can be reduced by this voltage gain. This is a significant advantage.

In contrast to the operation of the SRSL circuit, the operation of the SRPL circuit provides inherent short circuit protection. In addition, no load voltage regulation

can be achieved, however, care must be taken when operated under no load conditions at resonance as this leads to a high circulating tank current. This high circulating current affects the circuit's efficiency when operated with variable output load and fixed output voltage.

In order for the voltage magnitude to be controlled at a constant in a fixed output voltage, a constant magnitude of AC current must flow through the resonant capacitor at all output loads. This circulating current creates conduction losses even when no load is attached.

3.4 Resonant RF modulators

Resonant radio frequency modulators have the same general block diagram shown in figure (3.3). As previously mentioned, the input is AC at the line frequency (50 or 60Hz). Direct or indirect resonant converters are used to convert this input into high frequency (20-30 kHz) voltage for driving the resonant tank circuit. Thus, using the highest possible frequency has several benefits such as achieving a very high bandwidth control and a large reduction in the transformer size and other filtering components. Moreover, at the considered power levels (100kW) and frequency range (20-30 kHz), off the shelf components can be utilised.

Over the past 15 years, the University of Nottingham has worked on resonant power converters for a number of industrial applications such as Long Pulse Generators, Continuous Wave and Pulsed Magnetron and Klystron modulators. The following sub-sections present various configurations of resonant power converters for RF tube modulators. The research in this area aimed to develop a new power supply technology for driving RF tubes as well as other industrial applications such as Electrostatic Precipitators.

3.4.1 Direct Resonant Converter (DRC)

Direct resonant converters have the ability to provide a controllable AC waveform from another AC source without an intermediate change to DC form, which could contribute to reducing the converter component count, cost, and size as a bulky DC link is not required [52, 53].

A continuous wave modulator based on a direct resonant converter for high power RF application has been developed by the PEMC group at the University of Nottingham [39]. The modulator is composed of an input filter, a three phase to single phase array of power switches and a resonant tank. This concept entails the use of six common emitter derived bidirectional switches to convert the three phase voltage source at 50/60Hz into a single phase voltage source at 20 kHz. A SRPL approach was selected in order to incorporate the transformer leakage inductance and parasitic capacitance into the tank network. As the SRPL topology is operated optimally at full power this topology can be used as a fixed load CW modulator. Figure 3.7 shows the direct resonant converter for RF applications:
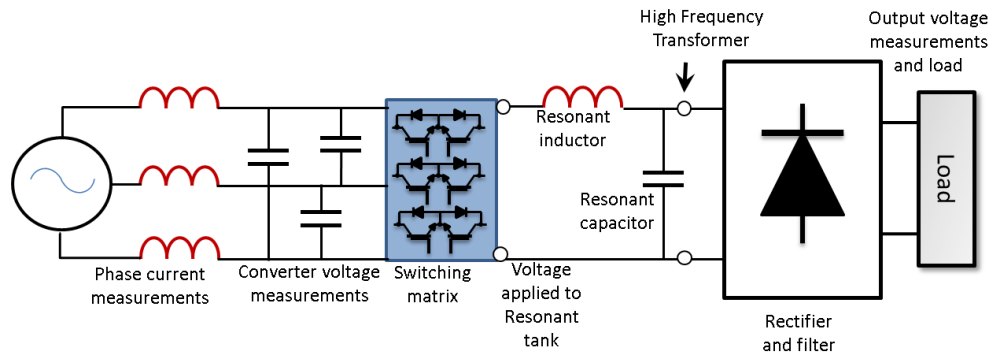
Figure 3.7 direct SRPL resonant converter

In this topology, the transformer and the resonant tank elements need to be designed not only for load current but also the resonant circulating current. Hence, the transformer volt ampere VA rating is higher than the actual output VA of the resonant converter.

Another approach of DRC for high voltage DC power supply applications has been developed [42]. This topology is based on SRSL tank configuration in order to avoid the aforementioned drawback and also to consider variable load operation. Figure 3.8 shows the diagram of the direct resonant converter DRC.
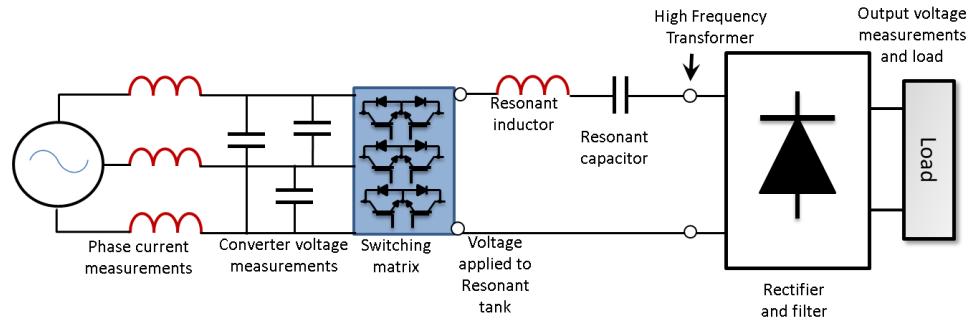
Figure 3.8 direct SRSL resonant converter DRC.

One of the main advantages of direct resonant converter topologies is that the converter is able to offer unity power factor operation on the supply side when employing a proper control strategy. It is applicable to achieve high efficiency by switching the semiconductor devices at every zero crossing of the output current (ZCS). Moreover, it has a high power density and a smaller size compared to the conventional converters due to the high frequency operation and the absence of the input DC link.

However, the direct resonant converters can be easily affected by any poor input power which will be reflected in the quality of the output power [54] for example in applications such as CW magnetrons and klystron very pure energy is required. The latter drawback could prevent it from serving in some applications such as those where the main power supply is limited (an example is an offshore oil field, treatment of oil-contaminated drill cuttings where the power source may be a number of diesel generators) and could be affected by other devices on the same electrical network.

3.4.2 Indirect Resonant Converters (IDRC)

Unlike the direct resonant converter, the IDRC has an intermediate DC stage which could prevent the poor input power from propagating into the output load. Pulse modulators based on the indirect resonant converter for high power RF applications have been developed by the PEMC group at the University of Nottingham [55] [56]. The modulator comprises of a three phase rectifier which is used to charge a DC link capacitor bank. An H-Bridge inverter is employed to produce variable frequency and duty cycle quasi-square wave voltage. Also, a resonant tank and step up transformer are utilised to obtain the voltage levels

required. In the last stage, a rectifier and filter components are adopted to attain low ripple output. For the approach shown in figure 3.9, a three phase SRPL converter is used.
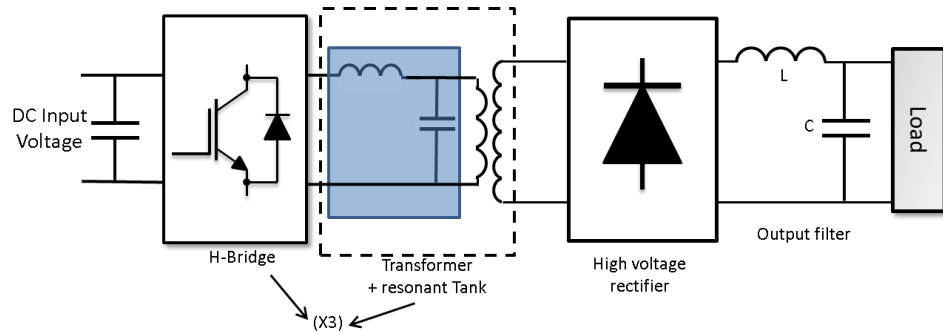
Figure 3.9 Three phase SRPL resonant converter

For SRPL topology, optimal switching waveforms can be achieved only at full load and a specific designed operating point. This is why it is suitable for pulses not for CW with variable loads. The SRSL topology is chosen for CW with variable loads.

3.4.3 **Proposed Converter and Application**

Supplying a CW magnetron for CW heating applications such as those discussed in chapter 2 is the focus of this work. The load characteristics of the industrial magnetron (shown in chapter 2) requires high voltage and low current power supply. Based on the discussion in the previous sections, the IDRC based on SRSL converter has been found suitable for such applications. This is due to its ability to control the output current (anode current) and its ability to produce a more desired relationship between the load and the tank current when compared to the SRPL circuit. The SRSL power converters do not suffer from resonant tank circulating current and do not contain an output inductive filter [57].

Moreover, the IDRC has an intermediate DC stage (DC link) which helps prevent poor input power quality from propagating into the load. Offshore applications (where the main power supply is limited and could be affected by plugging any additional device and small space required) such as treatment of oil-contaminated drill cuttings, can make the use of these advantages.

Previous work [55] [56] has considered the SRPL converter and demonstrated that a phase/frequency modulation method can be used to obtain soft switching at a fixed load (fixed quality factor) by utilising a 4th order approximation to this phase/frequency characteristics. This relationship may become inaccurate as the load is changed as it assumes a fixed quality factor. This may lead to a decrease in efficiency. Due to this, this work has been carried out to consider the use of a look up table approach over wide ranges of quality factor. In this thesis and for the first time the SRSL converter is considered to be used as a modulator to drive the CW magnetron with variable load requirements, using phase/frequency modulation.

3.5 Conclusion

This chapter has provided an overview and development of RF modulators technology. The advantages and disadvantages of each topology are discussed. The load resonant converters have been presented in more detail. The previous research carried out at the University of Nottingham in this area was briefly introduced. The research over the last fifteen years in this area aimed to develop a new power supply technology for driving RF tubes. The SRSL DC-DC converter is decided to be suitable topology for supplying CW industrial magnetrons for CW heating applications. The following chapter will discuss the SRSL converter as the proposed topology in more detail.

Chapter 4

THE PROPOSED APPROACH FOR A CW MAGNETRON

4.1 Introduction

As discussed in chapter 2, the anode current and voltage characteristics of the magnetron show that the magnetron has exceptionally low dynamic impedance. A small variation in the applied voltage can cause appreciable change in the operating current. Therefore, the magnetron power supply must have regulated current characteristics for stable operation [20]. In addition, based on the discussion in section (3.4.3), a high voltage DC power supply based on a series resonant series loaded SRSL converter is proposed to be used as a power supply for CW magnetrons. The SRSL inverter behaves like a current source since the resonant tank and load are connected in series. A high frequency step up transformer linked between the inverter and the output rectifier is employed for the high load voltage and low current requirement.

One of the main advantages of using this topology is that the SRSL converter is highly efficient at light loads because the resonant tank current decreases with an increase in the load resistance. Another advantage is that the series resonant capacitor blocks any DC component in the inverter voltage, and consequently it prevents the high voltage HV transformer from saturating. Moreover, in contrast to the SRPL, the SRSL current decreases by decreasing the load current. This reduces the conduction losses and improves efficiency. In addition, a simple capacitive filter on the output side is sufficient; thus there is no need for a costly and bulky output inductive filter. For these reasons, the SRSL DC-DC resonant power converter is suitable for the high voltage CW applications. In this chapter the circuit description and the principle of operation under steady state conditions for the resonant SRSL DC-DC converter is covered. This enables a design for the main converter component to be made and to address the challenges in the application of the approach.

4.2 SRSL DC-DC Converter

It has been decided that the series resonant series loaded DC-DC converter topology is to be employed as a modulator for industrial magnetrons in heating applications. The following sub-sections analyse and consider the topology structure in order to enable the design and control of the converter.

4.2.1 Circuit Description

Figure 4.1 shows a schematic diagram of the proposed SRSL DC-DC power converter.
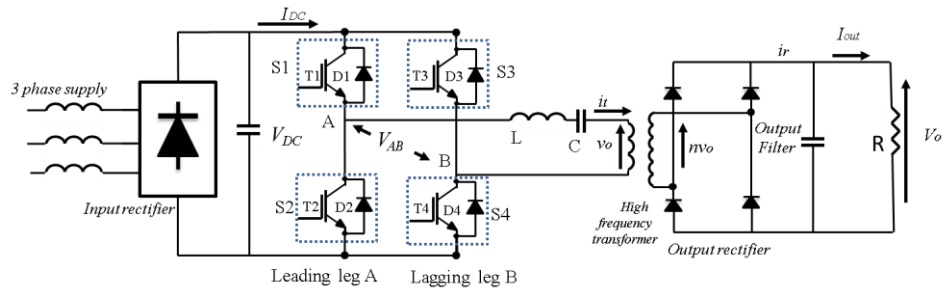
Figure 4.1 the proposed series resonant series loaded converter schematic

The DC source is derived from a three phase diode rectifier and the single phase full bridge inverter excites the series resonant tank with a high frequency quasi square wave voltage. In order to step up the voltage to the required level, a high frequency high voltage transformer is utilised. The final stage contains a diode bridge rectifier, a capacitive filter and the load which appears in series with the resonant tank. The load modelling is an equivalent circuit of the magnetron I-V characteristic. For simplicity, in the following design and steady state analysis, the load is modelled as a resistive load, R.

4.2.2 Steady State Analysis

In order to analyse this converter, the following parameters must be considered:

- Resonant frequency (f_o or ω_o). This can be defined as the frequency where the input voltage and current become in phase or the frequency which cancels out the inductive and capacitive impedance leaving just a peak voltage across the AC load resistance (R_{eq}). It is given as in (4.1).

$$\omega_o = 2\pi f_o = \frac{1}{\sqrt{LC}} \qquad (4.1)$$

- Characteristic impedance (Z_o). This can be defined as the absolute value of the inductive impedance or of the capacitive impedance calculated at the resonant frequency. It is given as in (4.2).

$$Z_o = \sqrt{\frac{L}{C}} \qquad (4.2)$$

- Normalised frequency or the frequency ratio *(F)*. This can be defined as the ratio of the operating frequency *((ω)* in rad/sec or *(f)* in hertz) compared with the resonant frequency *((ω_o)* in rad/sec or *(f_o)* in hertz). It is defined by (4.3).

$$F = \frac{\omega}{\omega_o} = \frac{f}{f_o} \qquad (4.3)$$

- Loaded quality factor (Q). This is defined as the ratio of stored energy in the resonant tank reactive component (capacitor (C) or inductor (L)) compared with the energy dissipated in the load (R_{eq}) in each cycle. Thus it is defined by (4.4)

$$Q = 2\pi \frac{Total\ energy\ stored\ at\ resonant\ frequency\ (W_s)}{Energy\ dissipated\ per\ cycle\ at\ resonant\ frequency\ (T_o.P_R)}$$

$$(4.4)$$

Where the resonant frequency $f_o = \dfrac{1}{T_o}$ and P_R is the dissipated power.

The following quantities can also be derived:

- The total energy stored in the resonant tank

$$W_s = W_{L\max} = \frac{1}{2} L.\mathrm{I}_m^2 \qquad (4.5)$$

Where, $W_{L\max}$ is the maximum energy stored in the inductor and I_m is the amplitude of the tank current. Then the loaded quality factor can be defined as

$$Q = \frac{\omega_o.W_s}{P_R} = \frac{\omega_o L}{R_{eq}} \qquad (4.6)$$

The tank parameters (*L and C*), are given according to the following equations.

- The resonant tank inductor

$$L = \frac{Q.R_{eq}}{\omega_o} \qquad (4.7)$$

- The resonant tank capacitor

$$C = \frac{1}{\omega_o.R_{eq}.Q} \qquad (4.8)$$

In load resonant DC-DC converters, the H-Bridge inverter supplies the resonant tank with a quasi-square wave voltage [3, 10]. The fundamental component of the tank input voltage can be obtained by means of Fourier series of the quasi-square wave signal shown in figure 4.2.
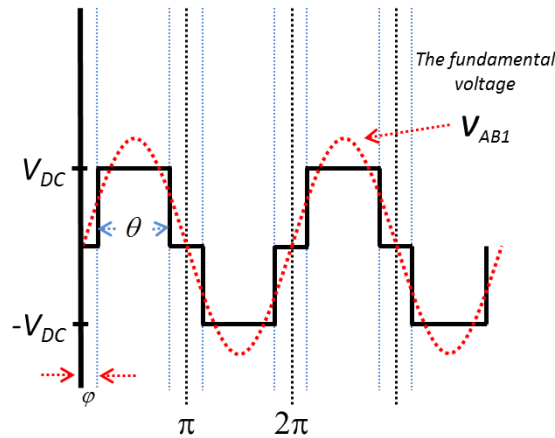
Figure 4.2 quasi-square wave signal

This series is given by:

$$V(t) = \sum_{n=1}^{\infty} \{ \frac{2V_{DC}}{n\pi}[1-\cos(n\pi)]\cos(n\varphi)\}\sin(n\omega t) \qquad (4.9)$$

When the phase angle $\varphi = 0$ the peak value of the fundamental component of the full square wave signal is obtained as:

$$\hat{V}_1 = V_{AB1} = \frac{4V_{DC}}{\pi} \tag{4.10}$$

From an analytical point of view, the final stage in the load resonant DC-DC converter (rectifier , filter and load) can be used as an AC load of the inverter [5]. Therefore, in a separate stage, the inverter can be analysed and designed independently of the rectifier.

The following analysis is carried out in order to simplify the SRSL converter in figure 4.1 for design and control purposes. Assuming a sinusoidal tank current (i_t), the output stage is in series with the resonant tank which acts as a current source. The primary transformer voltage (v_o) or the rectifier input voltage (nv_o) is a square wave voltage, whose peak magnitude depends on the DC output voltage (V_o). Figure 4.3 shows the waveforms of the primary transformer voltage (v_o) and the rectified output current (i_r) which is corresponding to the tank current (i_t).
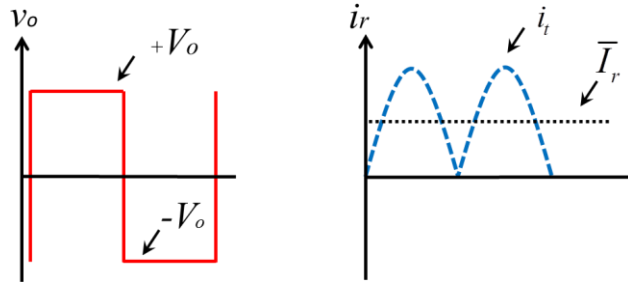
Figure 4.3 the primary transformer voltage and the rectified output current

The average rectified current is given by (4.11) and the primary transformer voltage is given by (4.12) considering only the fundamental component.

$$\bar{I}_r = I_{out} = \frac{2i_t}{n\pi} \tag{4.11}$$

$$v_{o1} = \frac{4V_o}{n\pi} \tag{4.12}$$

The rectifier stage and the load R can be replaced by equivalent AC load resistance, R_{eq}. Thus the equivalent AC load is written as (4.13).

$$R_{eq} = \frac{8R}{\pi^2 n^2} \tag{4.13}$$

From the previous discussion and by making the fundamental mode approximation, the equivalent circuit for the SRSL converter becomes as shown in figure 4.4.
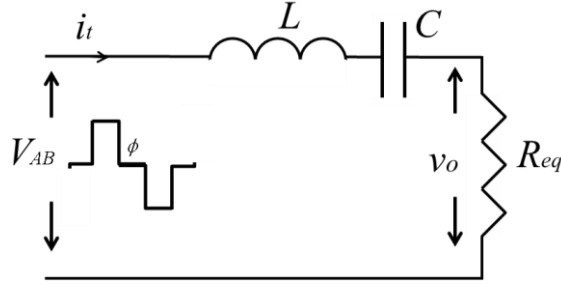
Figure 4.4 equivalent circuit of Full-Bridge SRSL converter

The following analysis of the SRSL converter of figure 4.1 is based on the equivalent circuit of figure 4.4 and the following assumptions.

- The transistor and diode ON state resistances are neglected
- The parasitic capacitance of the transistors is also neglected
- The switching time of the semiconductor devices is zero.
- The elements of the series-resonant circuit and the high voltage transformer are time invariant and do not have parasitic resistive components.
- The loaded quality factor Q of the series resonant circuit is high enough so that the tank current is sinusoidal.

From figure 4.4, the input impedance of the series resonant circuit can be derived as:

$$\mathbf{Z} = R_{eq} + j(X_L - X_c) = R_{eq} + j(\omega L - \frac{1}{\omega C}) \tag{4.14}$$

By utilising the definition of ω_o , F and Q from equations (4.1), (4.3) and (4.6), equation (4.15) can be rewritten as:

$$\mathbf{Z} = R_{eq}.[1 + j.Q.(F - F^{-1})] = Z.e^{j\varphi} = R_{eq} + jX \tag{4.15}$$

Where, the magnitude of the impedance Z and its angle φ are given by

$$Z = R_{eq}\sqrt{1 + Q^2(F - F^{-1})^2} = Z_o\sqrt{\frac{1}{Q^2} + (F - F^{-1})^2} \tag{4.16}$$

$$\varphi = \arctan[Q.(F - F^{-1})] \tag{4.17}$$

$$R_{eq} = Z\cos\varphi \tag{4.18}$$

$$X = Z\sin\varphi \tag{4.19}$$

$$\cos\varphi = \frac{1}{\sqrt{1 + Q^2(F - F^{-1})^2}} \tag{4.20}$$

From equation (4.15) it can be observed that when the converter is operated at the resonant frequency ($F = 1$), the reactance of the resonant tank becomes zero.

Figure 4.5 shows the angle of the total impedance as a function of the frequency ratio and the quality factor Q.
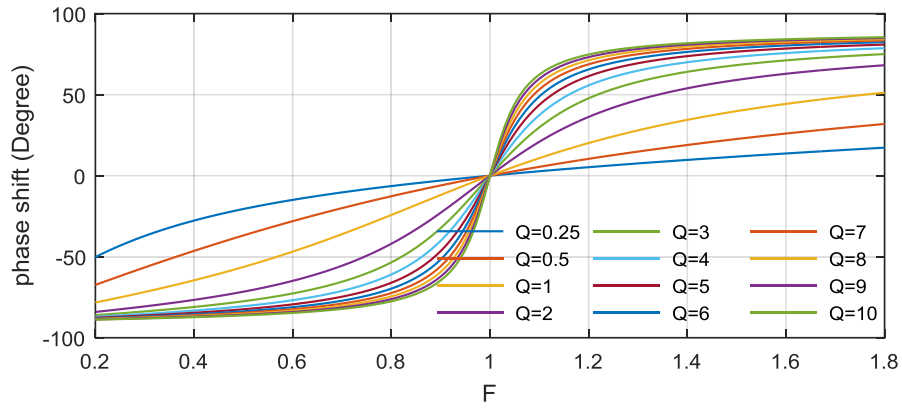
Figure 4.5 angle of the total impedance of a series resonant circuit

It can be seen that the quality factor and the switching frequency have an effect on the resonant circuit. For $f > f_o$, the resonant circuit appears as inductive load where φ is greater than zero, however, for $f < f_o$, the circuit appears as capacitive load where φ is smaller than zero.

Figure 4.6 (a) and (b) show the SRSL circuit and its input impedance (Z) as a function of the operating frequency at different loaded quality factor values. The impedance of the circuit is a minimum at the resonant frequency and increases when the operating frequency moves away from f_o. This means that when varying the operating frequency away from f_o, the input current reduces and therefore the load voltage decreases due to series connection.
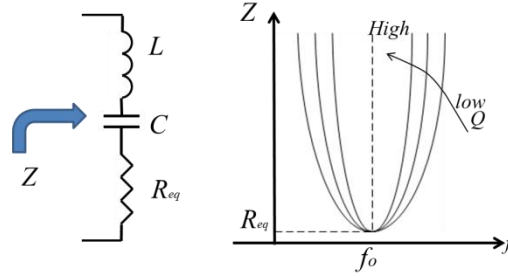
Figure 4.6 SRSL circuit and its input Z as a function in f at different Q

With regard to the range of Q in the load resonant converter design, choosing a Q which is too high will result in high energy storage and consequently a large size of the tank component. However, if Q is too small, the tank current will be distorted and the fundamental component approximation used in the analysis will be in error. Therefore, it is crucial to compromise on this factor.

Based on the equivalent circuit of the SRSL converter in figure 4.4, the voltage transfer function of the resonant tank $H(F)$ can be derived as given in (4.21)

$$H(F) = \frac{v_o}{V_{AB}} = \frac{i_t . R_{eq}}{i_t . Z} = \frac{1}{\sqrt{1 + Q^2 (F - F^{-1})^2}} \qquad (4.21)$$

Figure 4.7 illustrates the input/output voltage relationship, $H(F)$ as a function of the frequency ratio at different values of Q.
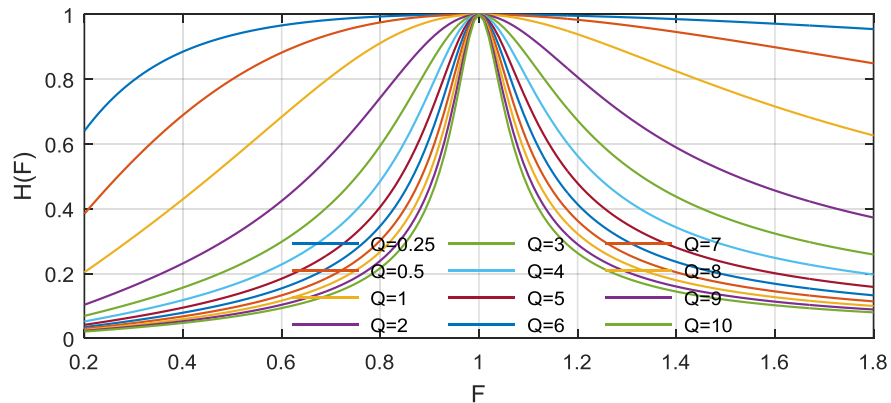
Figure 4.7 voltage conversion ratio curve of SRSL converter

It is interesting to note that as the load is decreased, the DC characteristic becomes very flat; then the curve has less selectivity [58]. However, by using the combined phase and frequency modulation, the output voltage can be regulated at lower loads than using the frequency modulation alone. This will be discussed in details in chapter 5.

4.2.3 Principle of Operation

Figure 4.8 shows the principle of operation of the series resonant series loaded power converter. The resonant current is sinusoidal when the loaded quality factor is assumed to be high ($Q \geq 2.5$). All H-Bridge main switches maintain soft switching only when the operating frequency is equal to the resonant frequency ($f = f_o$) as shown in figure 4.8b. In this case the IGBTs turn on and off at zero current, resulting in zero switching loss and high efficiency. Practically, in many applications the output voltage is controlled by varying the operating frequency below or above the resonant frequency ($f < f_o$ or $f > f_o$) [5].
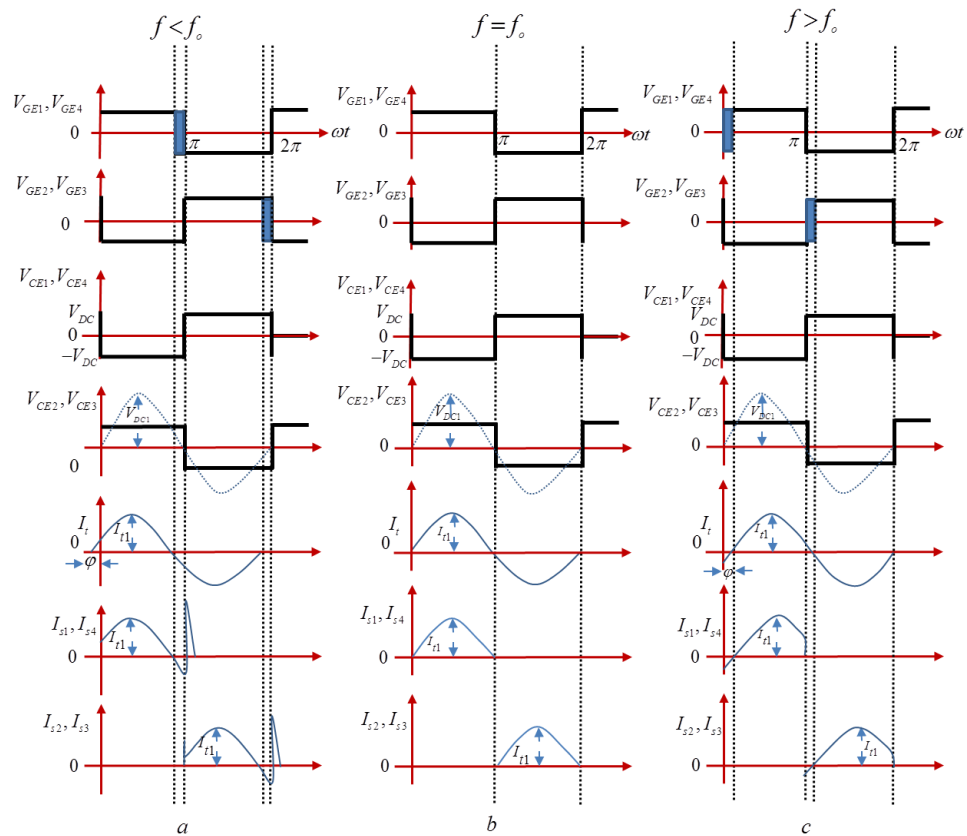
Figure 4.8 SRSL converter operation (a) for $f < f_o$ (b) for $f = f_o$ (c) for

$$f > f_o$$

4.2.3.1 Operating Below the Resonant Frequency

Figure (4.8a) shows the waveforms of the H-Bridge when $f < f_o$. The current through the resonant circuit leads the fundamental component of the tank input V_{AB} by phase angle φ, this results in a dominating capacitive load at this frequency. From the waveforms in figure (4.8a), it is clear that the switch current through switches S_1, S_4 is positive after the T_1, T_4 turn ON and negative before T_1, T_4 turn OFF. The conduction sequence of the switches is $T_1, T_4 - D_1, D_4 - T_2, T_3 - D_2, D_3$. This sequence causes the current of the resonant circuit to commutate from the diode of one switch to the transistor of the other switch, which leads to diode reverse recovery stress when the diode is turned OFF. This generates high reverse recovery spikes due to the very large di/dt during the diode turn OFF. These spikes flow through the other transistor because the resonant inductor does not allow abrupt current changes. Consequently, these spikes rapidly increase the switching loss and may damage the transistors. One of the main advantage of operating below the resonant frequency is that the turn OFF switching loss is almost zero because all transistors are switched OFF at nearly zero voltage (ZVS). However, there is a turn OFF switching loss in the diodes (reverse recovery) and turn ON switching loss in the transistors.

4.2.3.2 Operating Above the Resonant Frequency

Figure 4.8c shows the waveforms of the H-Bridge when $f > f_o$. The current through the resonant circuit lags the fundamental component of the tank input voltage V_{AB} by phase angle φ; this results in a dominant inductive load at this frequency. From these waveforms in figure 4.8c, it can be seen that the current through switch S_1, S_4 is negative after the T_1, T_4 turn ON and positive before T_1, T_4 turn OFF. The conduction sequence of the switches is $D_1, D_4 - T_1, T_4 - D_2, D_3 - T_2, T_3$. As the transistor T_1, T_4 is switched OFF, the V_{CE1}, V_{CE4} increases and V_{CE2}, V_{CE3} decreases. Consequently, the diode D_2, D_3 turns ON and the current commutates from T_1, T_4 to D_2, D_3. Thus the turn OFF transition is caused by the gate drive voltage V_{GE1}, V_{GE4} while the turn ON

transition is forced by the turn OFF transition of the other transistors. Therefore, all transistors are turned ON at zero voltage and there is no turn OFF switching loss in the diodes due to the absence of reverse recovery. It can be summarised that soft switching occurs during the turn ON transitions; however there is a switching loss during the turn off transition. The turn OFF switching loss can be reduced by adding a suitably dimensioned snubber capacitor to the leading leg of the H-Bridge and having sufficient dead time during transitions as will be explained further in chapter 5.

4.3 Design Results

Modern industrial heating magnetrons are powerful (hundreds of kW) and efficient sources of continuous wave (CW) microwaves. They operate at frequencies just below the bottom boundary of the L-band. General characteristics of some CW industrial heating magnetrons which deliver more than 100kW of output microwave power are available as off-the-shelf products [59]. In this work, the power converter design has been developed to be capable of supplying a 100kW L-band industrial heating magnetron (a typical e2v Technologies BM100L Series Continuous Wave CW Magnetron) [60].

Before designing the resonant converter, some parameters have to be identified. These parameters are the load voltage (V_o), the rated load current (I_{out}), the load resistance (R) the output power, the load voltage ripple (V_r), the operating frequency (f), the resonant frequency (f_o), the load quality factor (Q), the DC link voltage (V_{DC}), the transformer turns ratio (n), the tank inductor (L), the tank capacitor (C) and the capacitive filter.

From the data sheet of the considered (100kW, BM100L-Band CW Magnetron), the anode voltage (load voltage) is 19.5-20kV, the anode current (load current) is 5.8-6A, consequently the nominal load resistance is chosen as 3.33kΩ, and the CW Power Output is 100kW. In this work the load voltage ripple is chosen to be less than 5%. The switching frequency of the converter is also the trade-off between the switching losses in the power semiconductors and the passive component size. High switching losses are the result of high operating frequencies. However, high operating frequencies also reduce the passive component size. A switching frequency range of 20-24 kHz is used for the IGBT

operation and a suitable Q of 2-5 was chosen in this design in order for the resonant tank current to be considered sinusoidal.

The DC link voltage was determined to be 560V obtained from standard AC mains by using a three phase bridge rectifier. The turn's ratio (n) of the transformer can be obtained based on the fundamental component of the voltage on the primary side of the transformer (v_o) and desired output voltage (Vo) from equation (4.12). Equations (4.7) and (4.8) are used to calculate the tank parameters values (L, C). The procedures of calculating the filter capacitance is shown in appendix A.

The power supply specifications and design values of the major components of the proposed converter are summarised in table 4.1. These component values are used in all of the following simulations.

Table 4.1 the power supply specifications and design results of the proposed converter

	DESCRIPTION	SYMBOL	VALUE
POWER SUPPLY SPECIFICATIONS	Load voltage	V	19.5-20kV
	Load voltage ripple	V_r	<5%
	Load current	I	6A
	Output power	P	100kW
	Quality factor	Q	2- 5
	Switching frequency	f_{sw}	20-24 kHz
	DC-Link voltage	V_{DC}	561V
DESIGN RESULTS	Tank inductor	L	33.41 µH
	Tank capacitor	C	1.894µF
	Resonant Frequency	f_o	20kHz
	output filter capacitance	C_f	0.166µF
	Transformer turns ratio	N	1:44

Figure 4.9 shows an I-V (Current-Voltage) characteristic for an industrial magnetron, where the range of Q from 2 to 5 is inside the light blue area.
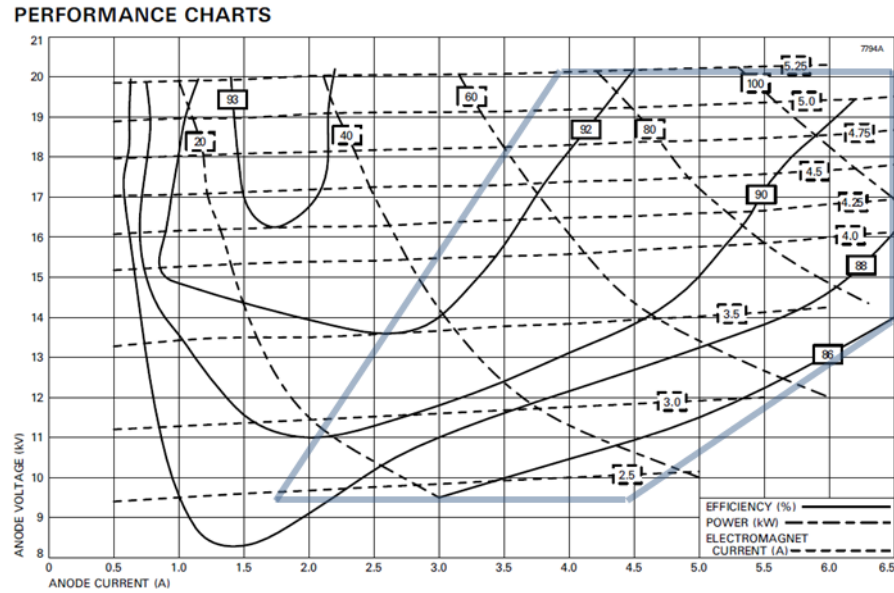
Figure 4.9 Magnetron I-V characteristic [24]

It can be observed that along the selected Q (from 2 to 5), the load can be changed in a wide range for example from around 110kW at an efficiency of 90% to 40kW at an efficiency of 92% or 20kW at an efficiency of 86%. In addition, it can be seen that the Q range (2-5) is within the limits of the specifications given by the magnetron manufacturer.

In order to practically validate the proposed control scheme, a reduced scale prototype power converter design has been developed. This avoids the issues related with the production of high voltage whilst still enabling validation of the proposed methodologies. The 3kW prototype is implemented to validate the novel proposed variable load SRSL converter. This prototype design is detailed in chapter 7.

4.3.1 Simulation Model

In order to verify the proposed converter topology, PLECS has been used to develop the simulation models. With PLECS, the simulation time is very fast. PLECS also provides powerful graphic tools using the probe and scope. The controller used in the simulation can be run in both the continuous mode (s-domain) and the discrete mode (z-domain) due to the fast simulation time. All simulation results presented in this thesis were determined using the PLECS simulation model.

4.4 Challenges in the Application of the Approach

It is desirable to raise the switching frequency in order to minimise the size of the passive components. However, at the power levels required, these operating frequencies can only be considered if the semiconductor switching losses are significantly reduced. Therefore as already determined a resonant power supply topology is proposed. This achieves low switching losses by using soft-switching techniques where either the voltage across or current through the semiconductor device is zero at the instant of switching.

Some modulation techniques, which will be discussed in chapter 5,   can be employed to appropriately operate the resonant converter. For example a combined frequency and phase modulation (CFPM) can be directly applied to modulate the resonant converter with a fixed load [7, 51, 61, 62]. However, operating with variable load is required in some industrial applications such as driving magnetrons in industrial heating applications. In this case the equivalent load resistance "seen" by resonant converter is variable. Therefore, the quality factor Q is not fixed and the CFPM modulation cannot ensure soft switching operation [6]. Using the CFPM modulation to modulate the resonant converter with variable load conditions could increase the switching losses to an unacceptable level.

In order to overcome the aforementioned limitations, a soft-switching tracking technique for high power resonant converters with variable or fixed load conditions is required. A novel variable Q based CFPM modulation technique is proposed in this thesis. For this technique, the soft-switching points for the whole operating range are pre-calculated and represented in a 3D lookup table. Hence, by feeding the actual load condition and control actuating signal, the accurate soft-switching point for the semiconductors can always be found during converter operation. The variable Q based CFPM modulation technique is a solution for the resonant converter dealing with variable load conditions. Considering the applications that the load resistance is measurable or can be evaluated through the load voltage/current characteristics (e.g. magnetrons), the accurate Q can be derived accordingly. Combining Q with the modulation index produced by an appropriate feedback current control loop and DC-link

measurement, the demanded frequency ratio F (and the required switching frequency) can be derived, and the corresponding phase shift that retains soft-switching can also be derived. As a result, the influence of the variable load on the soft switching scheme can be overcome. This novel technique is presented in detail in chapter 5.

4.5 Conclusion

In this chapter, the SRSL converter based modulator for driving an industrial magnetron with variable load conditions has been proposed. The introduction of an AC analysis technique has greatly simplified the steady state analysis of this system. This technique assumes the use of sinusoidal voltage and current in the system. It is shown by the plot of the normalised gain against normalised frequency that at the resonance, the normalised system gain is unity. This normalised system gain decreases upon deviation from this frequency.

The converter steady state analysis was presented to design the main converter components. Challenges in the application of the proposed converter are discussed and it is highlighted that an extended CFPM modulation technique (Variable Q based CFPM) is required to enable the SRSL converter to maintain soft switching whilst driving a variable load. Modulation techniques for the proposed converter will be discussed in the next chapter.

Chapter 5

MODULATION

5.1 Introduction

In this chapter, modulation of the Series Resonant Series Loaded (SRSL) converter will be considered. Figure 5.1 shows the open-loop control structure of the SRSL converter. The converter is controlled via the H-Bridge inverter. The H-Bridge is basically driven by applying gate signals (GS1- GS4) to the four switching devices (IGBTs, S1-S4).
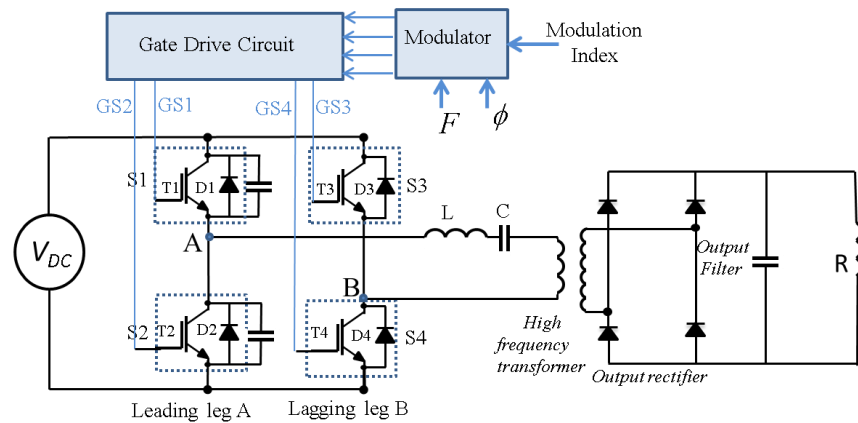
Figure 5.1 simplified circuit of the proposed converter

The output stage (transformer, rectifier, filter and DC resistance) can be further treated as an AC resistance as analysed in Chapter 4. Due to the selective resonant tank, the H-bridge output can be represented by the fundamental component of the square wave voltage. Therefore, the equivalent circuit used for modulation analysis is as shown in Figure 5.2.
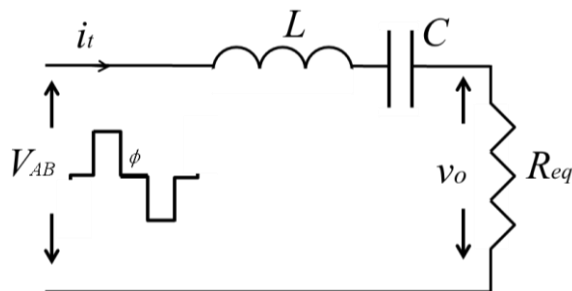
Figure 5.2 equivalent circuit used for modulation analysis

The modulation method is discussed considering existing different approaches and a novel modulation method for variable load operation is proposed and developed. In order to validate the feasibility of the adopted modulation method a single-phase resonant converter model has been developed in PLECS. Detailed simulation results will be presented.

5.2 Modulation Methods of SRSL Converter

Regulation of the output current (or voltage) for the SRSL resonant converter can be achieved by using one of three different methods; frequency modulation FM phase shift modulation PM or a combination of both FM and PM.

5.2.1 Frequency Modulation FM

This method relies on varying the impedance of the resonant tank. This can be achieved by varying the switching frequency above or below the resonant frequency. The resonant tank and the load act as a voltage divider and the gain is always less than 1 (maximum gain happens at the resonant frequency). As shown in figure 5.2, the load is connected in series with the resonant tank in case of SRSL resonant converter; therefore, regulating the output current is directly associated with regulating the output voltage, therefore, the voltage transfer function of the resonant tank is given by equation (5.1) as derived in chapter 4.

$$H(F) = \frac{v_o}{V_{AB}} = \frac{1}{\sqrt{1+Q^2(F-F^{-1})^2}} = \cos\varphi \qquad (5.1)$$

The modulation index M_I^F is defined in a way that it equals 1 when the resonant tank is fed by the maximum input voltage. From equation 5.1 it can be seen that when $F=1$, the voltage transfer function is maximum at 1. Thus the M_I^F, for a frequency controlled converter is given as in equation (5.2) and plotted in figure (5.3).

$$M_I^F = \frac{H(F)}{1} = \frac{1}{\sqrt{1+Q^2(F-F^{-1})^2}} \qquad (5.2)$$
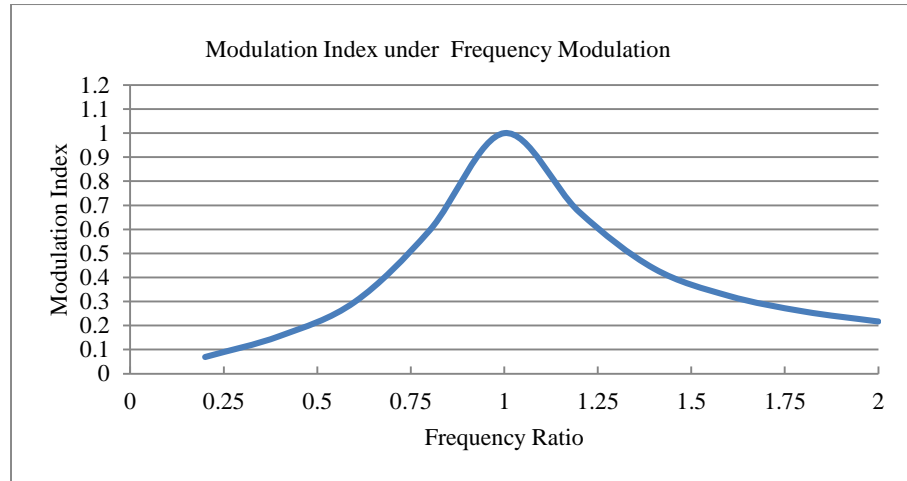
Figure 5.3 the modulation index under frequency control

In the frequency modulation method, the frequency ratio F is obtained for each given value of modulation index M_I^F by solving the equation (5.2) and assuming the quality factor Q is reasonably selective (i.e. $Q \geq 2.5$). The main drawbacks of *FM* are that the soft switching is only obtained for all switches at resonance and the range of frequency required is considerable for a wide control range. To control the output current, the switching frequency has to deviate from the resonant frequency, which results in the H-Bridge seeing a poor power factor with increased switching and conduction losses [63]. Figure 5.4 shows the typical waveforms of the tank voltage and current when the converter operates at the resonant frequency and figure 5.5 when the converter operates away from the resonant frequency. From figure 5.4, it can be observed that soft switching is obtained at resonant frequency.
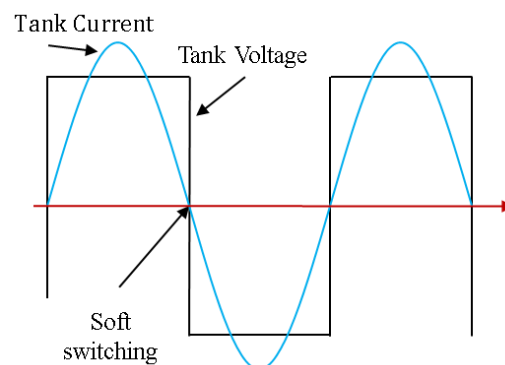
Figure 5.4 Typical waveforms of FM at resonant frequency

However, from figure 5.5 it can be seen that the soft switching is lost by operating the H-Bridge away from the resonant frequency lossless snubbers (capacitors) added across the switching devices may reduce only turn OFF loss but they cannot eliminate it [7].
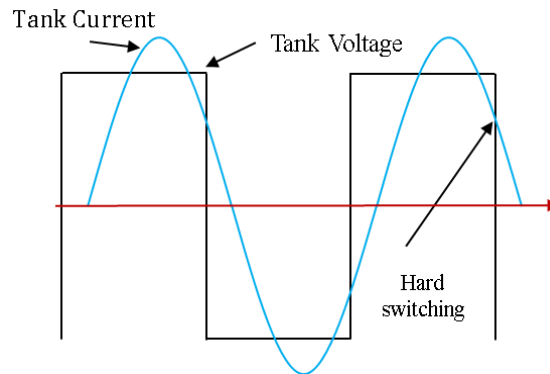
Figure 5.5 Typical waveforms of FM away from resonant frequency

5.2.2 Phase Shift Modulation PM

Phase shift modulation is used to regulate the magnitude of the H-Bridge fundamental output voltage V_{AB}. This is achieved by controlling the phase shift ϕ between the two legs of the H-Bridge with constant frequency [63, 64]. The theoretical waveforms for the resonant tank with *PM* are shown in figure 5.6.
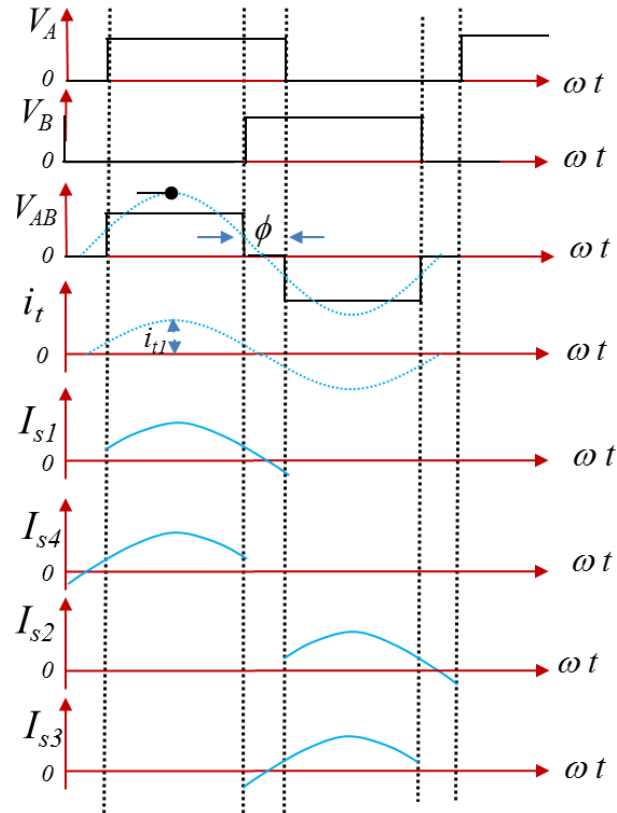
Figure 5.6 the theoretical waveforms for the resonant tank with PM

From figure 5.6 it can be noticed that the phase shift modulation method maintains unity displacement power factor at resonant frequency operation. Moreover, this approach yields soft switching of all IGBTs when $\phi = 0$. However, in order to regulate V_{AB}, the phase shift, ϕ between the two halves of the H-bridge must be varied. In this case the switches in leg A undergo a hard turn ON, whilst the switches in leg B undergo a hard turn OFF [7, 65]. The fundamental component of the tank input voltage V_{AB1} is obtained by using Fourier analysis.

$$V_{AB1} = \frac{4.V_{DC}}{\pi} . \cos \frac{\phi}{2} \qquad (5.3)$$

When the operating frequency is equal to the resonant frequency, the tank impedance is equal to zero and the output ac voltage v_o can be written as (5.4)

$$v_o = V_{AB1} \qquad (5.4)$$

From this equation it can be noticed that the maximum value of v_o is when $\phi = 0$ therefore the modulation index for phase control M_I^ϕ can be written as

$$M_I^\phi = \frac{V_{AB1}}{4 . \dfrac{V_{DC}}{\pi}} = \cos\frac{\phi}{2} \tag{5.5}$$

Typical tank voltage and current waveforms for *PM* control are shown in figure 5.7, it can be seen that despite the fact that the output was regulated and the H-Bridge retains unity displacement factor operation, soft switching was lost and all IGBTs undergo hard switching. Due to switching loss considerations, this method is not useful when used in isolation.
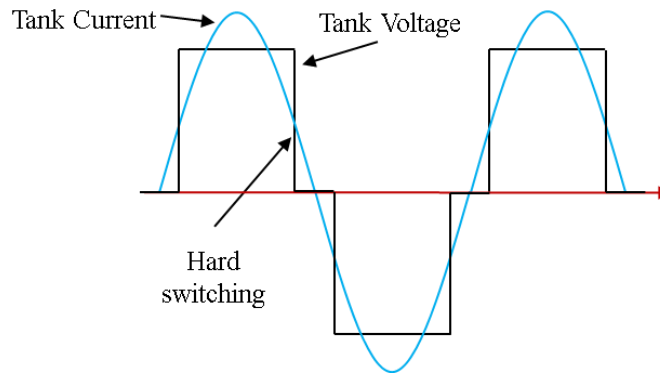
Figure 5.7 Typical waveforms of the PM

From the previous discussion it is evident that utilising *PM* or *FM* alone will not control the output current without excessive switching losses [63]. Therefore, a combined *FM* and *PM* control strategy is considered to overcome the previous disadvantages.

5.2.3 Combined FM and PM Modulation Method

It is clear from the previous analysis that using either the frequency modulation method or the phase modulation method alone cannot regulate the output current or voltage of the converter without significant increase in the switching or/and conduction losses. Therefore, in order to minimise the semiconductor switching losses, a combined *FM* and *PM* modulation (CFPM) strategy is introduced [7, 51, 61, 62].

Figure 5.8 shows the theoretical waveforms using the CFPM strategy.
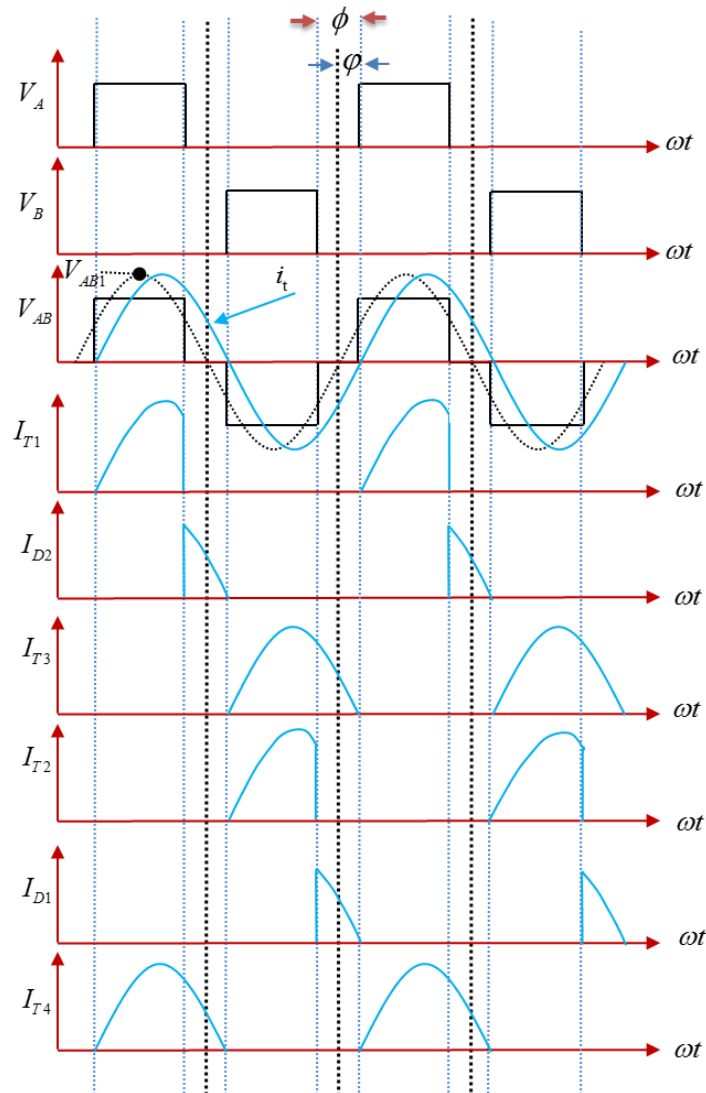
Figure 5.8 theoretical waveforms of FM and PM control strategy

From this figure it can be noticed that the lagging leg B of the H-Bridge always switches at the zero crossing point of the tank current if the condition $\phi = 2\varphi$ is enforced, (where ϕ is the angle between the two legs of the H-Bridge and φ is the phase shift between the fundamental of the tank input voltage V_{AB1} and the resonant tank current) and the leading leg A is always hard switched during turn OFF. An additional capacitive snubber applied on this leg could minimise the hard turn off by slowing the rate of voltage increase, thus achieving ZVS [7, 50, 58].

In figure 5.8, φ given as:

$$\varphi = \frac{\phi}{2} = \arctan[Q.(F - F^{-1})] \tag{5.6}$$

From equations (5.6) and (5.5), the modulation index for the phase modulation, M_I^ϕ , can be derived as given in 5.7

$$M_I^\phi = \cos\varphi = \frac{1}{\sqrt{1 + Q^2(F - F^{-1})^2}} \tag{5.7}$$

The modulation index under combined frequency and phase shift control, M, can be defined as given in (5.8),

$$M = M_I^F \times M_I^\phi \tag{5.8}$$

By substituting (5.2.and 5.8) into (5.8), the modulation index under CFPM modulation can be rearranged as in (5.9) and plotted as in Figure 5.9.

$$M = \frac{F^2}{\left(F^4 Q^2 + F^2 + Q^2 - 2F^2 Q^2\right)} = \cos^2\varphi \tag{5.9}$$
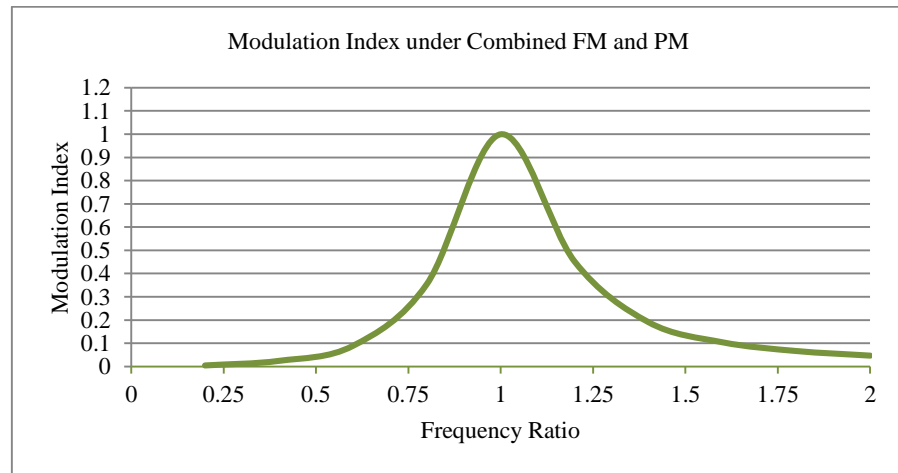
Figure 5.9 the modulation index under combined FM and PM

In order to implement the combined frequency and phase control, the modulation index, M, should be calculated in the first place according to the control signal produced by the proposed controller (will be discussed in chapter 6) and the instantaneous DC-link voltage.

By considering only the fundamental component, the maximum input voltage to the resonant tank $V_{AB_{max}}$ is obtained when ($\phi = 0$) and can be expressed as in (5.10)

$$V_{AB_{max}} = \frac{4V_{DC}}{\pi}$$
(5.10)

It is defined that M is unity when the resonant tank is supplied by maximum square wave voltage. Based on the control demand signal, V_{AB}, and the measured DC-link voltage, V_{DC}, the modulation index, M, can be calculated by using (5.11).

$$M = \frac{V_{AB}}{V_{AB_{max}}} = \frac{\pi V_{AB}}{4V_{DC}}$$
(5.11)

With a defined modulation index (equation (5.11)) and a given quality factor, Q, the corresponding frequency ratio between the switching frequency and resonant frequency, F, can be determined from (5.9). However, in the experimental verification, all calculations are performed in the digital control platform and should be executed within one sampling period. Calculating of F through equation (5.9) incurs significant computation especially within the short sampling period. The solution is given in equation (5.12), where this equation is derived by solving the equation 5.6 and substituting for $M = \cos^2 \varphi$.

$$F = \left(\frac{1}{2}\right)\left(\sqrt{\frac{1-M}{Q^2 M}} + \sqrt{\frac{1-M}{Q^2 M} + 4}\right)$$
(5.12)

Since the implementation of (5.12) on a microprocessor would require significant overhead, this equation can be approximated by using a polynomial curve fitting as shown in figure 5.10 in order to implement it in a digital processor.
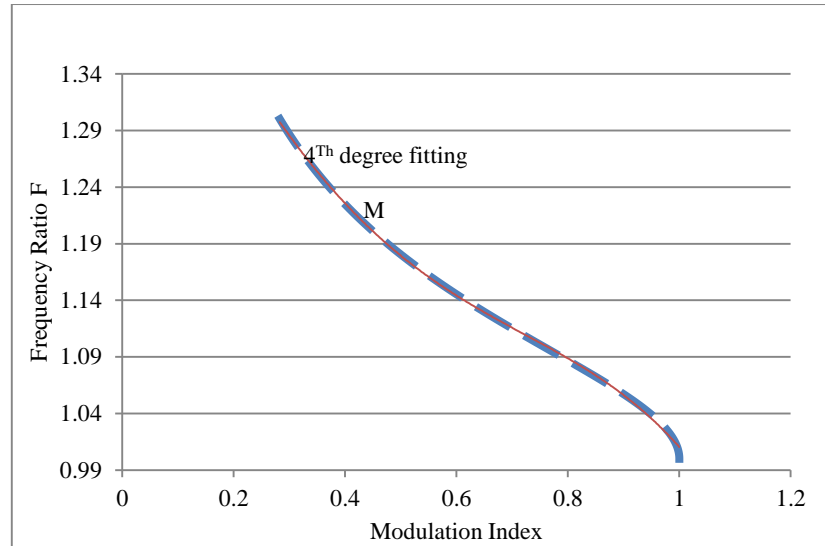
Figure 5.10 Polynomial approximation of F as function in M

In order to make the approximation sufficiently accurate, the order of the polynomial is chosen to be 4. The quality factor Q is assumed to equal 3 to obtain a sinusoidal tank current and the modulation index range from 0.3 to 1. By giving a set of values of modulation index and corresponding values of F, the polynomial fitting equation is given as (5.12).

$$F = -0.5516M^4 + 0.5269M^3 + 0.5897M^2 - 1.1106M + 1.556 \qquad (5.13)$$

It can be seen from figure 5.10 that the selected frequency operating region of the converter is above the resonant frequency to avoid the effect of diode reverse recovery. The two curves are almost identical proving that the polynomial approximation represents the modulation index curve accurately.

5.2.4 Justification of CFPM Modulation Method

In this method the converter output voltage is controlled by variation of the phase shift between the two H-Bridge legs (lagging and leading leg) and the switching frequency is automatically adjusted to ensure the commutation of one bridge leg at zero current (ZCS) and the other bridge leg at zero voltage (ZVS) as shown in figure 5.11.
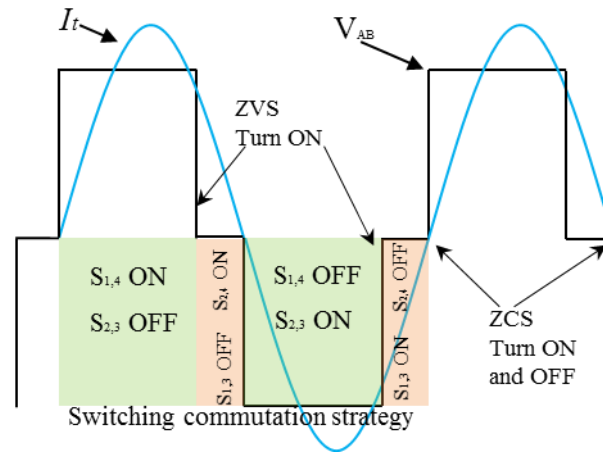
Figure 5.11 the tank voltage and current

One of the main advantages of the CFPM control is that it narrows the switching frequency variation in relation to the handled power. This will overcome the issue of high losses in the *FM* control during low output power operation. Another advantage of this strategy is that two different switch technologies can be employed; one could use switches with low conduction losses characteristics on the lagging leg, and switches with low turn OFF losses characteristics on the leading leg [50] . Ideally the antiparallel diodes of the switches S3 and S4 (in figure 5.1) never conduct, however, due to the necessity of implementing a dead-time between both switches in a practical implementation the commutation cannot be triggered exactly at zero current. therefore, these antiparallel diodes have to be implemented but they conduct only for a very short time [62].

A disadvantage of the CFPM strategy is an uneven current distribution between both legs of the H-Bridge inverter. This is due to the fact that the lagging leg switches are conducting current almost 50% of the switching period, while the turn ON interval of the leading leg switches is dependent on the phase shift between the legs [62]. Another drawback with existing combined frequency and phase modulation methods such as those described in [3, 10, 50, 62, 63], although good for variable output voltages, is that they assume a constant quality factor *Q* and therefore are not directly applicable to variable load conditions. Previous work has not attempted to address the limitation when the load is variable and/or nonlinear. Therefore, it can be difficult to ensure zero current switching (ZCS) via phase and frequency control when the load is variable.

5.3 Modulation with Variable Load Operation

The modulation of resonant converters whilst maintaining soft switching when the load varies is a challenging issue. It is crucial that switching occurs at the optimum moment (i.e. points giving soft switching transitions) in high power high voltage load resonant converters. This exerts low electrical stress on the semiconductor devices and provides high system conversion efficiency.

 The aforementioned combined frequency and phase modulation could be employed to effectively modulate the load resonant converter with fixed load conditions (fixed Q based CFPM modulation). However, some industrial applications which have different output requirements need to operate with a variable load condition. This is a challenging situation for the resonant converter as the soft switching operation cannot be ensured because the equivalent load resistance seen by the converter is varying and so the CFPM modulation can no longer ensure soft switching. As a result of this, the associated switching loss is increased and the device switching transition stresses are compromised, at times to unacceptable levels.

In this research, for a resonant converter dealing with the variable load condition (e.g. cavity magnetrons), a novel control methodology has been developed and designed which is able to achieve ZCS over a range of values of Q (2 to 5). This is a vital requirement when the driven load is a magnetron and the RF output power is variable due to application requirements.

The method considered utilises a 3D lookup table which characterises the soft switching of the converter via a Q estimation method. The correct voltage and output frequency are selected to control the magnetron current whilst achieving ZCS on the lagging leg of the converter. the leading leg switching losses are also minimised by using lossless (capacitive) snubber to achieve ZVS [66].
The load quality factor Q can be estimated through the load voltage/current characteristics. By combining Q with the DC link measurement and the modulation index produced by the feedback current control loop, based on equation (5.12), the demand frequency ratio F and the required switching frequency can be derived. The corresponding phase shift that retains soft switching can also be derived using equation (5.6). Consequently, the variable

load influence on the soft switching scheme can be overcome. This novel control methodology is named as a variable Q based CFPM modulation.

In order to use the 3D look up table, a pre-calculation of the frequency ratio points is required across the entire converter operating range. Based on equation (5.12) a three dimensional surface of the frequency ratio F is plotted as a function of the modulation index M and the quality factor Q as shown in figure 5.12. Where the quality factor is represented by the x-axis (varying from 2 to 5); the modulation index is represented by the y-axis (varying from 0.5 to 1); and the corresponding frequency ratio value is represented by the z- axis.
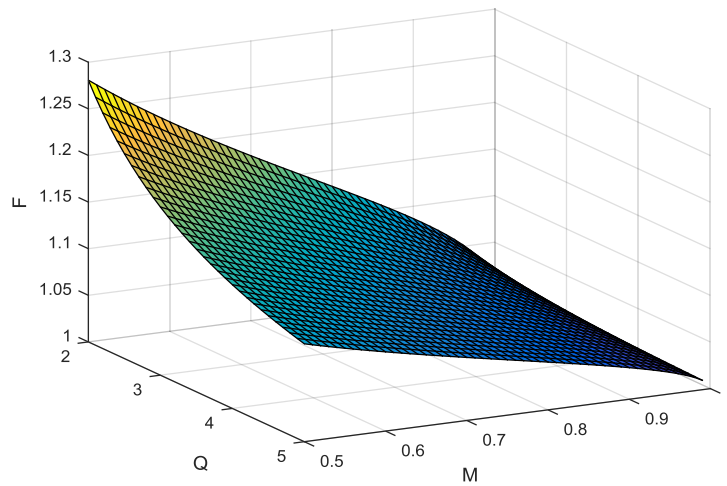
Figure 5.12 the nominal frequency as a function of the M and Q

The surface fitting tool box of the MATLAB is utilised to fit this surface with a 4x4 polynomial equation. This guarantees a fast and accurate evaluation of the frequency ratio for practical implementation of digital control. The surface fitting approximation equation is obtained as:

$$
\begin{aligned}
F = \quad & 2.195 - 0.9689Q + 1.754M + 0.2068Q^2 + 1.221Q \times M - 8.977M^2 \\
& - 0.02326Q^3 - 0.1345Q^2 \times M - 0.7746Q \times M^2 + 0.48M^3 + \\
& 0.0009199Q^4 + 0.009949Q^3 \times M - 0.0007299Q^2 \times M^2 + \\
& 0.3496Q \times M^3 - 4.28M^4
\end{aligned}
\tag{5.14}
$$

Here, M is the modulation index and F is the frequency ratio which defined as:

$$F = \frac{f}{f_o} \tag{5.15}$$

Where f, is the switching frequency and f_o is the resonance frequency of the circuit. The phase-shift between the two legs of the Full-Bridge resonant converter (ϕ) is obtained as

$$\phi = 2 * \arctan\left(Q\left[F - F^{-1} \right] \right) \tag{5.16}$$

Initial simulation work has been undertaken using PLECS. Equations (5.14) and (5.16) are implemented using a C-Script code in PLECS in order to produce the switching signal patterns for the SRSL converter.

In order to confirm the validity of equation (5.14), equation (5.12) is calculated at various discrete values of Q and is compared with the results of the surface fitting approximation equation. As shown in figure 5.13, they have been found to match closely.
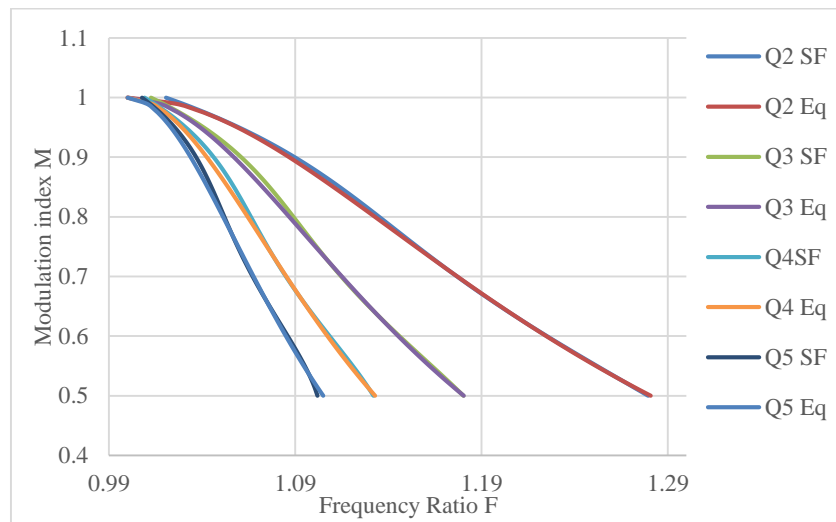
Figure 5.13 results from analytical compared to the surface fitting

Figure 5.14 illustrates the relationship between the modulation index M and the frequency ratio F at different values of Q. it can be seen that at specific values of M, the larger the value of Q, the closer the switch frequency is to the resonant frequency.
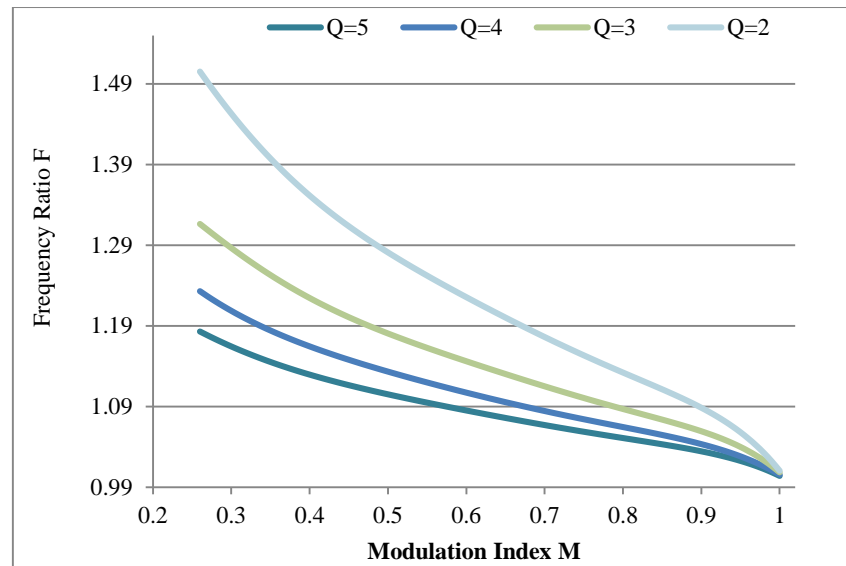
Figure 5.14 modulation index m vs. the nominal frequency F at different *Q*'s

5.3.1 Lagging Leg Switching Losses

As previously mentioned, if the fixed *Q* based CFPM modulation is used, the lagging leg of the H-Bridge can completely maintain both turn ON and OFF lossless switching when the load is assumed to be constant at nominal quality factor, Q_{nom} (the correct value of *Q* that the converter is originally designed for). It can be seen from the theoretical waveforms for a resonant tank and lagging leg switch, S4, under fixed *Q* based CFPM modulation in Figure 5.15 that this leg will always switch at the zero crossing point of the tank current, if the conditions $\varphi_{nom} = \dfrac{\phi_{nom}}{2}$ and the tank quality factor $(Q = Q_{nom})$ are achieved.

Note that the other switch S3 in the lagging leg has the same typical waveforms. This means soft switching is maintained for all transitions of the lagging leg.
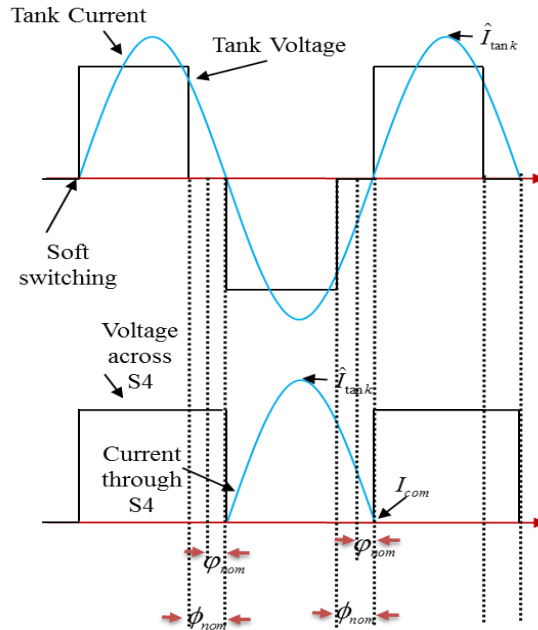
Figure 5.15 theoretical waveforms for tank and lagging leg switch S4 at Q_{nom}

However, if Q is changed $(Q \neq Q_{nom})$ with F and ϕ_{nom} maintained constant, the phase shift of the tank will be changed to a new φ and the waveforms will be as illustrated in figure (5.16).
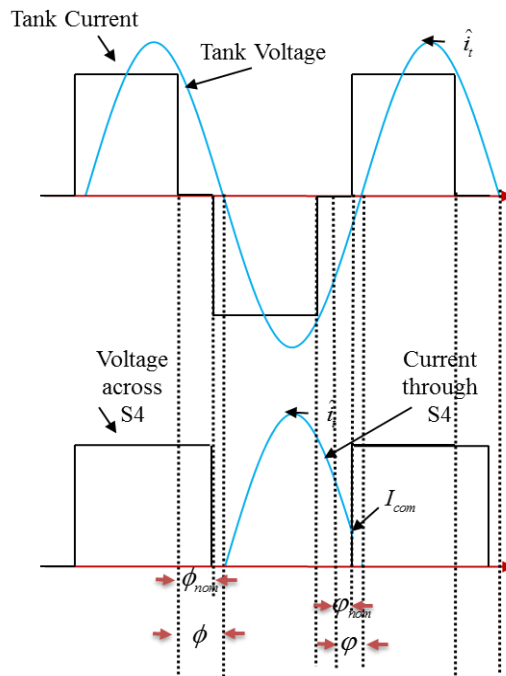
Figure 5.16 theoretical waveforms for tank and lagging leg switch S4 at Q

From figure (5.16) it can be seen that the current through S4 turns OFF at sizable current when the load varies since the tank phase shift, φ, is changed according to equation (5.6). Moreover, it can be observed that the current at the commutation (I_{com}) can be given by:

$$I_{com} = \hat{i}_t \sin(\varphi - \varphi_{nom}) \tag{5.17}$$

Where ($\hat{i}_t$) is the peak tank current and it is given as in (5.18) (Appendix B).

$$\hat{i}_t = \frac{4MQV_{DC}}{\pi\sqrt{\dfrac{L}{C}}} \tag{5.18}$$

Where V_{DC} is the DC link voltage and M is the modulation index. In the fixed Q based CFPM modulation, the nominal modulation index (M_{nom}) is given by

$$M_{nom} = \cos^2 \varphi_{nom} \tag{5.19}$$

By substituting equations 5.18 and 5.19 into 5.17, the commutation current at any value of Q is given by

$$I_{com} = \left(\frac{4V_{DC}Q}{\pi\sqrt{\dfrac{L}{C}}}\right)\left(\frac{\left(\dfrac{Q}{Q_{nom}}-1\right)\left(\sqrt{1-M_{nom}}\right)}{\sqrt{\left(1+(\dfrac{Q}{Q_{nom}})^2\right)\left(\dfrac{1}{M_{nom}}-1\right)}}\right) \tag{5.20}$$

A mathematical derivations for the peak tank current $\hat{i}_t$ and the commutation current I_{com} are detailed in Appendix B.

The current (absolute) at commutation $\left|I_{com}\right|$ on the lagging leg is plotted in figure (5.17) when the parameters of table 4.1are used and set Q_{nom} =3, M_{nom} = 0.75 and Q ranges from (2-5). Note the commutation current is normalised to the peak tank current of the converter (375A at Q=3 and M=0.75).
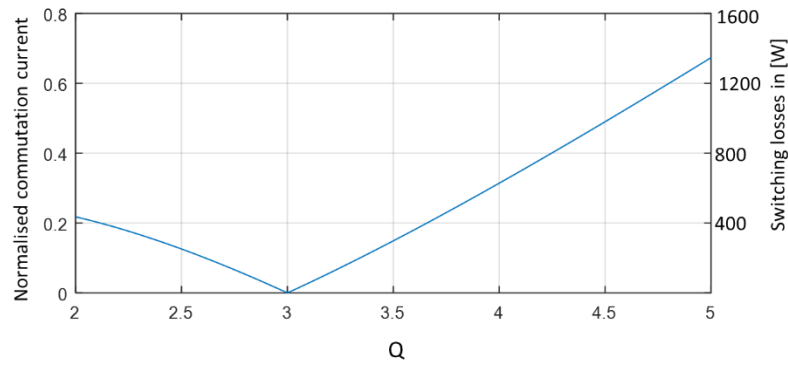
Figure 5.17 lagging leg commutation current

It is important to note here that the commutation current is zero when the load is fixed at ($Q=Q_{nom}$). However, when the load is changed ($Q{\neq}Q_{nom}$), the commutation current will excessively increase, means the lagging leg switching losses will also increase, where the commutation current is directly proportional to the switching losses. Based on datasheet of the selected IGBT (800-A dual switch IGBT modules (DIM800DDM17-A000)), the switching losses are shown in figure (5.17)

However, If the variable Q based CFPM modulation is used to drive the converter, the correct F and φ are always tracked by obtaining the correct online Q when the load is changed over its range from 2-5. In this case Q is always equal to Q_{nom}. By applying this ($Q=Q_{nom}$) in equation 5.20, the commutation current is always zero. Theoretically, this indicates that the lagging leg is always commutating at ZCS.

5.3.2 Leading Leg Switching Losses

When the series resonant converter with the variable Q based CFPM modulation is operated, the switches in the lagging leg always maintain ZCS. However, the leading leg is turned OFF when a significant current is flowing in the active device. A theoretical waveforms for the leading leg switch, S1, and the resonant tank are shown in figure (5.18). S2 in the leading leg has the same typical waveform of S1.

65
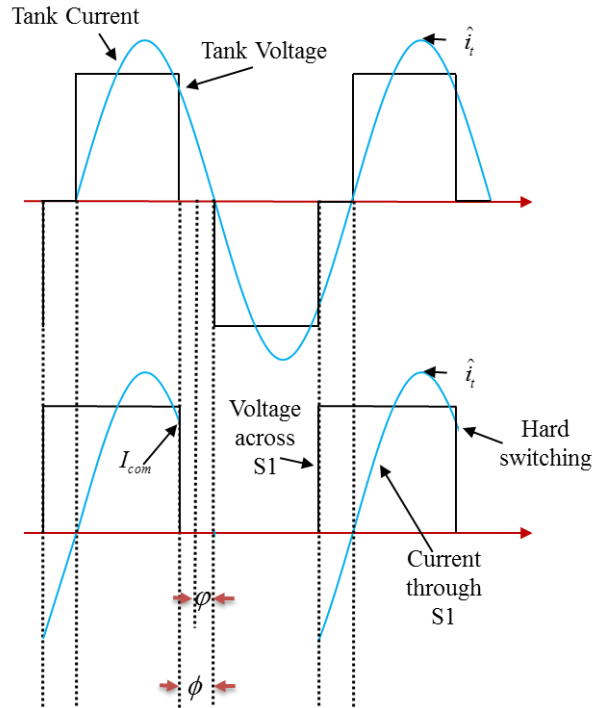
Figure 5.18 theoretical waveforms for the leading leg switch, S1, and the resonant tank

It is apparent in Figure 5.18 that the S1 has soft switch ON and hard switch OFF. To calculate switching losses, the leading leg commutation current I_{com} has to be firstly obtained. It is worth noting that I_{com} is a function of the peak tank current $\hat{i}_t$ and the tank phase angle between the two legs, ϕ, as given in (5.21).

$$I_{com} = \hat{i}_t \sin(\pi - \phi) = \hat{i}_t \sin(\phi) \tag{5.21}$$

By substituting (5.18) into (5.21), the commutation current can be written as in (5.22). (Appendix B).

$$I_{com} = \left(\frac{8MQV_{DC}}{\pi\sqrt{\frac{L}{C}}} \right) \left(\sqrt{M}\sqrt{1-M} \right) \tag{5.22}$$

It is important to note from equation (5.22) that the commutation current is a function of the modulation index and the quality factor. In conjunction with the given parameters in (Table 4.1) and different ranges of the modulation index

(0.5-0.99), figure (5.19) depicts the normalised commutation current when the load varies (Q from 2 to 5). In this figure, the commutation current, I_{com}, is normalised to the peak current $\hat{i}_t$.
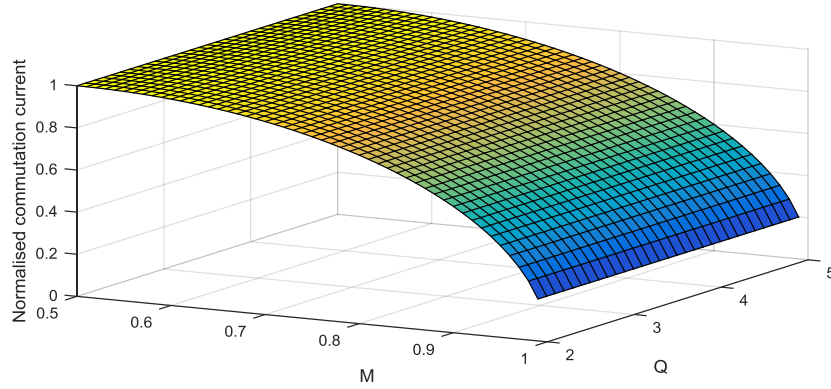
Figure 5.19 the normalised commutation current along (Q from 2 to 5)

As can be seen, the highest value of commutation current is when the modulation index is 0.5 regardless the value of Q. Thus, the converter should be operated away from M=0.5 where the ratio of $\dfrac{I_{com}}{\hat{i}_t}$ is maximum.

The relationship between the commutation current and the output power, P_{out}. Can also be formed as shown in (5.23). The mathematical derivation are detailed in Appendix B.

$$\frac{I_{com}}{P_{out}} = \frac{\pi}{V_{DC}}\left(\sqrt{\frac{1}{M}}-1\right)$$ (5.23)

This relationship is completely independent of the Q, the tank parameters, the operating frequency and the size of the converter, it just depends on M and V_{DC}. Therefore, for example, if a 100kW converter is designed, choosing the transformer ratio so that M=0.75 when the power is 100kW and V$_{DC}$= 560V, the commutation current will be 320A without considering any other design details. That will give a good indication to the size of the required snubber before any detailed design is done.

In terms of the leading leg switch loss calculations, the switching losses for one switch in the leading leg, $P_{loss,}$ can be derived as given in (5.24). (Appendix B).

$$P_{loss} = I_{com}\, V_{DC}\, E_{off}^{n}\, f \tag{5.24}$$

Where, E_{off}^{n} is the normalised turn-off energy loss which is obtained from the selected IGBT module datasheet and measured by (nJ/VA) and, f, is the switching frequency. Based on datasheet of the selected IGBT (800-A dual switch IGBT modules (DIM800DDM17-A000)), the normalised turn-off energy loss is (500nJ/VA at 125C°).

Figure (5.20) demonstrates the leading leg switching losses ($2P_{loss}$) when the load varies (Q from 2 to 5). The power losses is calculated based on the parameters given in table 4.1 and M is set at (0.75).

Figure 5.20 the leading leg switching losses ($2P_{loss}$)

Clearly, the leading leg switching losses are high for the selected IGBT module due to the large turn OFF commutation current, which often make this option practically unfeasible if a snubber circuit is not utilized.

The relationship between the leading leg switching losses, $2P_{loss}$, and the output power, P_{out}. Can also be formed as shown in (5.25) (Appendix B).

$$\frac{2P_{loss}}{P_{out}} = \left(2\pi \sqrt{\frac{1}{M} - 1} \right)(E_{off}^{n})(f) \tag{5.25}$$

For example at $Q=3$, P_{out} is 100kW and the loss according to figure 5.20 is 4.1kW. Thus, agree with equation (5.25) which the parameters used previously equivalent to 4.1%.

It is possible to reduce the turn OFF losses by placing a suitable capacitive snubbers across the IGBT switches of leading leg [58]. The main function of these capacitors are to delay the voltage rise during the IGBT turn OFF commutation and hence achieve an operating condition that is close to ZVS. In leg A the snubber capacitor of the device which is turned OFF is charged; while the other capacitor in the same leg is discharged. A dead time is required between turning OFF *S1* and turning ON *S2* to avoid DC link 'shoot-through'. Figure 5.21 illustrates the current through the leading leg, the red lines shows the flow of the load current when S1 is ON and S2 is OFF (Mode 1), the green lines show the flow of the load current when S1 is OFF and S2 is ON (Mode 2) and the blue lines show the flow of the load current during the interval of the dead time, S1 and S2 are OFF, (Mode 3). This based on assumption that the load current is continuous during the dead time interval.
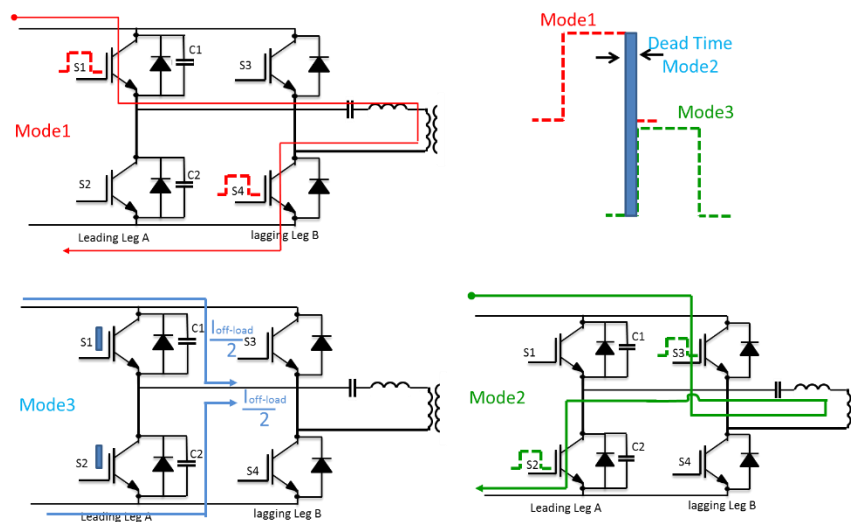
Figure 5.21 the current through the leading leg

This dead time should be large enough to completely discharge C_2 at the lowest turn OFF current. The snubber capacitor should be chosen large enough to slow down the voltage rise for the largest turn OFF current I_{com}^{max} (in this case I_{com}^{max} is the commutation current when $Q=5$ if the Q range (2-5) is considered). At the same time it should be small enough to be completely discharged within the prefixed delay time by smallest turn OFF current I_{com}^{min} in this case I_{com}^{min} is the commutation current when $Q=2$. The snubber capacitor (C) value can be obtained as:

$$C = \frac{I_{com}^{max} t_{fall}}{2V_{DC}} \tag{5.26}$$

Where, t_{fall} is the typical device current fall time obtained from the IGBT module data sheet.

The dead time (T_D) required between *S1 and S2* can be obtained as:

$$T_D = \frac{2V_{DC}C}{I_{com}^{min}} \tag{5.27}$$

It should be noted that a minimum dead time is set to avoid device shoot-through. Additional dead time can be used at operating points where full snubber capacitor discharge cannot be achieved.

When the snubber capacitor is utilised to slow down the voltage rise during the commutation in order to reduce the leading leg switching losses, the voltage and current transition waveforms during the turn OFF are considered as shown in figure (5.22).
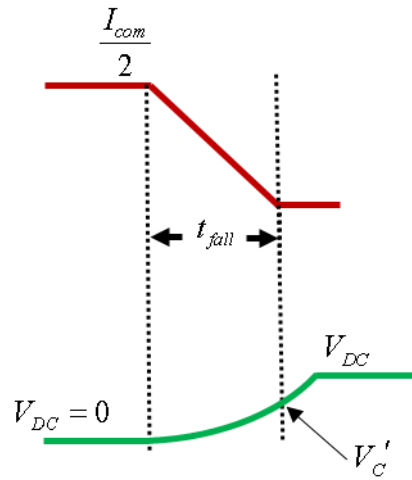
Figure 5.22 transition waveforms during turn OFF without snubber

Where, V_C' is the voltage on the snubber capacitor when the commutation current is zero and it is given as in 5.28.

$$V_C' = (\frac{I_{com}}{2})(\frac{t_{fall}}{2C}) \tag{5.28}$$

The turn OFF switching loss for one switch in the leading leg when the capacitive snubber is utilised can be derived as given in (5.29). (Appendix B)

$$P_{loss} = (\frac{I_{com}V'_C t_{fall}}{24})(f)$$ (5.29)

Figure 5.23 demonstrates the leading leg switching losses ($2P_{loss}$) when the capacitive snubber is used and the load varies (Q from 2 to 5). The power losses are calculated based on the parameters given in table 4.1 with M set at 0.75.

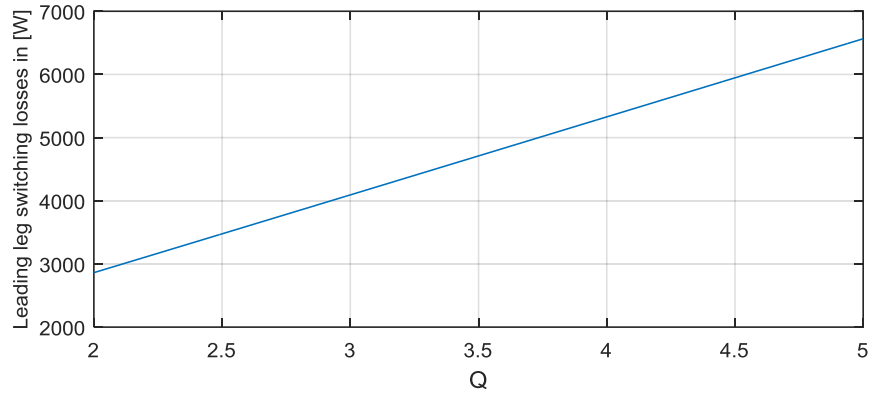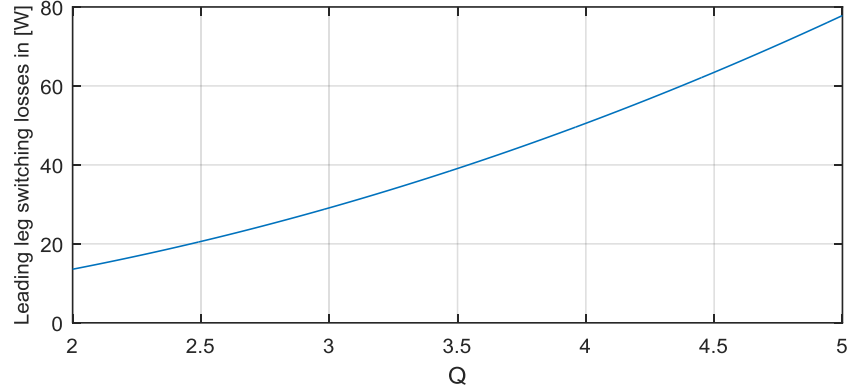Figure 5.23 the leading leg switching losses ($2P_{loss}$) with using snubber

As it can be seen that, by utilising the designed snubber capacitor and dead time, switching losses is largely reduced compared to the results in figure 5.20 and becomes negligible.

Also, the relationship between the leading leg switching losses, $2P_{loss,}$ and the output power, P_{out} Can be derived as formed in (5.30). The mathematical derivation are detailed in Appendix B.

$$\frac{2P_{loss}}{P_{out}} = \frac{\pi}{12}\frac{Q}{Q_{max}}\left(\sqrt{\frac{1}{M}}-1\right)t_{fall}\cdot f$$ (5.30)

Where, Q_{max} is the maximum quality factor in this case is equal 5. With the parameters used previously to draw figure 5.23, the $\frac{2P_{loss}}{P_{out}}$ is equal to 0.030%, the impact of the loss will be very small compared to 5.20 and can be neglected.

5.4 Quality Factor Estimation Methods

To implement the variable Q based CFPM modulation, it is necessary to estimate the quality factor Q accurately when the load varies. In this section, three different approaches are discussed in order to practically estimate the Q. Figure 5.24 shows a typical DC-DC SRSL resonant converter. In this converter the quality factor Q is given as:

$$Q = \frac{\omega_o L}{R_{eq}}$$
(5.31)

Where ω_o is the resonant frequency, L is the tank inductance and R_{eq} the equivalent ac load resistive. From this equation it can be deduced that the only variable component is the R_{eq}.
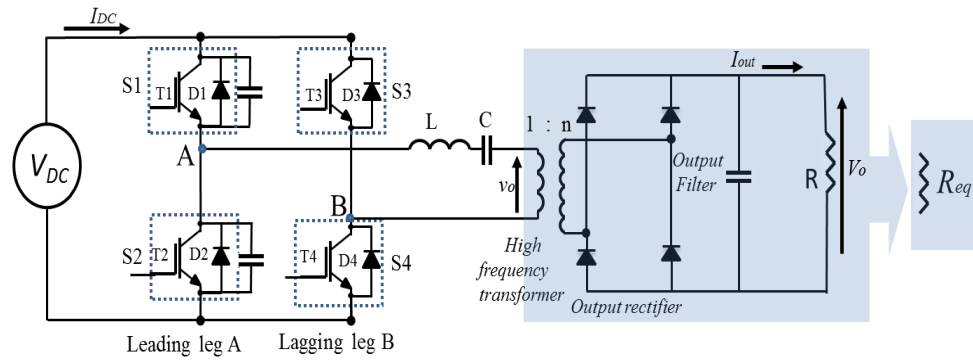
Figure 5.24 a typical DC-DC SRSL resonant converter

As discussed previously in chapter 4, the equivalent ac resistance R_{eq} is given as:

$$R_{eq} = \frac{8}{\pi^2 n^2} R = (\frac{8}{\pi^2 n^2})(\frac{V_o}{I_{out}})$$
(5.32)

Where R is the load DC resistance, V_o is the load, I_{out} is the output current and n is the transformer turns ratio.

- The first approach for Q estimation is by measuring the output voltage V_{out} and current I_{out}.

By substituting equation 5.32 into 5.31 the quality factor can be estimated by equation 5.33.

$$Q = \frac{\omega_o L \pi^2 n^2 I_{out}}{8 V_o}$$
(5.33)

Although this method is conceptually simple, there are some practical implementation issues. The output current is relatively easy to measure with the appropriate isolation. However, the output voltage V_o is in kilovolts. Measuring the high voltage requires special methods. The most common method in any DC-DC converter's feedback system is a high voltage resistive feedback divider [67]. As shown in figure 5.25, the high voltage resistive feedback divider consist of a resistive divider network which divides the output voltage to a level low enough to be processed by the control platform.
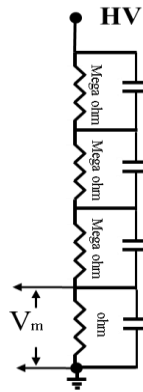
Figure 5.25 high voltage resistor divider

The high voltage feedback divider is a source of stability error due to the large resistance of the feedback resistors. In order to reduce power dissipation in the circuit and reduce the effects of temperature change due to self-heating, values of greater than Mega-Ohms are common. In addition an isolation amplifier may be needed.

- The second approach for Q estimation is by measuring both the input power P_{in} and the output current I_{out}. The input power is given by

$$P_{in} = I_{DC}.V_{DC} \tag{5.34}$$

Where the V_{DC} is the DC link voltage and I_{DC} is the input DC current to the H-Bridge inverter. By assuming the converter is ideal, the input power P_{in} can be written as

$$P_{in} = I_{out}^2 R \tag{5.35}$$

Based on equations 5.34 and 5.35 the load DC resistance is given as

$$R = \frac{V_{DC}.I_{DC}}{I_{out}^2} \tag{5.36}$$

Substituting equations 5.36 and 5.32 into 5.31 the quality factor Q is given as

$$Q = (\frac{8\omega L I_{out}^2 n^2 \pi^2}{V_{DC} I_{DC}})$$ (5.37)

To practically measure all these components in the equation (5.37), two current transducers and one voltage transducer are required. This approach is not appropriate to estimate Q due to the difficulties of measuring the input current I_{DC} cycle by cycle. Moreover, in practice the converter is not ideal as assumed and the input power is not equal the output power.

- The third approach for Q estimation is by measuring the voltage on the primary side of the HV transformer v_o, and the tank current I_{out} of the *SRSL* resonant converter. In this case the R_{eq} is given as:

$$R_{eq} = \frac{v_{o(RMS)}}{i_t}$$ (5.38)

Where, $v_{o(RMS)}$, is the *RMS* value of the voltage on the primary side of the *HV* transformer. It is known that the v_o, is square-wave and high frequency voltage. The $v_{o(RMS)}$, is given by:

$$v_{o(RMS)} = (\frac{4v_o}{\pi})(\sqrt{2}) = 0.9 v_o$$ (5.39)

The relationship between the output current I_{out} and the tank current i_t is given by:

$$I_{out} = \frac{2\hat{i_t}}{n\pi}$$ (5.40)

 Substituting equations (5.38, 5.39 and 5. 40) into 5.31 the quality factor Q is given as

$$Q = (\frac{\omega_o L}{0.9 v_o})(\frac{n\pi I_{out}}{2\sqrt{2}})$$ (5.41)

In practice v_o is not a perfect square wave and would need to be sampled at a high frequency to obtain an accurate measurement of RMS value. Therefore, a specific voltage transducer with a very fast response time is required. To satisfy this requirement, a differential probe can be utilised. Some probes for example (Differential Probe for Power Measurement- Model 4235 from S J electronics) have a bandwidth of 50MHz and the rise time is 7ns which fulfil the requirements. A LEM-LA 55-P current transducer can be used to measure the output current I_{out}.

Based on the previous discussed the third approach is the best solution to estimate the Q compared with the first approach where high voltage measurement is required and the second approach where input current needs to be measured and there are errors due to converter losses.

5.5 Implementation of the Variable Q Based CFPM Modulation

It is important now to look at how to implement the Variable Q based CFPM modulation method. The first step is to obtain the modulation index, M, by using equation (5.11). The second step of the implementation is to utilise the equation 5.41 in order to track online the value of the Q to be used in the frequency ratio F calculations.

The second step is to calculate the frequency ratio between the switching frequency and the resonant frequency from equation (5.14).

As result of acquiring the Q and F, the corresponding control phase-shift, ϕ, can be obtained by multiplying equation (5.6) by 2 to make sure that ϕ between the diagonal pair switches of the H-Bridge, is twice the phase-shift φ between the fundamental tank voltage, V_{AB}, and the tank current i_t.

In practice a digital platform based on DSP/FPGA is used to implement this method. The FPGA is used to generate a series of triangular waves with amplitude of ± 1. The generation of the triangular wave is detailed in Chapter 7. Figure (5.26) illustrates the implementation of the Variable Q based CFPM modulation method.

In the time period t_1 the modulation index M_1 is obtained by solving equation (5.11). Also, the online Q is tracked from equation (5.41). The switching frequency f_1 is calculated by using the surface fitting equation. Consequently ϕ_1 is obtained through equation 5.14. At the time range t_2, the load is changed, given an updated Q, switching frequency, f_2 and phase shift, ϕ_2. Instantaneously, the frequency of the triangular wave is changed to f_2 (by

varying the slope) and compared with the new amplitude reference $\pm A_2$. Consequently, this allows both the frequency and duty cycle of the tank input voltage to be adjusted accordingly.
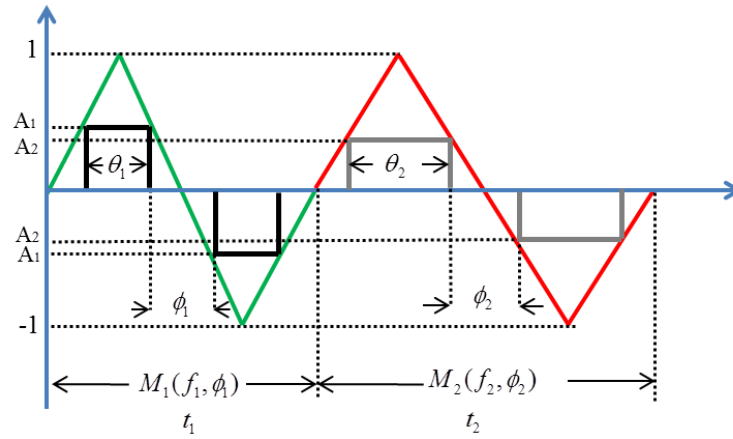
Figure 5.26 implementation of the Variable Q based CFPM modulation method

In order to find the gate signal patterns with the desired frequency and duty cycle, the following relationship between ϕ_1 and A_1 is expressed from figure 5.26 as

$$\frac{A_1}{\left(\dfrac{\phi_1}{2}\right)} = \frac{1}{\left(\dfrac{\pi}{2}\right)} \tag{5.42}$$

The overall block diagram of the Variable Q based CFPM modulation method is shown in figure 5.27.
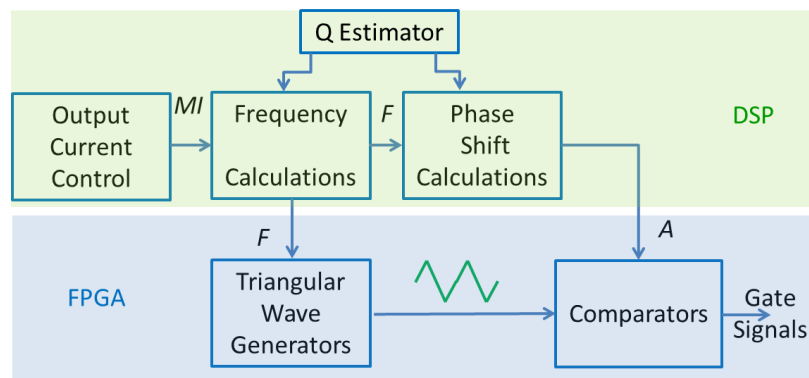
Figure 5.27 the block diagram of the Variable Q based CFPM modulation

A C-code was written in PLECS C-Script for the previous steps of the implementations in order to be used in the simulation model for the proposed

control strategies (variable Q based CFPM). Moreover, these steps will be used in the hardware implementation (more details will be provided in chapter 7).

5.6 Simulation Results

The simulation was set up as shown in to Figure 5.28, with a fixed DC source representing the rectified supply, and an ideal transformer for voltage scaling and isolation.
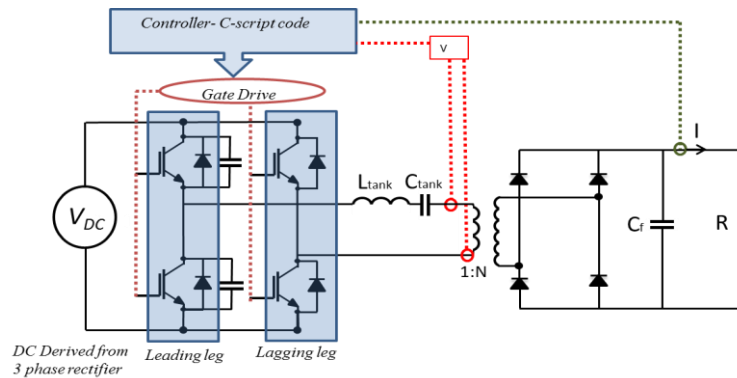
Figure 5.28 simulation set up circuit

The power converter design has been developed based on the power supply specifications and design results in table 4.1. A variable resistive load was utilised in this chapter in order to verify the proposed control strategy.

5.6.1 Variable Resistive Load Simulation Results

From the converter point view, the variable *RF* output requirements behave like a variable resistive load, so the initial simulation work is undertaken by representing the load as a variable resistor (variable Q). In the proposed modulation (variable Q based CFPM) the soft switching points for Q ranging from 2 to 5 are pre-calculated and represented in the normalised equation (5.14). Hence, during the converter modulation, the soft switching point can be tracked by obtaining the online value of the variable load resistance and the control actuation signal. In the PLECS simulation this equation was utilised as a C-Script code to determine the switching signals patterns of the SRSL converter. With the variable resistive load and open loop controller, the SRSL power converter will produce variable quality factor Q at a constant voltage.

In the early stage of this project the modulation index was set up at a fixed value (*M*=0.75), and there was no control actuation feedback signal to regulate the output current. In order to track the soft switching point and achieves *ZCS* on the lagging leg of the converter continuously, the *Q* estimator and the normalised surface fitting equation were implemented in C-Script code. Equations (5.14 and 5.41) were implemented in a PLECS C-Script block to design the switching signals patterns of the SRSL converter. Figure 5.29 shows the simulation circuit set up for the open loop controller.
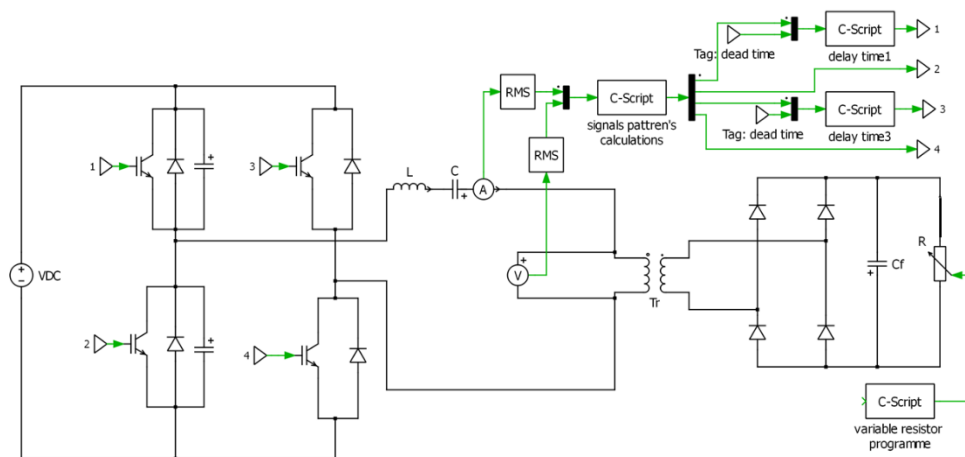
Figure 5.29 Simulation circuit set up for open loop controller

Figure 5.30 shows the simulation results of the output voltage and current when the load is changed (from Q=3 to Q =5).
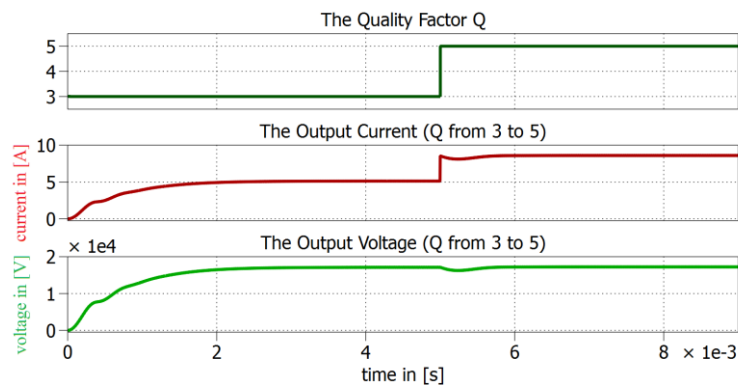
Figure 5.30 simulation results for the output voltage and current

It can be seen from the above figure that the converter produces a variable current and constant voltage which results in a variable *Q* when the resistive load is changed.

Figure 5.31 shows collector current and collector-emitter voltage on the lagging leg with both Fixed and variable Q based CFPM modulation method at $Q=3$. In this case using both methods maintain soft switching because the fixed Q method originally designed based on the assumption of $Q=3$.
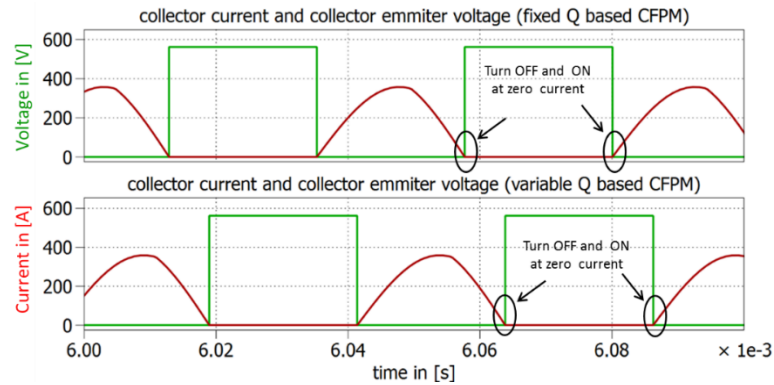
Figure 5.31 the collector current and collector-emitter voltage at $Q=3$

However, by changing the load at $Q=5$ as shown in figure 5.32, the converter maintains soft switching when variable Q based CFPM is used, but hard switching if the fixed Q based CFPM is used.
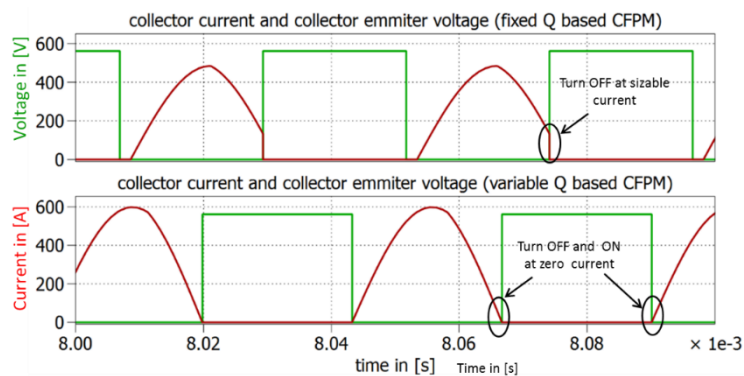
Figure 5.32 the collector current and collector-emitter voltage at $Q=5$

It can be seen that using fixed Q based CFPM modulation method results in hard switching turn OFF when the load is changed to ($Q > 3$). With the proposed variable Q based CFPM modulation method the soft switching can be ensured at all switching transitions along the range of (Q from 3 to 5).

Figure 5.33 shows the lagging leg turn ON current (which is directly proportional to the switching loss) when the load is changed to $Q = 2$.
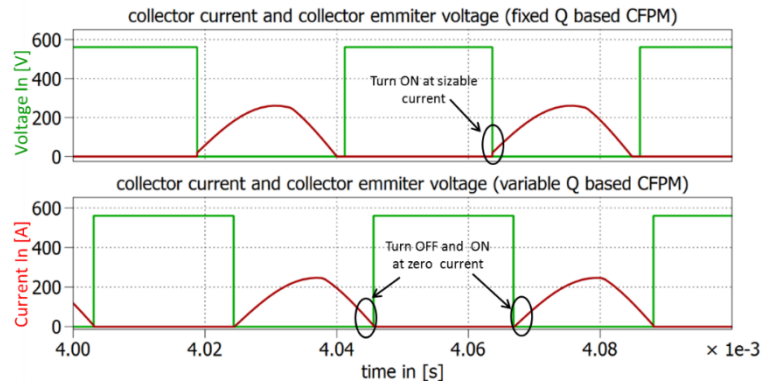
Figure 5.33 the collector current and collector-emitter voltage at Q=2

It can be seen that using Fixed Q based CFPM modulation method results in hard switching turn ON when the load is changed to ($Q < 3$). It is important to note here in figure 5.33 that when fixed Q based CFPM method is used and Q is changed to (Q<3) the circuit is exhibits the characteristics of a capacitive circuit, where this operation causes the current of the resonant circuit to commutate from a diode of one switch to transistor of the other switch. This can lead to diode reverse recovery stress when the diode is turned off. With the proposed variable Q based CFPM modulation method the soft switching can be ensured at all switching transitions along the range of (Q from 2 to 3).

Figure 5.34 shows the simulation results for tank voltage and current when the load is ramps from Q=3 to Q =5. Ramp demand is more realistic than a step demand in the considered application
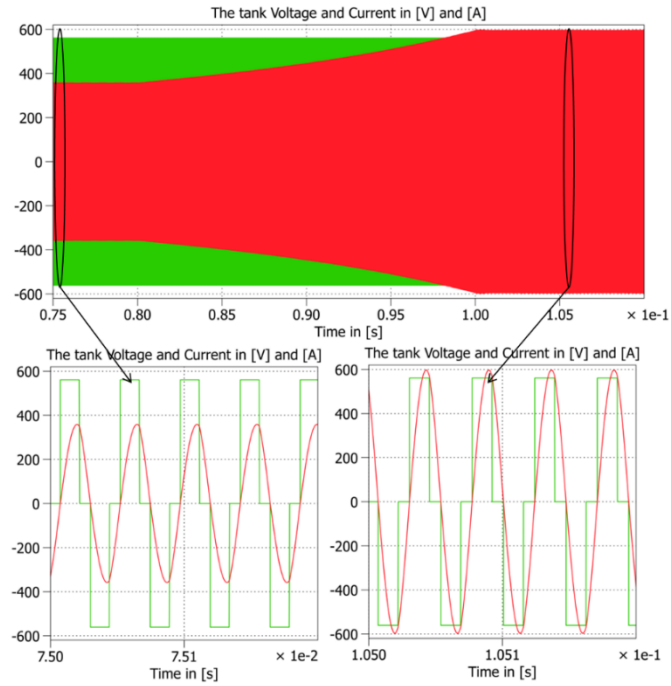
Figure 5.34 tank voltage and current when the load is changed from *Q*=3 to 5

From figure 5.34 it can be seen that when the load varies the variable *Q* based CFPM modulation method chooses the correct frequency and phase shift which leads to soft switching for the switches of the lagging leg. However, the switches in the leading leg require an additional snubber capacitor to achieve ZVS turn-off.

Figure 5.35 shows the simulation results of the leading leg switching losses without using the snubber capacitor.
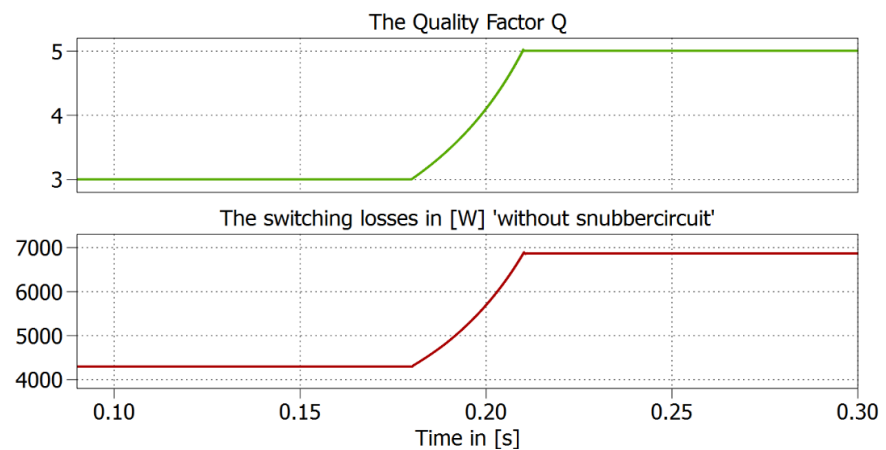
Figure 5.35 simulation results of the leading leg switching losses without snubber

81

It can be seen that without the snubber circuit, the switching losses increased significantly along the range of Q; which is very high and unacceptable. When the designed snubber capacitor are placed across the switches of the leading leg the switching losses is dramatically reduced as depicted in figure (5.23)

5.7 Conclusion

In this chapter, different modulation methods for the proposed converter were introduced. The variable Q based CFPM modulation method were chosen to control the SRSL converter and to apply the zero current switching (ZCS) while the load varies, so the soft-switching of semiconductor devices can be always maintained and high conversion can be achieved. A novel analytical expression for the normalised frequency as a function in the power quality and the modulation index is obtained in order to be used to gain soft switching when the load is changed. The control strategy is verified by analytically comparing the novel variable Q based CFPM modulation method to the fixed Q based CFPM modulation method and by the PLECS simulations.

It was found that when the proposed control methodology was used the lagging leg always maintains soft switching despite the load being changed. However, without using the designed snubber circuit, the leading leg was turned OFF in the hard switching mode. By utilising the designed snubber circuit, the leading legs' switching losses were significantly reduced.

As observed in the simulation results a significant reduction in the switching losses when the novel variable Q based CFPM modulation is used to drive the SRSL converter with variable load. The comparison of the results produced by the use of the novel variable Q based CFPM modulation method and using the fixed Q based CFPM modulation method prove that the former is correct and accurate. In the next chapter, the modelling technique is investigated in order to design the closed loop control system.

Chapter 6

MODELLING AND CONTROL STRATEGY

6.1 Introduction

In this chapter, the modelling process is investigated and the closed loop current controller is designed. The modelling process is a very important step in the dynamic analysis and in the design of resonant converters [68]. In the case of PWM DC-DC converters, either the state space averaging approach or the averaged switch modelling approach can be adopted [69-72] to model the dynamic behaviour and allow the closed loop control design to be done. However, due to the oscillation of the state variables such as the resonant inductor current and resonant capacitor voltage, the state space averaging and the averaged switch modelling approaches cannot be applied directly to the resonant converters [71]. There are several methods to model resonant converters such as sampled data modelling, State Plane analysis and the direct-quadrature DQ modelling technique. Sampled data modelling can be used to obtain the large signal response of a resonant converter; however, it suffers from long computation time [73]. State plane analysis is only a valid approach to second order resonant converters [74].

The DQ modelling approach, which was introduced in [18], requires less computational effort and has a simpler mathematical derivation to model resonant converters. The authors in [3, 56] demonstrated that the DQ modelling technique can represent the resonant converter dynamics and steady state behaviour accurately and have developed the DQ modelling technique for the three-phase SRPL resonant converter.

In this chapter the DQ method is used to model the proposed single-phase SRSL resonant converter in order to represent the resonant converter dynamics and steady state behaviour. Thus, the system transfer function can be obtained, which is utilised in the closed loop control design. The converter transfer function is used to design a suitable PI controller with the aim of achieving both

the dynamic and steady state requirements for the output current regulation. In order to implement the controller digitally using an FPGA/DSP control platform, the control design procedure is carried out directly in the discrete time domain. In addition, in order to examine the proposed converter topology and associated control strategy and to avoid unnecessary cost and the production of high voltage; an emulator prototype is also proposed and developed to represent the magnetron load behaviour in a laboratory environment. Moreover, simulation results are provided in this chapter to demonstrate the effectiveness of the proposed method.

6.2 DQ Modelling Technique

The DQ modelling technique is used to derive a suitable plant which can be used for control design activities [18]. In the considered application the DQ modelling technique is used to derive the relationship between the converter output current and the tank input voltage. The assumptions of the DQ model are:

- The tank current is sinusoidal.
- The input voltage (DC link) constant and has no ripple.
- All converter components are ideal (lossless).
- All capacitors and inductors are time-invariant.

The input DC link and the H-Bridge, which is shown in Figure 5.1, can be treated as a controlled voltage sourced inverter (*VSI*); hence the simplified equivalent circuit of the SRSL converter is shown in Figure 6.1. Here V_S represents the square wave voltage from the *VSI*, i_t is the tank current, L and C are the resonant inductor and capacitor, v_o is the output voltage of the resonant tank, C_f is the filter capacitor, V_o is the output voltage and I_{out} is the output current.
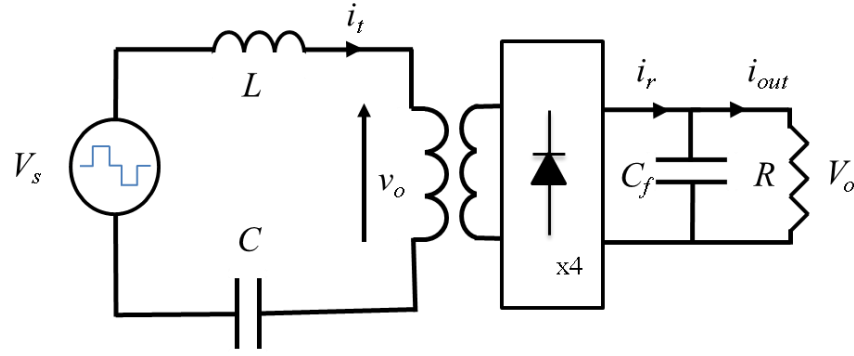
Figure 6.1 equivalent circuit of the SRSL DC-DC converter

By considering only the fundamental component, the input voltage V_s can be written as (6.1).

$$V_s = \hat{V}_s \cos(\omega t) \tag{6.1}$$

The tank current i_t has the general form shown in (6.2).

$$i_t = \hat{i}_t \cos(\omega t - \varphi) \tag{6.2}$$

Where, $\hat{V}_s$ is the peak amplitude of the fundamental component, ω is the fundamental frequency, $\hat{i}_t$ is the peak amplitude of the resonant inductor current and φ is the phase shift of the resonant circuit impedance. By assuming V_o is ripple free, changing slowly compared to the resonant circuit and taking only the fundamental component as Q is considered high ($Q \geq 2.5$) [3], the voltage v_o that is applied to the high frequency transformer (*HF*) can be represented as (6.3).

$$v_o = \frac{4}{(n\pi)} V_o \cos(\omega t - \varphi) \tag{6.3}$$

While the mean value of the output current I_{out} is written as (6.4).Where, n, in equation (6.3) is the *HF* transformer turns ratio.

$$I_{out} = \overline{i}_r = \frac{2}{(\pi * n)} \hat{i}_t \tag{6.4}$$

The equivalent circuit in figure 6.1 is still a complex circuit. In order to express this circuit in DQ form, the high frequency term is removed by converting the system of figure 6.1 into a two-phase equivalent circuit, similar to the method

used for three phase machine analysis, by introducing $\alpha - \beta$ axis system by using $\cos(\omega t)$ and $\sin(\omega t)$ functions [18]. Unlike the three-phase system, the orthogonal counterpart β circuit is generated mathematically. Then, this $\alpha - \beta$ axis system is further converted into the DQ frame as described below. Figure 6.2 shows the vector diagram of $\alpha - \beta$ axis. Where, f , here is the peak fundamental component and can be either voltage or current.
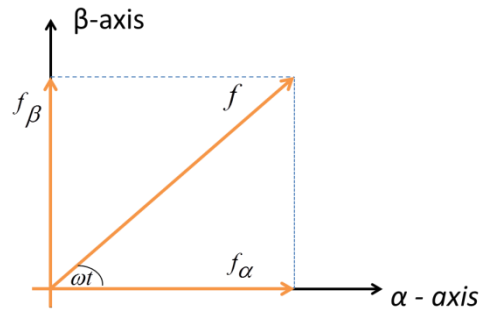
Figure 6.2 the vector diagram of the $\alpha - \beta$ axis

From this figure the α and β component functions can be expressed as

$$f_\alpha = f.\cos \omega t \tag{6.5}$$

$$f_\beta = f.\sin \omega t \tag{6.6}$$

Based on these equations equivalent circuit of the SRSL DC-DC converter can be converted into two phases as shown in Figure 6.3
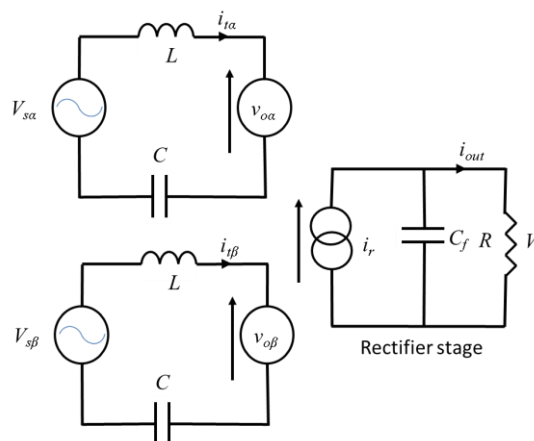
Figure 6.3 the two phase $\alpha - \beta$ equivalent circuit

Where the parameters $(V_s , v_o , i_t$ and $\bar{i}_r)$ can be defined as:

$$V_{s\alpha} = V_s \cos(\omega t) \tag{6.7}$$

$$V_{s\beta} = V_s \sin(\omega t) \tag{6.8}$$

$$i_{t\alpha} = i_t \cos(\omega t - \varphi) \tag{6.9}$$

$$i_{t\beta} = i_t \sin(\omega t - \varphi) \tag{6.10}$$

$$v_{o\alpha} = \frac{4}{(\pi * n)} V_{o\alpha} \cos(\omega t - \varphi) \tag{6.11}$$

$$v_{o\beta} = \frac{4}{(\pi * n)} V_{o\beta} \sin(\omega t - \varphi) \tag{6.12}$$

$$\bar{i}_r = \frac{2}{(\pi * n)} \sqrt{i_{t\alpha}^2 + i_{t\beta}^2} \tag{6.13}$$

It can be seen that the two phase $\alpha - \beta$ equivalent circuit still has *AC* quantities which are difficult to deal with for control due to the vector rotation. In order to simplify that, the two phase $\alpha - \beta$ equivalent circuit need to be transferred into DQ axis [3].
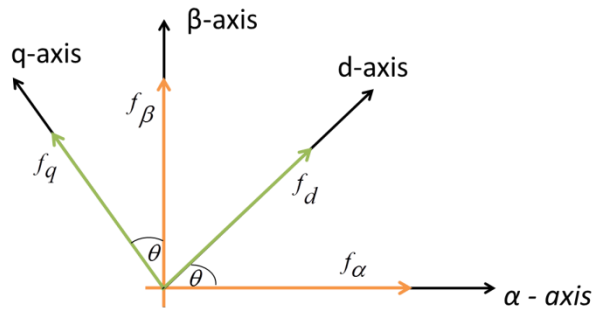
Figure 6.4 the vector diagram of the $\alpha - \beta$ projecting in DQ axis

Based on the vector diagram shown in Figure (6.4), the transformation to the DQ model is defined by the following equations where for simplicity θ is chosen to be equal to ωt.

$$f_{dq} = (f_d - f_q \cdot \text{j}) \tag{6.14}$$

$$f_{dq} = f_{\alpha\beta} e^{-j\theta} \tag{6.15}$$

$$f_{\alpha\beta} = f_{dq} e^{j\theta} \tag{6.16}$$

These equations can be used to derive the DQ equivalent circuit of the proposed converter. The derivation procedures are detailed in Appendix C. Figure 6.5 shows the DQ model equivalent circuit for the SRSL DC-DC converter.
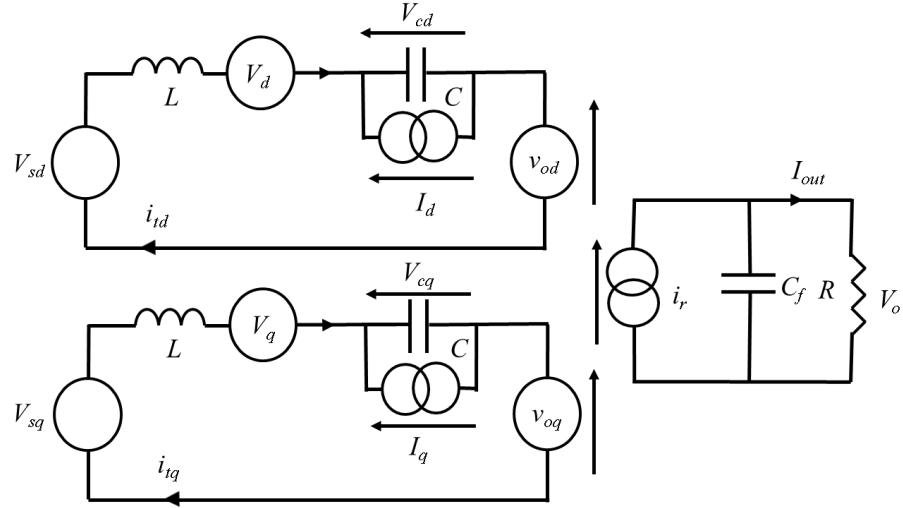
Figure 6.5 DQ model equivalent circuit for the SRSL DC-DC converter

Where,

$$V_{sd} = V_s, \quad V_{sq} = 0 \tag{6.17}$$

$$V_d = Li_{tq}\omega, \quad V_q = -Li_{td}\omega \tag{6.18}$$

$$I_d = CV_{cq}\omega, \quad I_q = -CV_{cd}\omega \tag{6.19}$$

$$i_{td} = i_t \cos\varphi, \quad i_{tq} = i_t \sin\varphi \tag{6.20}$$

$$v_{od} = \frac{4}{\pi n} V_o \cos\varphi = \frac{4 V_o i_{td}}{\pi n \sqrt{i_{td}^2 + i_{tq}^2}} \tag{6.21}$$

$$v_{oq} = \frac{4}{\pi n} V_o\, i \sin\varphi = \frac{4 V_{oi} i_{tq}}{\pi n \sqrt{i_{td}^2 + i_{tq}^2}} \tag{6.22}$$

6.3 State Space Equation Model

In order to simplify the *DQ* circuit further, the output stage (output filter and load) is referred to the input side by scaling all voltage on the output side by $\frac{4}{\pi n}$, all output currents by $\frac{\pi n}{2}$ and all impedances in the output stage in figure 6.5 by *K*, where $k = \frac{8}{\pi^2 n^2}$.
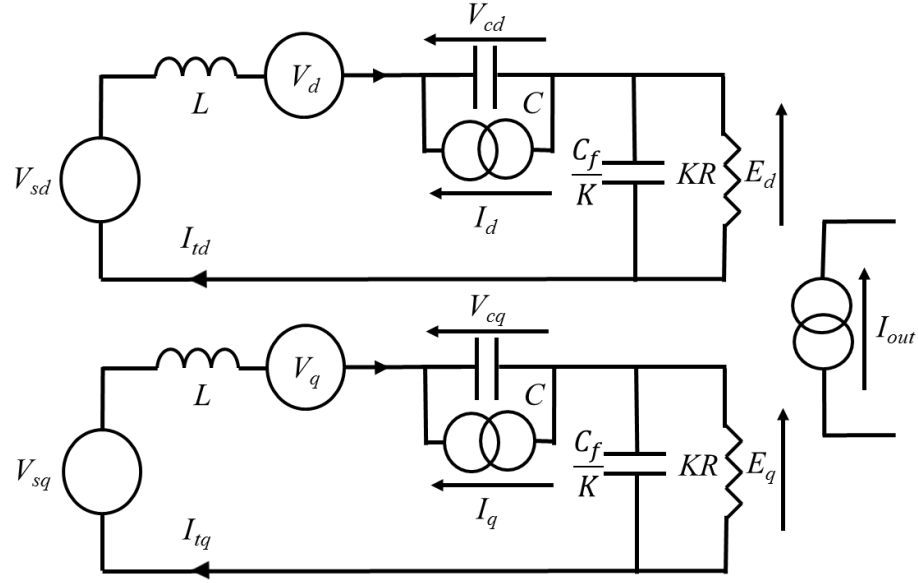
Figure 6.6 equivalent DQ model circuit, the output stage referred to the input

Based on the equivalent circuit shown in Figure 6.6, a set of differential equations which describing the converter system dynamic are obtained. The system has six state variables (I_d, I_q, V_d, V_q, E_d, E_q), hence the state space equations can be written as:

$$\frac{dI_d}{dt} = \frac{V_{sd}}{L} - \frac{V_{cd}}{L} - \omega i_{tq} - \frac{E_d}{L} \tag{6.23}$$

$$\frac{dI_q}{dt} = -\frac{V_{cq}}{L} + \omega i_{td} - \frac{E_q}{L} \tag{6.24}$$

$$\frac{dV_d}{dt} = \frac{i_{td}}{c} - \omega V_q \tag{6.25}$$

$$\frac{dV_q}{dt} = \frac{i_{tq}}{c} + \omega V_d \tag{6.26}$$

$$\frac{dE_d}{dt} = \frac{ki_{td}}{c_f} - \frac{E_d}{Rc_f} \tag{6.27}$$

$$\frac{dE_q}{dt} = \frac{ki_{tq}}{c_f} - \frac{E_q}{Rc_f} \tag{6.28}$$

The expression of the output current I_{out} associated with the DQ model circuit can be determined as

$$I_{out} = \frac{2}{n*\pi} \sqrt{\left(\frac{E_d}{KR}\right)^2 + \left(\frac{E_q}{KR}\right)^2} \tag{6.29}$$

By setting the input voltage to the DQ model circuit (V_{sd}) equal to u, the output current I_{out} equal to y and denoting (I_d, I_q, V_d, V_q, E_d and E_q) as $x_1 - x_6$ respectively, the state space equations can be written in the general form as (6.30).

$$\frac{dx}{dt} = Ax + Bu$$
$$y = Cx + Du$$

(6.30)

The equation (6.29) shows the relation between the output current I_{out} and the two state variables E_d and E_q. It can be noticed that this equation is nonlinear. It is necessary to linearise I_{out} at the nominal steady state operating point before applying the feedback control design. The linearisation technique used for equation (6.29) is presented as follows. Letting the output current $I_{out} = y$, $E_d = x_5$ and $E_q = x_6$ the equation (6.29) can be written as

$$y = \frac{2}{n\pi KR} \sqrt{(x_5)^2 + (x_6)^2}$$

(6.31)

Taking the partial derivative of (6.31) hence

$$\partial y = \frac{2}{n\pi KR \sqrt{(x_5)^2 + (x_6)^2}} \left((x_5 \partial x_5) + (x_6 \partial x_6) \right)$$

(6.32)

For a steady operating point, by solving x_5 and x_6, equation (6.32) represents the linear form of equation (6.31). The output current feedback control is designed based on the above equations. The state space matrices [A, B, C, D] were presented as follows:

$$A = \begin{bmatrix} 0 & -\omega & -\frac{1}{L} & 0 & -\frac{1}{L} & 0 \\ \omega & 0 & 0 & -\frac{1}{L} & 0 & -\frac{1}{L} \\ \frac{1}{C} & 0 & 0 & -\omega & 0 & 0 \\ 0 & \frac{1}{C} & \omega & 0 & 0 & 0 \\ \frac{K}{C_f} & 0 & 0 & 0 & -\frac{1}{RC_f} & 0 \\ 0 & \frac{K}{C_f} & 0 & 0 & 0 & -\frac{1}{RC_f} \end{bmatrix}$$

(6.33)

$$B = \begin{bmatrix} \dfrac{1}{L_r} \\ 0 \\ 0 \\ 0 \\ 0 \\ 0 \end{bmatrix} \tag{6.34}$$

$$C = \begin{bmatrix} 0 & 0 & 0 & 0 & \Gamma_1 & \Gamma_2 \end{bmatrix} \tag{6.35}$$

$$D = \begin{bmatrix} 0 \end{bmatrix} \tag{6.36}$$

Where, the parameters Γ_1 and Γ_2 in matrix C are the linearized model.

$$\Gamma_1 = \frac{2}{n\pi KR \sqrt{(x_5)^2 + (x_6)^2}} (x_5) \tag{6.37}$$

$$\Gamma_2 = \frac{2}{n\pi KR \sqrt{(x_5)^2 + (x_6)^2}} (x_6) \tag{6.38}$$

Substituting ((6.37), (6.38)) into (6.35) and using the converter state variables E_d and E_q the matrix C can be re-written as

$$C = \begin{bmatrix} 0 & 0 & 0 & 0 & \left(\dfrac{2(E_d)}{n\pi KR \sqrt{(E_d)^2 + (E_q)^2}} \right) & \left(\dfrac{2(E_q)}{n\pi KR \sqrt{(E_d)^2 + (E_q)^2}} \right) \end{bmatrix} \tag{6.39}$$

6.4 System Transfer Function

The previous section illustrated the way of deriving the space representation of the DQ model in order to obtain the transfer function. This can be achieved by taking Laplace transform of the state space equations in (6.30) and assuming zero initial conditions [75, 76]. The new state-space representation can be written as

$$\begin{aligned} s.x(s) &= A.x(s) + B.u(s) \\ y(s) &= C.x(s) + D.u(s) \end{aligned} \tag{6.40}$$

The transfer function $\dfrac{y(s)}{u(s)}$ can be derived as

$$\frac{y(s)}{u(s)} = C(s.I - A)^{-1}.B + D \tag{6.41}$$

Where, I is the identity matrix. Using the following MATLAB commands make it easy to calculate the system output current transfer function $\dfrac{y(s)}{u(s)}$ where in this case $\dfrac{y(s)}{u(s)} = \dfrac{I_{out}(s)}{V_{sd}(s)}$.

$$
\begin{aligned}
[E,\ F]\ &=\ ss2tf\ (A,\ B,\ C,\ D);\\
Plant\_s\ &=\ tf\ ([E],\ [F]);
\end{aligned}
\tag{6.42}
$$

Where, E and F are the numerator and denominator of the transfer function, respectively.

6.5 Model Validation

In order to validate the DQ modelling method for the proposed converter a three *PLECS* models have been developed based on the parameters in table 4.1 when $Q=5$ and M=0.8. These models are: the actual resonant converter model as figure 6.1, the developed DQ model as figure 6.6 and the state space matrices model as ((6.33),(6.34),(6.35),(6.36)). The simulation applies open loop control with step change in the input voltage (i.e. the *DC* link voltage changes from 561V to 700V at 0.007s). This condition is chosen simply to validate the model under the transient conditions. The transient in figure 6.7 clearly shows consistency in accuracy of the modelling.
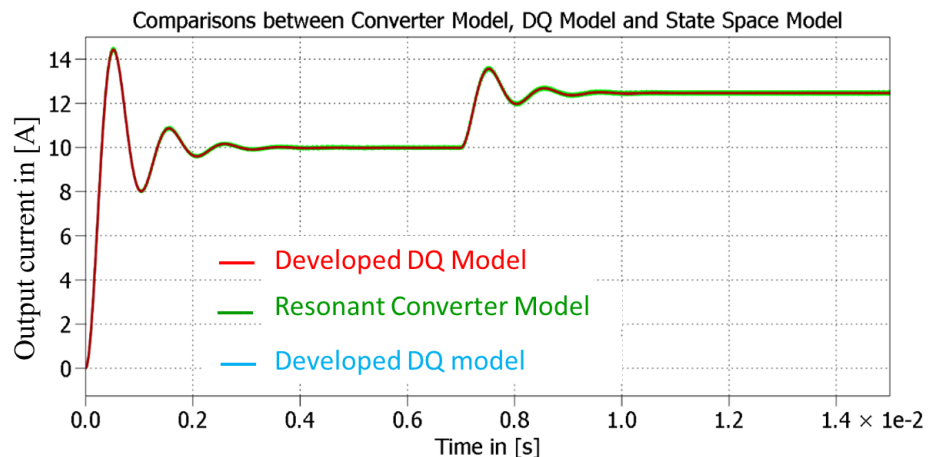
Figure 6.7 converter model, DQ model and state space model comparison

It should be mentioned that variation in frequency will result in inaccuracy in the final model as this has been linearised at a fixed frequency. Since the variable Q based CFPM control is used this means that relatively small deviations in

frequency are required when compared to frequency control and the error is small.

6.6 Closed Loop Current Control

In the previous sections, the state space equations were formulated and the converter transfer function was derived based on the DQ equivalent circuit for the SRSL converter. The converter transfer function is now used to design a suitable *PI* controller with the aim of achieving both the dynamic and steady state requirements for output current regulation. In order to implement the controller digitally using a FPGA/DSP control platform, all the control design procedures are carried out directly in the discrete time domain.

In order to control the output current of the convertor, a *PI* controller has been designed. In conjunction with the given power supply specification (Table 4.1) and the transfer function (from DQ modelling), the SISO toolbox in Matlab was used to obtain the *PI* controller parameters. A schematic diagram of the current control loop is shown in figure 6.8 where limits of the modulation index, M, are not included and the system is assumed to have linear characteristics. For a given output current target value, the *PI* controller output will determine target values for the converter voltage V_{AB}; the modulation index M can be calculated according to (6.43), where V_{DC} is the instantaneous DC link voltage. The equivalent ac output load resistance R_{eq} is evaluated using load voltage and current measurements. Thus, an accurate load quality factor Q can be derived as shown in (6.44).

$$M = \frac{V_{AB} * \pi}{4 * V_{DC}} \tag{6.43}$$

$$Q = (\frac{\omega_o L}{0.9 v_o})(\frac{n\pi I_{out}}{2}) \tag{6.44}$$

Where, ω_o is the resonant frequency and L is the tank inductance. The frequency ratio F and the required switching frequency f can be obtained from (5.14). Furthermore, the corresponding phase shift that retains soft switching can be derived as in (5.16).
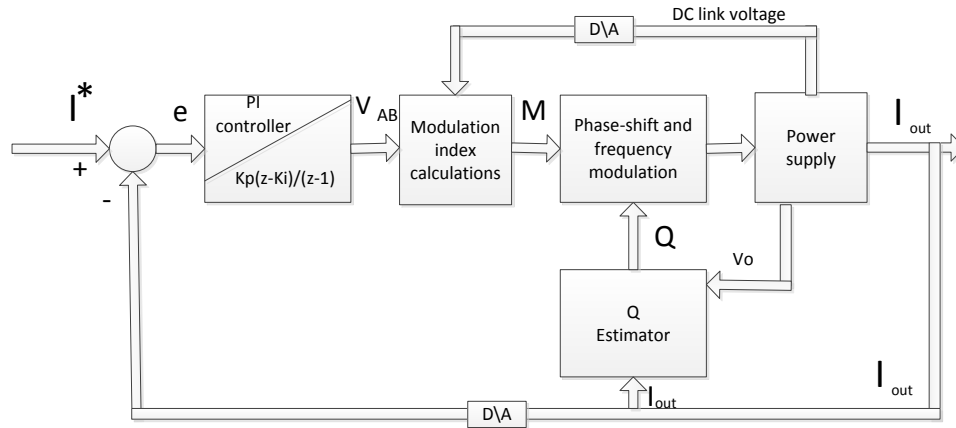
Figure 6.8 schematic diagram of the current control loop

6.6.1 Implementation of Feedback Control

The controller of the proposed resonant converter will be implemented by utilising a DSP/FPGA platform. From equation (6.42) it can be seen that the system plant is expressed in the continuous *s* domain. It has to be discretised into the *z* domain in order to be implemented in the DSP/FPGA platform. Matlab provides a command which makes it easy to convert the continuous transfer function given in (6.42) into a discrete equivalent function with sampling period T_s [77].

$$Plant\_z = c2d(Plant\_s, \frac{1}{f_s}, \text{'zoh'}) \tag{6.45}$$

Where $f_s = \dfrac{1}{T_s}$ is the sample rate and *zoh* is the Zero-order hold (one of the design methods to obtain the discrete equivalent). It is clear that the transformation depends on the sample rate f_s where the sample rate is determined by the switching frequency. With a very high sample rate the samples may be distorted by the noise if the analogue to digital converter's (A/D) resolution is not sufficient. However, the calculation time of the variable *Q* based CFPM control is relatively high during each interrupt routine (this requires a relatively slow sample rate). A compromised sample rate value is chosen to be 40kHz based on the previous work done by PEMC group [56]. In order to represent the sampling delay time (DSP-FPGA calculation), a unity delay (1/Z) is applied. Based on equations (6.42), (6.45) and in conjunction with the given specification in Table 4.1 the discretised transfer function $G_p(z)$ is

$$plant = G_P(z) = \frac{0.0004918\ z^5 - 0.001411\ z^4 + 0.000947\ z^3 + 0.00077\ z^2 - 0.001197\ z + 0.000399}{z^6 - 4.954\ z^5 + 10.57\ z^4 - 12.47\ z^3 + 8.589\ z^2 - 3.286\ z + 0.548}$$

(6.46)

The SISO tool in MATLAB was used to design the PI controller according to the discrete plant transfer function. This PI controller was designed to ensure a smooth dynamic response and a wide stability margin as expressed in equation (6.47)

$$G_{PI}(z) = \frac{6.02\ (z - 0.65)}{(z - 1)}$$

(6.47)

Figure 6.9 shows the bode plot of the open loop control system. The gain margin and the phase margin were set to be 12.7dB and 86.8° respectively.
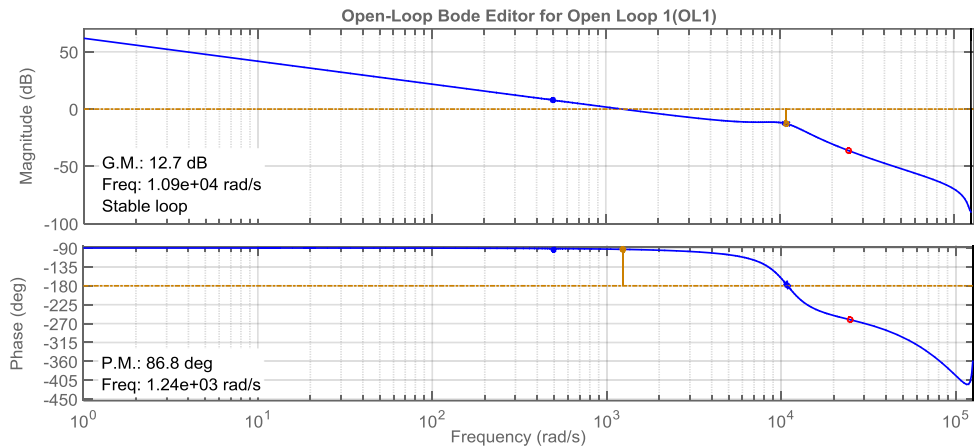
Figure 6.9 the bode plot of the open loop control system

The step response of the closed loop control system (G_{CLC}) is derived as in equation (6.48) and shown in figure 6.10.

$$G_{CLC}(z) = \frac{G_P(z)G_{PI}(z)}{1 + G_P(z)G_{PI}(z)}$$

(6.48)
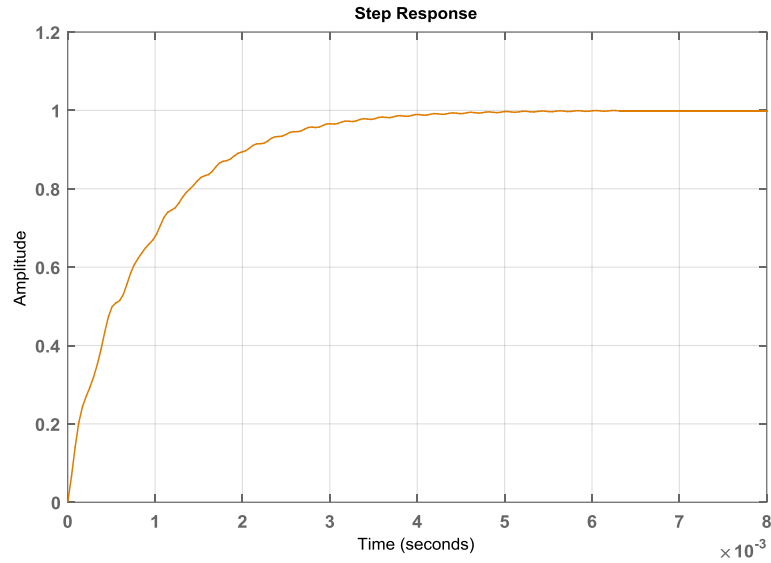
Figure 6.10 the step response of the closed loop control system

It can be noticed that no overshoot and oscillation occur at the transient and the output can trace the reference perfectly in steady state.

6.6.2 Gain scheduling

For the *DQ* modelling technique, a simplified linear model was considered. However, for nonlinear loads or variable load systems, different dynamic characteristics will be obtained as the load changes; therefore, a change in operating condition will lead to a different linearised model (Γ_1, Γ_2). In order to maintain a consistent dynamic response while the load is changing, a gain scheduling control has been introduced. The schematic diagram of the gain scheduling control loop is shown in figure 6.11, which is based on the same concept explained in section 6.6 However, in order to obtain the same dynamic characteristics, the values of the *PI* compensator parameters (K_p, K_i) need to be updated when the load varies.
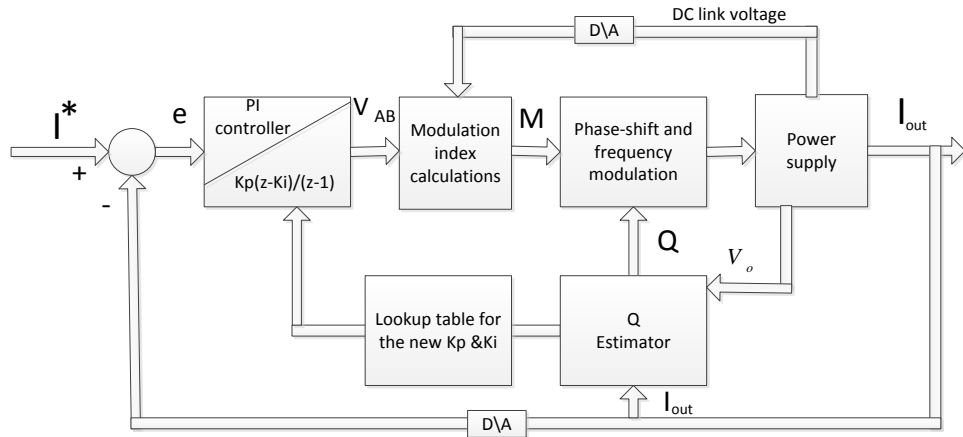
Figure 6.11 schematic diagram of the gain scheduling control loop

Equation (6.49) expresses the designed adaptive PI controller.

$$G_{PI} = \frac{K_P(z - K_i)}{(z - 1)}$$
(6.49)

K_p and K_i are updated for every new value of the Q. An off-line compensator lookup table is used to calculate the new parameters (K_i, K_p) when the load varies. The range of Q considered is from 3 to 5.

Figure 6.12 shows the step response of the system when the PI compensator is designed by assuming the load quality factor ($Q=5$), the step response of the system when the load changed to ($Q=3$) is also shown on the same figure.
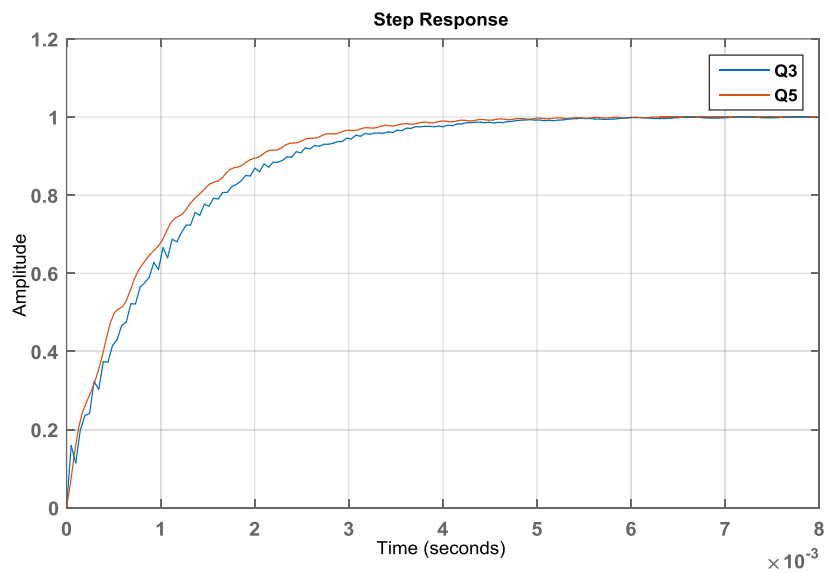
Figure 6.12 the step response of the system

Fig. 6.13 shows the step response of the system when the PI compensator is designed by considering the gain scheduling concept.
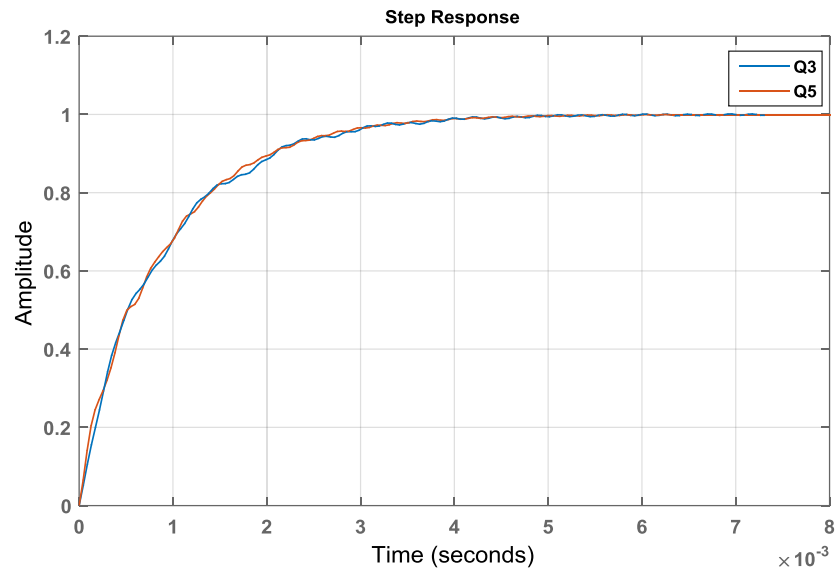
Figure 6.13 gain scheduling step response of the system

It can be seen from figure 6.12 that when the load quality factor varies from 5 to 3 the dynamic characteristics of the system in both cases ($Q=3$, $Q=5$) are different. However, when the gain scheduling concept is applied, the dynamic characteristics of the system in both cases ($Q=3$, $Q=5$) are nearly the same.

The idea of the gain scheduling control was investigated, however in this work this idea was not implemented as the converter was proposed to drive an industrial magnetron for a heating application (continuous wave) very fast response is not required.

6.6.3 Closed Loop Simulation Results

In this thesis the converter was designed to supply a magnetron where the close loop is required to regulate the output current. Using the given specifications in Table 4.1, the simulation set up of the SRSL converter with its current control loop is shown in figure 6.14. In this stage the load is represented as variable resistive load.
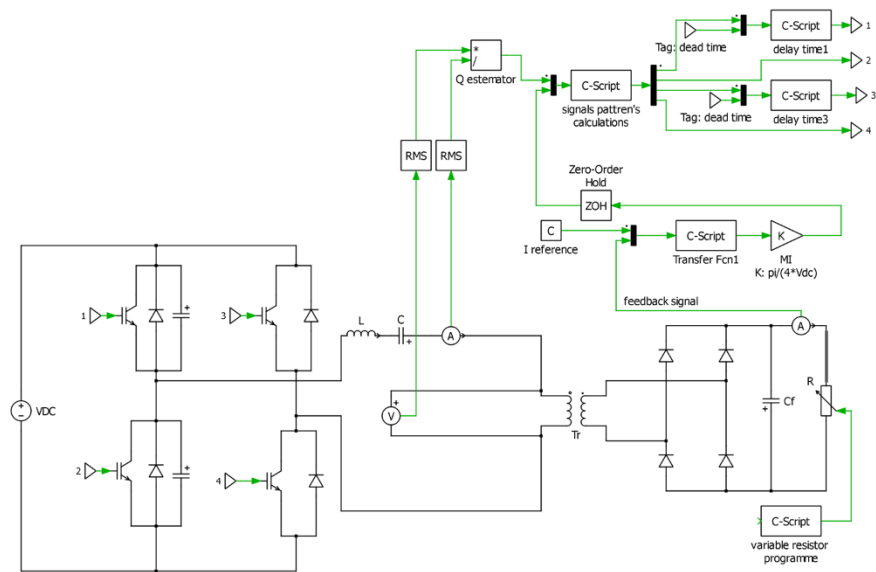
Figure 6.14 Simulation circuit set up for closed loop controller

In order to validate the proposed controller, the SRSL converter was simulated in closed loop control.

Figure 6.15 shows the simulation results for the output current and output voltage when the load quality factor *Q* ramps from *3 to 5*. The current reference in the controller was set at 6.5A. By using the variable resistive load and closed loop controller, the SRSL power converter will produce a constant output current with a variable *Q*.
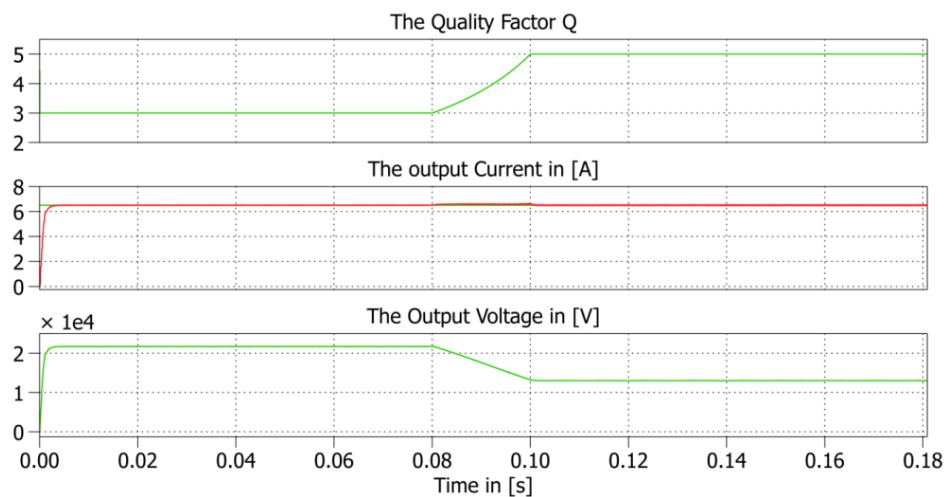
Figure 6.15 output current and voltage when *Q* ramps from 3 to 5

It can be seen that with the designed controller, the converter can regulate the output current well, while the output voltage varies when the resistive load is changed.

The output current can be regulated by changing the reference demand current, this is clear in figure 6.16 at 0.2s; the demand current changed from 7A to 8A.
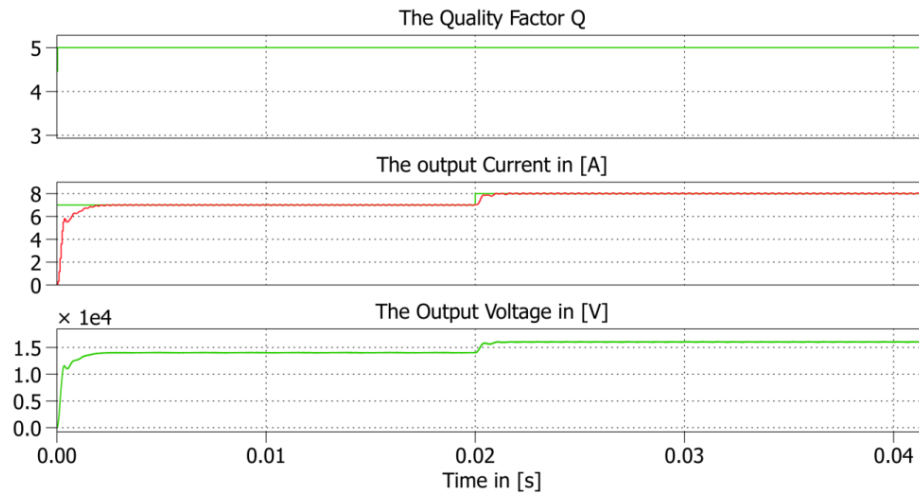
Figure 6.16 output current and voltage, demand current changed from 7A to8A

Clearly, the output current follows the demand signal which proves the current control design. Due to the resistive load utilised, the output voltage follows the change in the demand current to maintain constant Q. Although this does not represent the magnetron characteristics, using the resistive load in the simulation is still valid to examine the proposed control strategy to control the SRSL converter with variable load nature. A magnetron emulator will be simulated in the next section.

Figure 6.17 shows the closed loop resonant tank voltage and current when the load is changed from $Q=3$ to $Q=5$ at 0.08s.
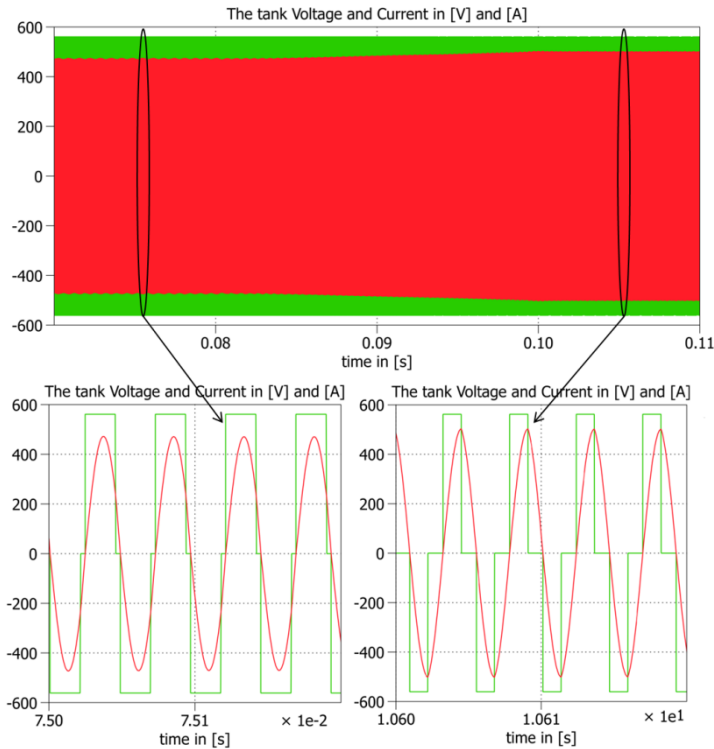
Figure 6.17 closed loop tank voltage and current, Q changes from 3 to 5

It is clear from figure 6.17 that with the use of the control method proposed both ZCS turn ON and OFF for the lagging leg are achieved despite the load being changed, allowing operation at high frequency with minimum losses.

Figure 6.18 shows the simulation results of the lagging leg turn OFF current (switching losses) when the load quality factor Q is changed from *3 to 5*.
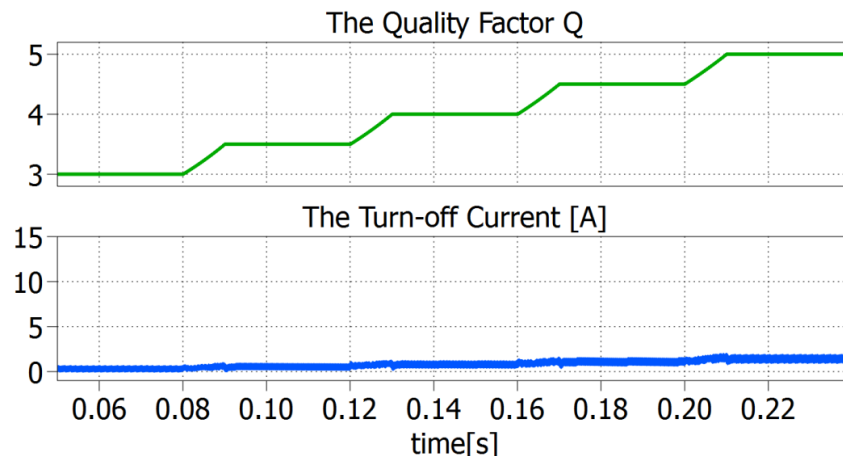
Figure 6.18 turn off current, load quality factor Q ramp changes from 3 to 5

It can be seen that at all the values of Q, the lagging leg turn OFF current has an insignificant value which is good indication that the lagging leg of the converter is soft switching. This proves that the proposed control strategy can achieve ZCS when the load is variable.

6.7 Magnetron Modelling and Emulator Approach

For an industrial magnetron, the quality of the produced radio frequency RF energy is a function of the anode current. Based on resonant technology, a series resonant series loaded (SRSL) power supply was proposed and designed previously to drive the magnetron. In order to examine the proposed converter topology and associated control strategy, and to avoid unnecessary cost and the production of high voltage; a reduced scale power electronics based magnetron emulator was also proposed and developed.

Based on magnetron characteristics shown figure (2.8) a typical relationship between the anode voltage and current is shown in figure 6.19. The increase in the anode voltage causes insignificant rise in the anode current until a critical voltage, knee voltage (V_{knee}) or cut-off voltage, is reached. After this knee voltage point the current is raised dramatically giving a dynamic slope resistance (R_{slope}). For the industrial magnetron to work, the applied anode voltage, V_a, must be greater than the knee voltage ($V_a > V_{knee}$). This nonlinear characteristic requires approximately a constant current power supply for stability.
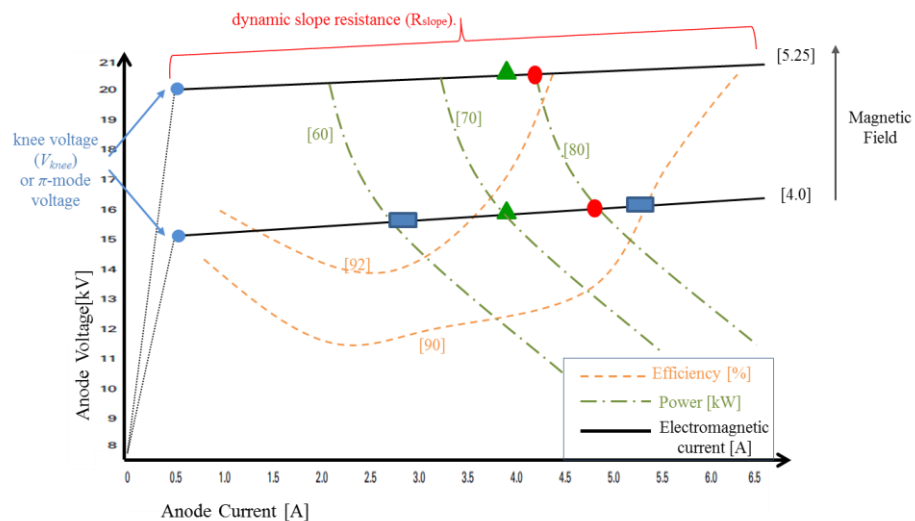
Figure 6.19 the relationship between the magnetron anode voltage and current

From figure 6.19 it can be noted that it is possible to adjust the knee voltage point by increasing the magnetic field. In order to vary the output power, either the knee voltage can be changed by varying the magnetic field applied to the tube as depicted in Figure 6.19 as green triangular points, or by varying the

current at a particular knee voltage as shown in Figure 6.19 as the blue rectangular points. A combination of the two can also be applied as illustrated in Figure 6.19 as red circular points. The latter combination could allow the magnetron to follow constant power characteristics and the possibility of higher RF efficiency illustrated by the efficiency contours.

The magnetron model is very important for the circuit design and simulations. From figure 6.19, the anode voltage and current characteristic can be modelled as a slope resistor and variable dc source corresponding to the knee voltage V_{knee} [23].

Figure 6.20 shows the simple model of the electrical equivalent circuit of the magnetron with these characteristics.
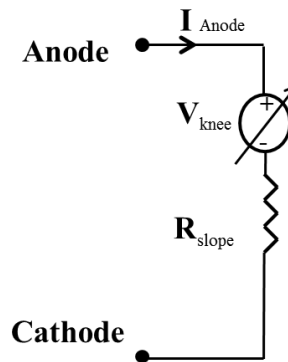
Figure 6.20 simple model of electrical equivalent circuit of the magnetron

The model comprises a slope resistor and variable dc source corresponding to the knee voltage V_{knee} [26]. The variable DC supply is set to certain values to represent the required knee voltage and emulate the magnetron characteristics. The challenge is how to implement this model practically without using a magnetron. The magnetron cannot be operated in a power electronic laboratory, a wave guide and dedicated RF loading equipment is required, and therefore the magnetron characteristics will be emulated by implementing a novel reduced scale power electronic prototype in order to validate the control method of the SRSL resonant power converter.

Two reduced scale power electronic prototypes were proposed in order to emulate the magnetron characteristics. The first one was a magnetron emulator using a Buck converter and the second one was the chopper based magnetron emulator, the latter was practically implemented in this work.

6.7.1 Magnetron Emulator Using a Buck Converter

The magnetron emulator system consists of a controlled voltage power supply to represent the knee voltage and the slope resistance R_{slope} as depicted in figure 6.21. The controlled voltage power supply comprises of a Buck converter and its voltage controller in order to set the output voltage at a particular knee voltage. The emulated knee voltage can be changed by varying the output voltage of the Buck converter. This will emulate the change in the magnetic field applied to the magnetron. Moreover, by fixing the output voltage of the Buck converter and controlling the tank current through the *SRSL* power converter control, a variable current at particular knee voltage can be obtained. This topology clearly can emulate the magnetron characteristics.
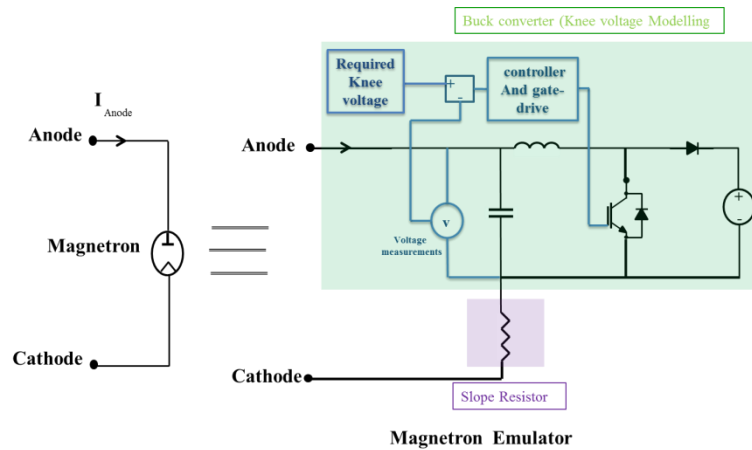
Figure 6.21 the Buck converter emulator scheme

6.7.2 Chopper Based Magnetron Emulator

This reduced scale power electronic prototype was proposed and developed in order to emulate the magnetron characteristics. Figure 6.22 show the chopper based magnetron emulator and its associated hysteresis controller.
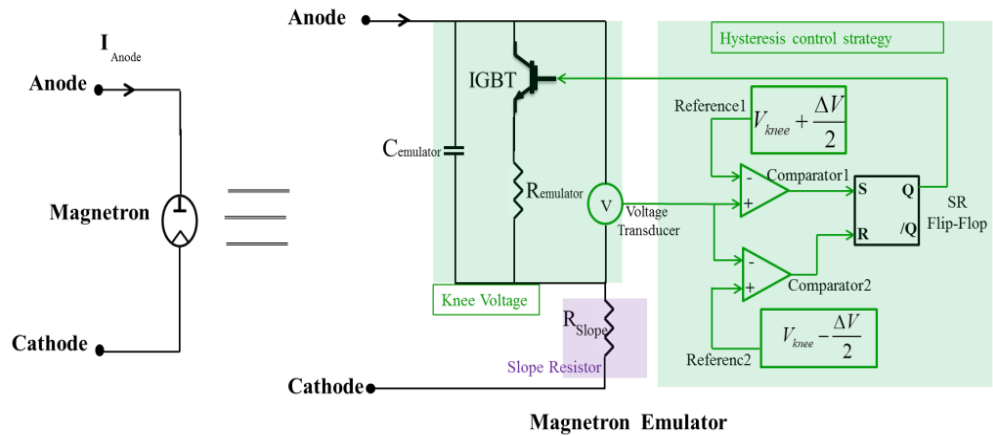
Figure 6.22 chopper based magnetron emulator

The knee voltage was simply represented by a resistor ($R_{emulator}$), capacitor ($C_{emulator}$) and IGBT switch. The slope resistance was represented by (R_{slope}). A hysteresis control was used to control the IGBT in order to obtain the required knee voltage. The hysteresis control comprises two comparators and an SR Flip-Flop logic circuit as depicted in figure 6.22. The anode current was regulated by using the SRSL converter controller.

This magnetron emulator has two modes of operation in order to set the knee voltage at the required (V_{Knee}) with a voltage ripple (ΔV). In mode 1 when the *IGBT* is *OFF* the main resonant converter charges the capacitor, $C_{emulator}$, until it reaches the value of reference *1* where the reference *1* is set as ($V_{knee} + \dfrac{\Delta V}{2}$).

At this point the hysteresis control will turn *ON* the IGBT and mode *2* starts. In mode *2* the *IGBT* is *ON* and the $C_{emulator}$ will be discharging until it reaches the value of reference *2* where the reference *2* is set as ($V_{knee} - \dfrac{\Delta V}{2}$), at this point the hysteresis control will turn off the *IGBT* and again back to mode *1*. This prototype can emulate the magnetron characteristics.

In contrast with the Buck converter emulator, the chopper based magnetron emulator approach requires less components and cost to be implemented. A reduced scale power electronic prototype based on this approach was developed and implemented in order to emulate the magnetron characteristics.

6.7.3 Magnetron Emulator Simulation Results

The proposed load emulator was used to emulate the changing characteristics of the magnetron when different levels of *RF* power are required where table 6.1 summaries the emulator parameters. Note in this simulation section, full scale magnetron emulator was used.

Table 6.1 the emulator parameters.

	Description	Symbol	Value
Design	Emulator capacitor	$C_{emulator}$	1 μF
Results	Emulator resistor	$R_{emulator}$	1700 ohm
	Slope resistor	R_{slope}	200 ohm

The simulation set up of the *SRSL* converter with the magnetron emulator is shown in figure 6.23.
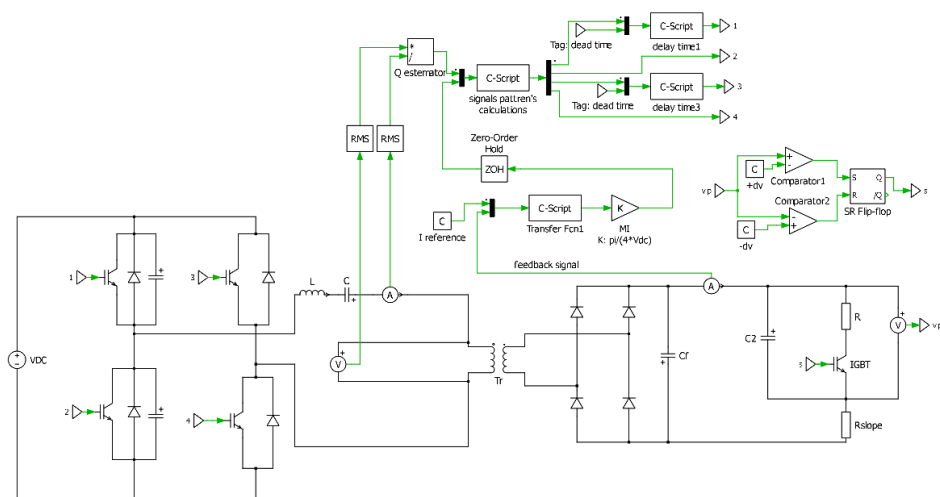
Figure 6.23 simulation circuit set up for the SRSL converter with the magnetron emulator

Figure 6.24 shows *PLECS* simulation results for the knee voltage when the hysteresis control is set to 16.850kV average knee voltage with a100V voltage ripple ($\Delta V = 100V$).
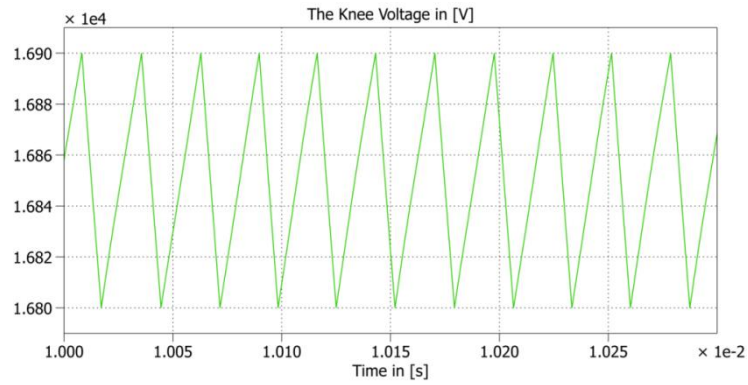
Figure 6.24 knee voltage simulation results

As expected, the hysteresis controller can regulate the knee voltage accurately at 16.85kV with $\Delta V = 100V$.

Figure 6.25 shows the simulation result for the knee voltage when the hysteresis control is set to change the knee voltage from 16.85kV to 15.85kV.
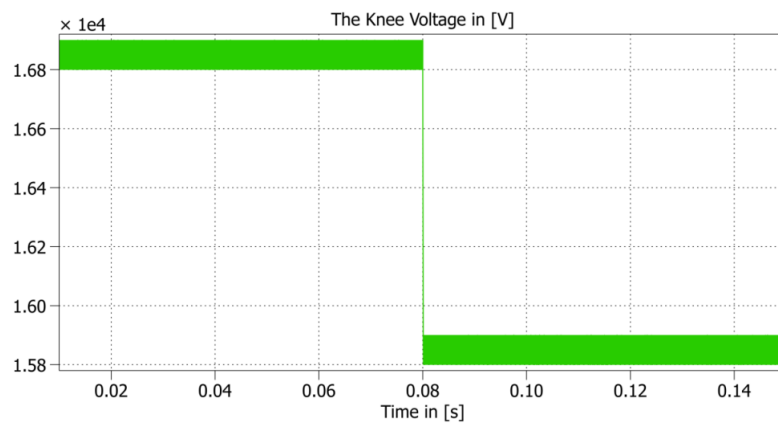
Figure 6.25 knee voltage f change from 16.85kV 15.85kV

It can be seen that the hysteresis controller successfully changes the knee voltage as required. This change will emulate the variation in the magnetic field applied to the tube in a real magnetron.

Figure 6.26 shows a step change of the output current reference from 4.5A to 6.5A (consequently the Q is step changed) in order to test the transient behaviour of the current controller and also to prove that the resonant converter control could drive a variable load.
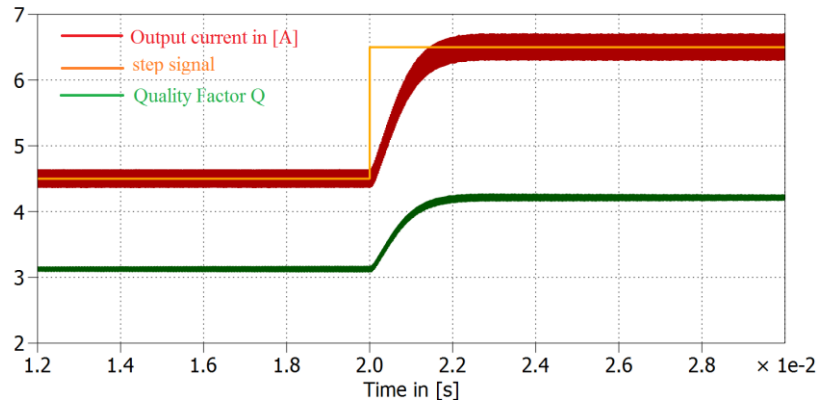
Figure 6.26 step change of the output current reference and corresponding Q

The change in the reference current will emulate the change in the anode current in the real magnetron. A combination of both the knee voltage and the reference current can be applied in order to find the most efficient *RF* generation point for a given load.

Figure 6.27 shows the simulation results of the current and the voltage waveforms of the resonant tank. In this case the output current demand is changed at 0.5s, while the hysteresis control is controlled to make the knee voltage constant. The IGBTs in the lagging leg are always switched at the zero crossing point of the tank current, while the ones in the leading leg have soft switching-on and hard switching-off. A snubber capacitor was utilized to achieve ZVS. Consequently, soft-switching can be obtained at full power in all the IGBTs.
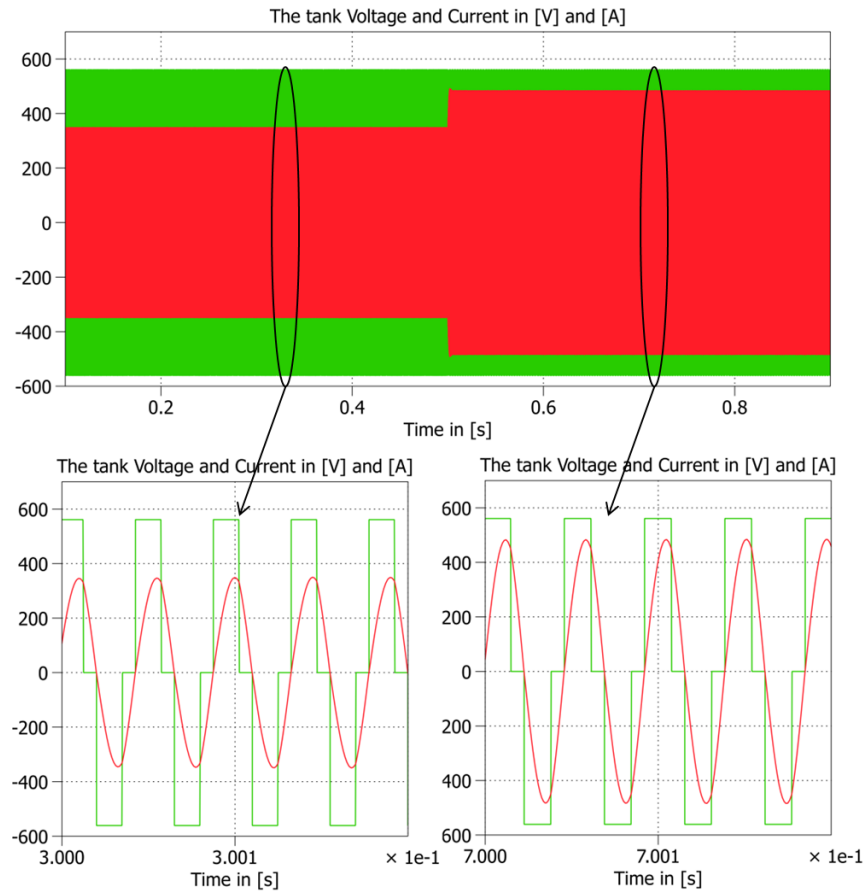
Figure 6.27 current and the voltage waveforms of the resonant tank

Figure 6.28 shows the output current, the knee voltage and the turn OFF current of the lagging leg at different values of Q. At 0.05s the hysteresis control demands the knee voltage to change from 12.85kV to 13.85kV. Consequently, the converter load changes and Q decreases from 4 to 3.5. The output current remains constant as the reference current demand is fixed at 6.3A.

At 0.13s the output current is demanded to be 5.5A and the output voltage is constant so Q decreased from 3.5 to 3.1. Also the figure shows another two changes at 0.1s and 0.17s. in all of these changes in the load quality factor either by the hysteresis controller to regulate the knee voltage or by the converter current controller to control the converter output current, the turn OFF current remains at almost zero. This proves that the lagging leg of the converter is switching at ZCS.
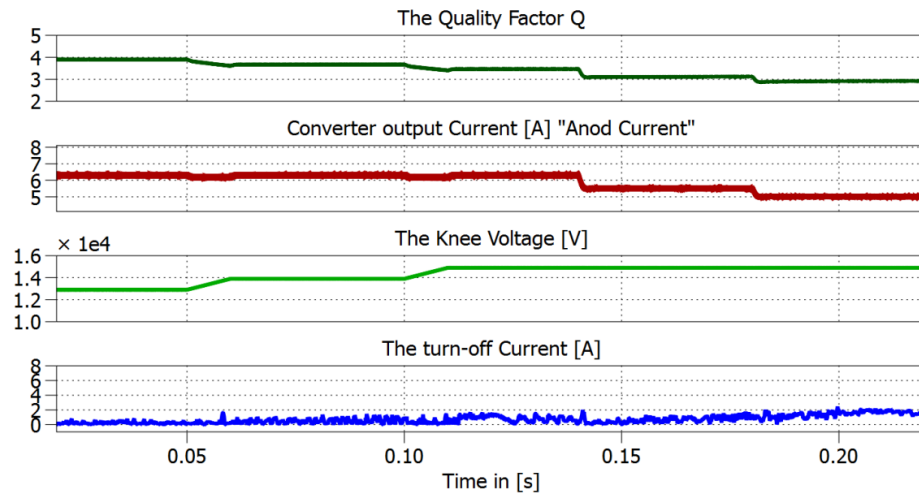
Figure 6.28 output current, knee voltage and turn off current at Q

This indicates that the proposed topology and its control methodology are appropriate to drive the industrial magnetron. Also, from the above figure it can be deduced that the soft switching is maintained during driving variable load nature.

Figure 6.29 shows a PLECS simulation of the I-V characteristics of the magnetron. An XY scope is used to draw the SRSL converter output current (representing the magnetron anode current) and the converter output voltage (representing the magnetron anode-cathode voltage).
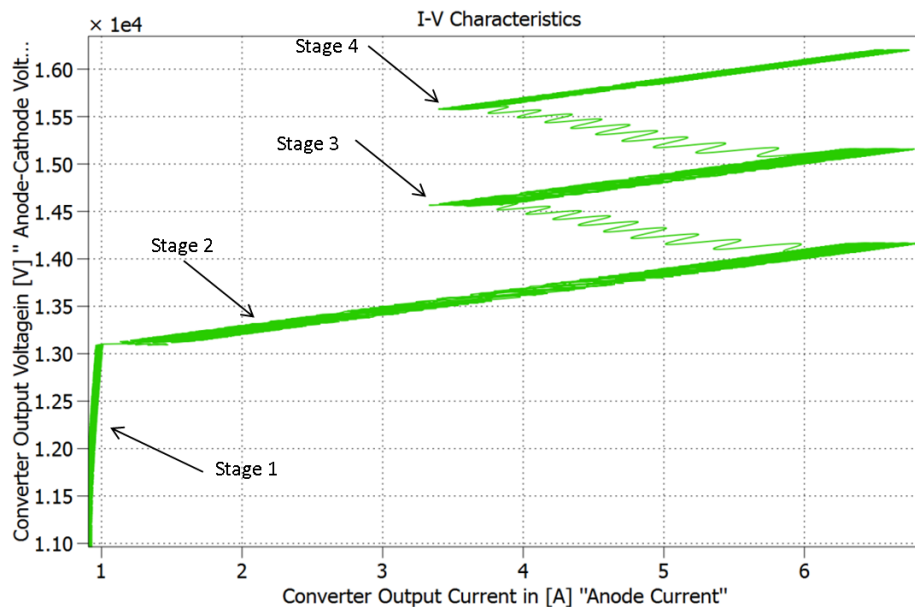
Figure 6.29 a PLECS simulation to the I-V characteristics of magnetron

From figure 6.29 it can be seen that Stage *1* represents the start-up, stage *2* represents the change in the current from 1 to 6.3A at slope voltage (13.05kV-

14.05kV), stage 3 shows the change in the knee voltage from 14.55kV to 15.05kV, stage 4 shows the change of the knee voltage to 15.55kV and finally in the last stage the current changed from 3.5A to 6.3A. These results illustrate that the variation in output load, either the knee voltage can be changed by varying the hysteresis controller (emulating the magnetic field applied to the tube) or by varying the current at a particular knee voltage (emulating Anode current applied to the tube). A combination of the two also can be applied to operate the magnetron with constant power characteristics and the possibility of higher RF efficiency.

6.8 Conclusion

In this chapter, a very brief review of the conventional modelling techniques for resonant converters has been given. Considering the advantages and disadvantages of various techniques, DQ modelling technique has been adopted to model the proposed SRSL resonant converter. By considering only the fundamental component and assuming sinusoidal tank current and a ripple free DC link, DQ model for the resonant converter was developed and a state-space representation was formulated.

Based on the DQ modelling, the system transfer function was obtained, which was utilised in closed loop control design. A *PI* current controller has been designed for the converter by using the *SISO* tool in *MATLAB* according to the discrete plant transfer function.

Two reduced scale power electronic prototypes were proposed in order avoid using magnetrons in the power electronic laboratory. The first one was the magnetron emulator using a Buck Converter and the second one was the Chopper Based Magnetron Emulator. The second prototype was adopted to be implemented as an industrial magnetron emulator.

PLECS simulation verification demonstrated the proposed converter and the magnetron emulator. It has been used to successfully validate the approach considered. With the use of the control method proposed the ZCS turn ON and turn OFF for the lagging leg were achieved despite the load was being changed, allowing operation at high frequency with minimum losses.

Chapter 7

CONVERTER HARDWARE DESIGN

7.1 Introduction

The feasibility of the novel variable Q based CFPM modulation technique and the closed loop control for the resonant converter will be verified using the prototype construction. It is noted in previous chapters that the rating of the proposed converter is 20kV, 100kW. In order to avoid unnecessary cost and complexity, a reduced scale prototype converter is considered for experimental validation. The practical design and construction of the prototype converter, which will be used to verify the feasibility of the converter topology and the control methodology is presented in this chapter.

7.2 The Converter Overview

Figure 7.1 shows an overview of the converter hardware. The converter prototype comprises a three phase rectifier, a DC link capacitor, an H-Bridge, a resonant tank, a transformer, a capacitive smoothing diode rectifier, the load and the control platform.
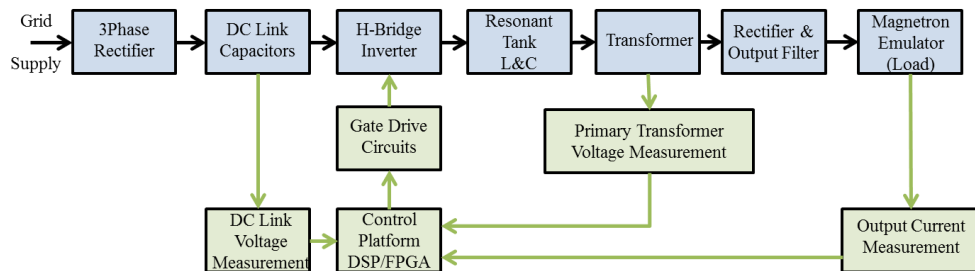
Figure 7.1 an overview of the converter hardware

Based on the power supply specifications and design illustrated in Table 7.1, the components of the power converter are designed and selected as detailed in the following sections.

7.3 The H-Bridge Design

7.3.1 H-Bridge and Gate Drive Design

The H-Bridge circuit and gate drive PCB board used in this project was designed by members of the PEMC group, University of Nottingham. The design has been modified for use in the proposed prototype. Moreover, snubber capacitors have been added to the H-Bridge. Figure 7.2 shows the diagram of the H-Bridge circuit board, which consists of fibre optic receivers, dead-time circuits, gate drive circuits and an IGBT module.
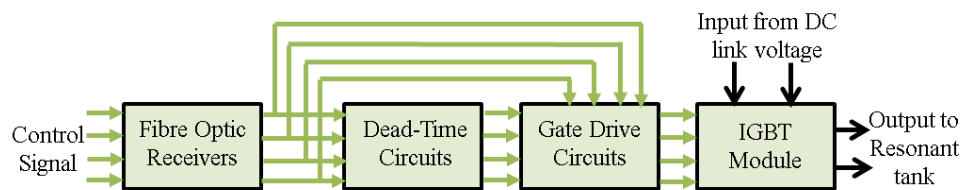
Figure 7.2 diagram of the H-bridge circuit board

A fibre optic line was used to transfer the control signals from the control hardware (FPGA, DSP) to the gate drive circuits. Figure 7.2 shows that the control signal received from the fibre optic cable can be transmitted to an analogue dead-time circuit or directly to the gate drive circuits. The main function of the dead-time circuits is to ensure that two IGBTs in each inverter leg are never turned ON at the same time, the absence of dead time circuits would cause a short circuit of the DC link capacitor. If the signal received from the fibre optic cable is transferred directly to the gate drive circuits, the dead-time required to avoid the short circuit can be programmed in the control board. The main advantages of using fibre optics are that this technology has good noise immunity and fast transmission.

7.3.1.1 H-Bridge Power Module

The H-Bridge module used in this circuit is *an Infineon - F430R06W1E3 - IGBT*, the collector-emitter voltage is 600V and the rated DC collector current is 30A. Figure 7.3 shows the H-Bridge power module which contains four IGBTs while Figure 7.4 shows a photograph of the H-Bridge board and the sunbber capacitors.
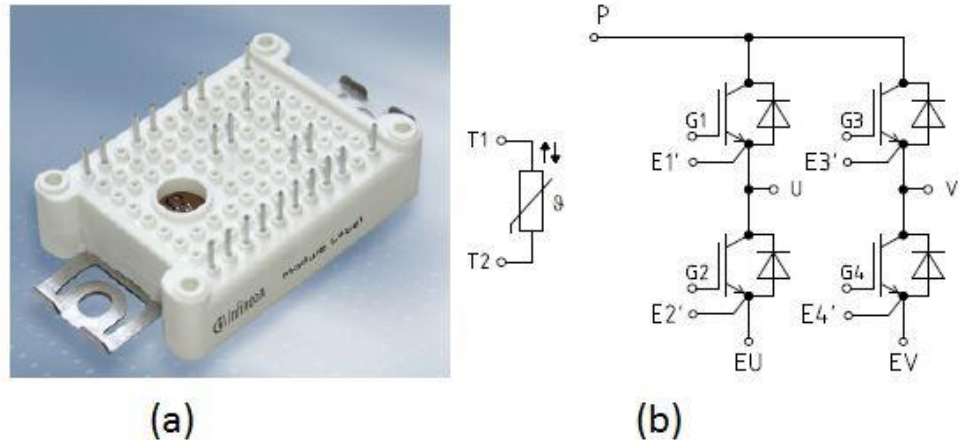
Figure 7.3 Infineon - F430R06W1E3: (a) power module (b) pin configuration
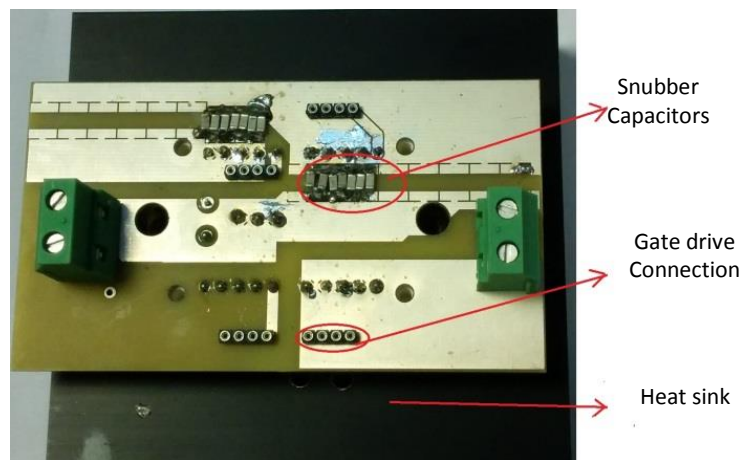
Figure 7.4 H-Bridge Board

7.3.1.2 Gate Drive Circuits

Figure 7.5 shows the gate drive circuits which contain a buffer, an *HCPL-3120* high speed Opto-coupler, a gate resistor (R_2), two Zener diodes and a gate-emitter resistor (R_3). In addition a R05P215D isolated 2W miniature DC-DC converter (+5V to ±15V) is utilised to supply the required voltages for the gate drive.
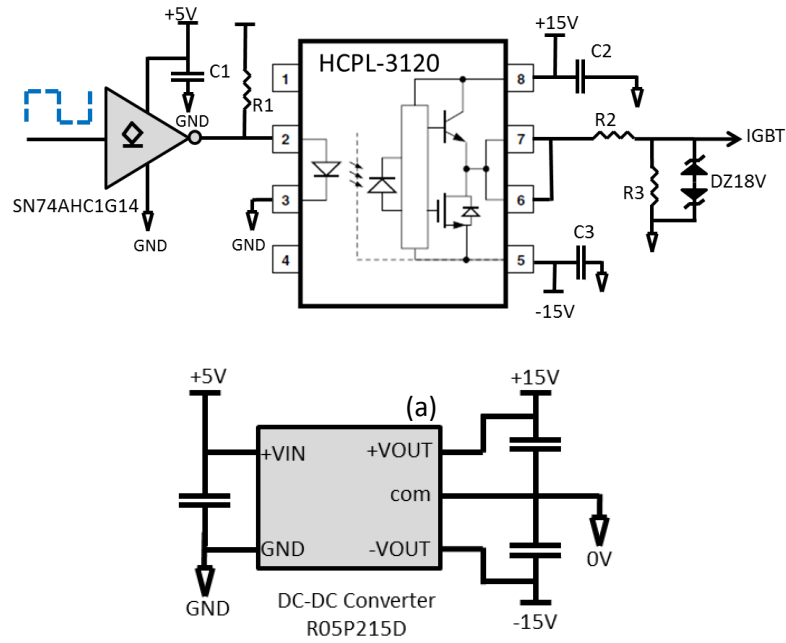
Figure 7.5 (a) the gate drive circuits (b) the DC-DC converter R05P2015D

The opto-coupler is used to provide electrical isolation between the control circuitry ground and the IGBT local ground. The current magnitude which will drive the gate of the *IGBT* is determined by the gate resistance (R_2). The two *18V* back-to-back Zener diodes are connected between the gate and emitter to protect the *IGBT* gate from over-voltages. A resistor (R_3) is connected between the gate and the emitter connections to prevent IGBTs turning ON via the parasitic capacitance in the event of control hardware failure. Figure 7.6 shows the gate drive circuit board.
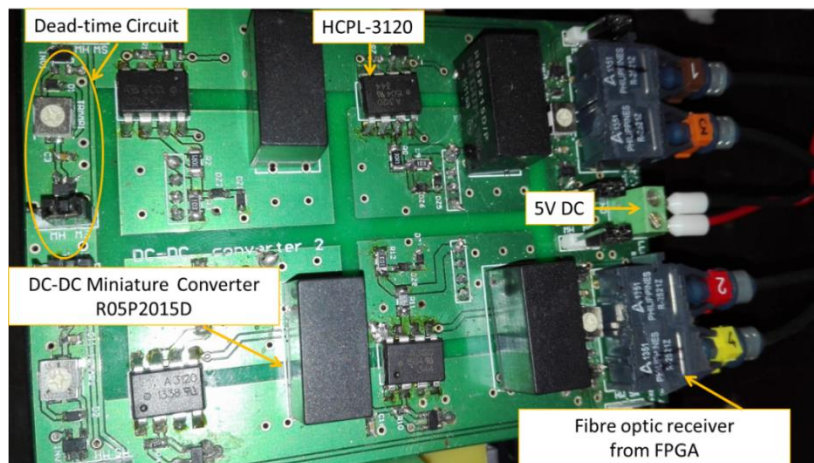
Figure 7.6 Gate Drive Board

Figure 7.7 shows the analogue dead-time circuit of one *IGBT*. The rising edge signal (*V_{PWM}*) is delayed for the required dead time by using an RC Circuit and a Schmitt inverter.
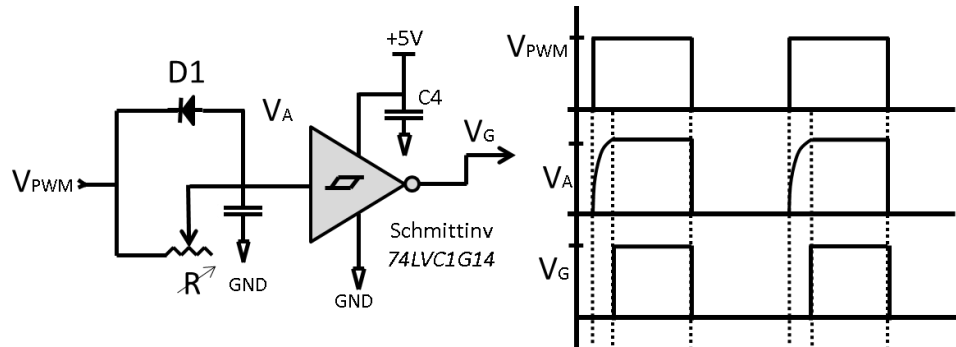
Figure 7.7 dead-time circuit of one IGBT

7.3.2 Snubber Capacitor and Dead Time Calculation

The snubber capacitor value and the dead time required are designed as following. In the case of the 3 kW prototype:

The maximum turn off current $I_{com}^{max} = 18A$ when (*Q=5*).

The minimum turn off current $I_{com}^{min} = 6A$ when (*Q=2*).

Based on data sheets of selected (*H-Bridge F4-30R06W1E3*,) the typical device current fall time is $t_f = 0.12\mu s$ and from the table 7.1 the DC link voltage is 400V. The snubber capacitor value was obtained as

$$C = \frac{18A * 0.12\mu s}{2 * 400V} \approx 2.7nF$$

Based on equations (5.26) and (5.27), the minimum dead time required between S_1 and S_2 was obtained as

$$T_D = \frac{2 \times 2.7nF \times 400V}{6A} \approx 0.36\mu s$$

7.4 The Control Platform and Measurements Design

7.4.1 Control Platform

Figure 7.8 shows a block diagram of the converter control hardware. This control hardware employs a digital signal processor (*DSP-TMS320C6713*), a HPI daughter card (*TMS320C6713 DSK HPI Daughter card*) and a field programmable gate array (*FPGA-Actel ProASIC3*) .The platform allows the system to perform different processes such as:

- Generation of switching signals for the power converter.

- Generation of a trip signals in the event of fault condition.

- Convert Analogue signal to digital signal.

- Calculations of control algorithm.
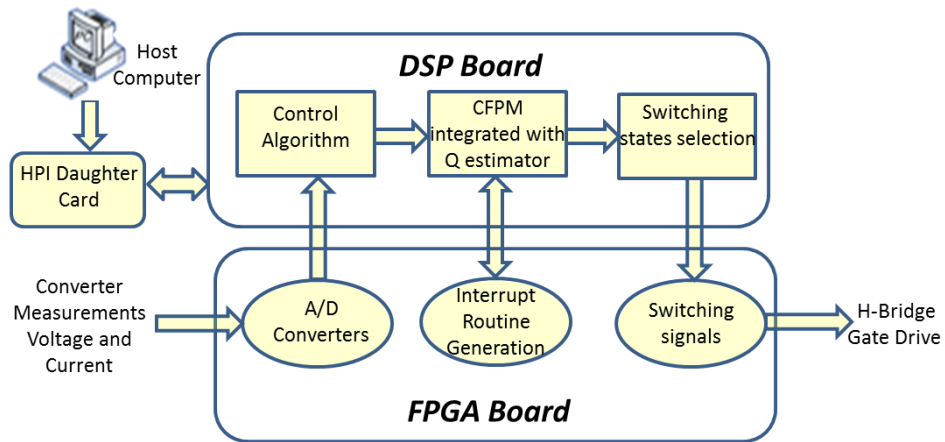
Figure 7.8 block diagram of the control platform for the converter

In this project this platform is utilised to control the series resonant power converter. The simple procedure is as follows: the FPGA hardware samples the signals from the transducers and saves them in memory. The DSP reads the digital signals in the memory obtained from the FPGA and uses this data as a part of the control strategies. When the *DSP* finishes the calculation process, the modulation demands are sent from the *DSP* to the *FPGA* and then to the gate drive circuit.

7.4.1.1 DSP-TMS320C6713

Figure 7.9 shows the C6713 DSK board. The main key features of this Kit are:

- DSP operating at 225 MHz

- A host Port Interface HPI (online reading and writing from a PC)

- 512KB of flash memory (a boot option)

- 32-bit External memory interface (EMIF)

Code Composer Studio software from Texas Instruments is utilised to programme the DSP using the C programing language. The HPI daughter card is employed to change variables in real time and to sample data via a host program.
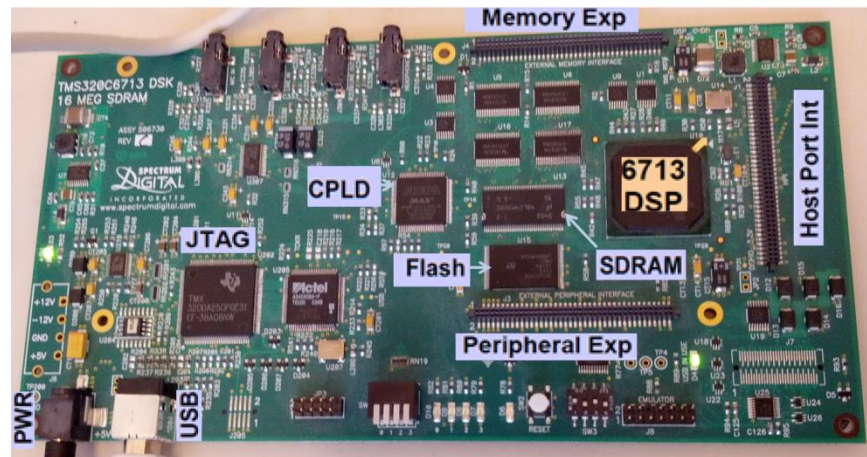
Figure 7.9 the C6713 DSK board

7.4.1.2 TMS320C6713 DSK HPI Daughter card

The HPI card is a high speed interface which allows a host PC to access the internal memory of the C6713 without interrupting the central processing unit of the DSP. This card can be used to transfer the data from/to the DSK board. The HPI daughter card is shown in figure 7.10. In this project the board is employed to load the control program into the DSK board via a USB connection. In addition, the HPI is utilised to modify the control strategy and to online view waveforms.
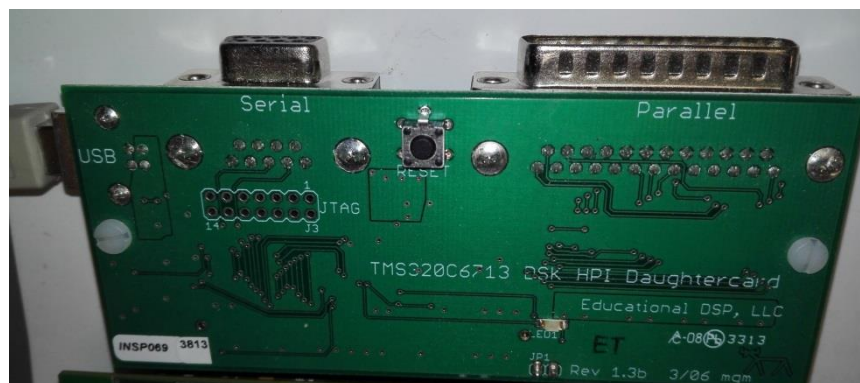
Figure 7.10 HPI card

7.4.1.3 FPGA-Actel ProASIC3

The FPGA card used was originally designed for the matrix converter by PEMC group at the University of Nottingham. Due to its flexibility it is adopted to be used for the control of the resonant converter. It is used to transmit the measured signals (V/A) from the transducers to the DSP where the control calculation is performed and after the DSP finishes the demands for the data of (F/ϕ) is transmitted to the FPGA and then to the H-Bridge gate drive through fibre optic

transmitters. The FPGA card shown in figure 7.11 is based on an ACTEL ProASIC3 A3P400 FPGA chip. The FPGA board operates with a 50MHz clock frequency and it has ten fibre optic outputs. It also has ten Analogue to Digital converter channels.
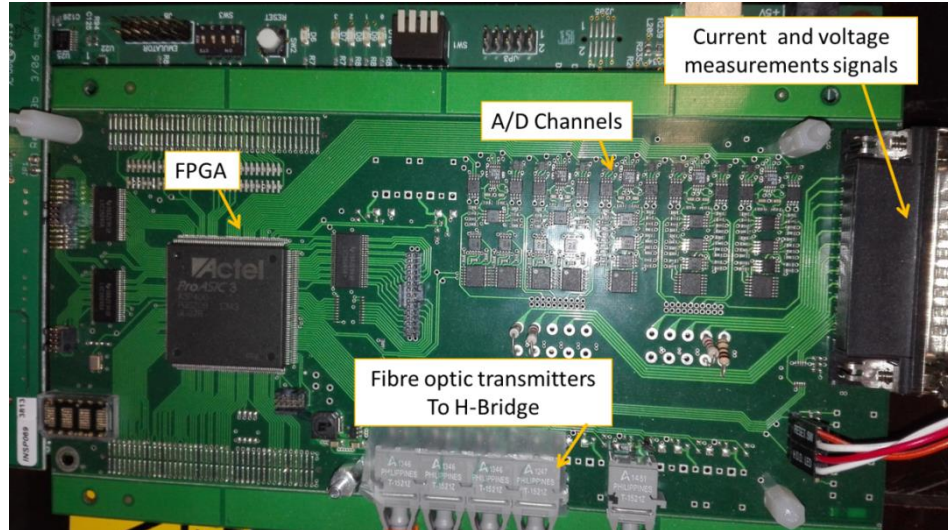
Figure 7.11 the FPGA card

The FPGA is connected through the External Memory Interface EMIF connectors of the DSK board which allows it to access the power supply, DSP memory, clocks and interrupts.

7.4.2 Control Software Implementation

The sampled data of (V_{DC}, I_{out} and V_o) is monitored by the DSP program during each sampling period. As discussed in section 5.5 the modulation index M is determined primarily by equation (5.11). Also, the Q of the resonant circuit is estimated by using equation 7.1. The first approach (discussed in section 5.4) is adopted to estimate the Q because in this reduced scale prototype there are no issues related with high voltage measurements.

$$Q = \frac{\omega L}{R} = \frac{\omega L}{(\frac{V_{out}}{I_{out}})} \tag{7.1}$$

Based on this, the phase shift between the two legs, ϕ and the normalised frequency ratio, F, can be obtained. Following this the gate drive demands can be generated as discussed in section 5.5 through amplitude reference and triangle wave.

The *FPGA* is used to generate the gate drive signals where the continuous triangle wave cannot be broken by the interrupting routine while the *DSP* is calculating the switching frequency and the phase shift. The phase shift and the amplitude reference can be identified from equation 5.42.

Providing the triangular wave generation and controlling the switching frequency can be achieved by stepping up the triangular frequency until it reaches 1 and stepping down to -1. This process is driven by a clock as shown in figure 7.12.
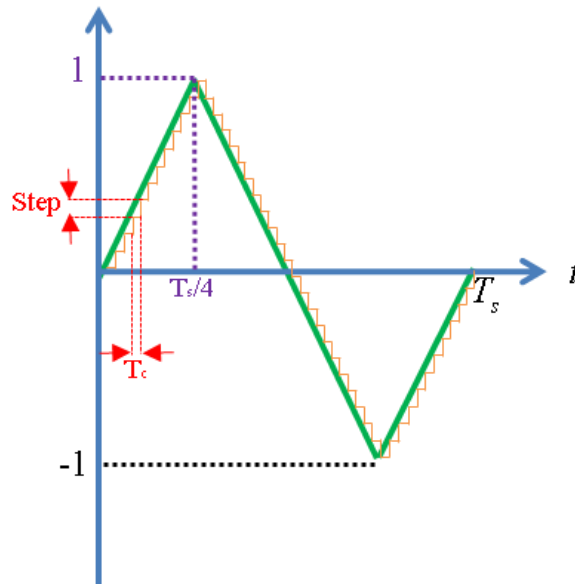
Figure 7.12 triangular wave generation.

It is clear from figure 7.12 that the higher the value of the step, the higher frequency of the triangular wave. The step value can be calculated from the following equation:

$$m = \frac{step}{T_c} = \frac{1}{(\frac{T_s}{4})}$$

(7.2)

Where *m* is the slope of the wave, the T_s is the switching period and the T_c is the clock period for triangular generation. The step should be as small as possible to increase the accuracy of the triangular wave. This indicates that the clock frequency should be very high and meanwhile to ensure the success of the process the clock cycle should be longer enough to calculate the triangular wave. In this work the clock frequency chosen for triangular wave generation is 10MHz. This is to ensure balance between wave accuracy and wave stability.

7.4.3 Voltage and Current Measurements

This section presents the voltage and current transducers used in the resonant converter. Two voltage probes are used to measure the output voltage and the load emulator's capacitor voltage for Q estimation and load emulator hysteresis control. One current transducer is employed to measure the output current for closed loop control.

7.4.3.1 Voltage Transducers

In order to implement the control algorithm, the output voltage and the voltage of the load emulator's capacitor must be measured and sampled. For each sampled period the sampled values are updated by the control platform. In this project the sampling frequency is 40 kHz. A specific voltage transducer with a very fast response time is required for this prototype. To satisfy these requirements, two laboratory differential probes were utilised (Differential Probe for Power Measurement- Model 4235 from S J electronics). Figure 7.13 shows the photograph of the utilised voltage probe.

Figure 7.13 the photograph of the laboratory voltage probe

The bandwidth of the probe is 50MHz and the rise time is 7ns which fulfil the requirements. Moreover, the attenuation ratio is 1:100; in case of maximum 400V measured output voltage will give a maximum 4V voltage signal. The 4V voltage signal is within the range of the A/D conversion circuit (±5V); therefore, the output of the probe can be connected directly to the A/D connecters on the FPGA.

7.4.3.2 Current Transducers

Owing to its fast response time, the LEM-LA 55-P current transducer was used to measure the output current so that it can be used in the closed loop control.

The transducer has accuracy of 0.1%, bandwidth of 150 kHz and less than 500ns response time. The schematic diagram of the LEM-LA 55-P current transducer is shown in figure 7.14

Figure 7.14 the LEM-LA 55-P transducer and it is connection diagram

An external 15V power supply is employed to power the current transducer. The current measured by the transducer is converted into a voltage on the FPGA board using the resistor R_M.

7.5 The Resonant Tank

In this project a series resonant tank is proposed which comprises a resonant inductor and resonant capacitor.

7.5.1 Resonant Inductor Design

For high frequency or high power inductors, the multi-strand Litz wire or foil conductors are used in order to minimise winding losses. With a proper winding design, the losses caused by skin effect can be kept at low levels when these conductors are used.

In this project, it was decided to use copper foil wound on the ETD59 ferrite core when building the resonant inductor in order to reduce the skin-effect. The design and the dimension of the ferrite core of this resonant inductor are detailed in Appendix D. Six cores of (Ferrites ETD 59/31/22) have been chosen to be connected in series in order to form the resonant inductor to distribute the voltage stress as the applied voltage on the inductor in the SRSL converter is equal ($Q*v_o$). The photograph of resonant inductor is shown in figure 7.15.
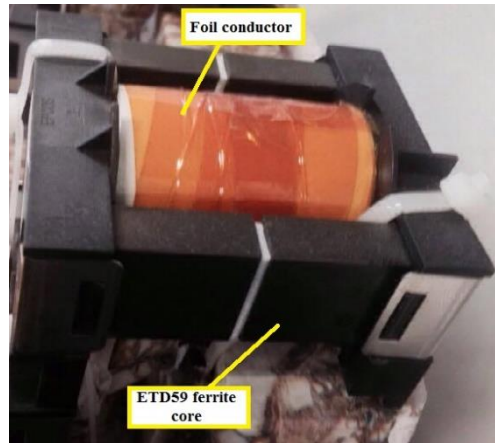
Figure 7.15 the photograph of the resonant inductor

By measuring, with an LCR meter, the total inductance was found to be 0.7875mH compared with the design value of 0.7999mH.

7.5.2 Resonant Capacitor Selection

The required resonant capacitance is 72nF with maximum rated voltage of 2.5kV and the RMS current of 12A. Five 350nF ($\pm 10\%$) $500V_{ac}/1500V_{dc}$ capacitors are connected in series in order to withstand the rated voltage. The five resonant capacitors selected can achieve a capacitance close to the requirement (72nF) and can withstand voltages of up to 2.5kV. They are also capable of withstanding more than 18A rated current. These capacitors were designed and manufactured by ICW Capacitors. The photograph of resonant capacitor is shown in figure 7.16.

Figure 7.16 the photograph of the resonant capacitor

7.6 The Output Stage

7.6.1 The Diode Rectifier and the Output Filter

For this reduced scale prototype, a single phase diode bridge rectifier was utilized to perform the required task. Four ultrafast switching diodes (*STTH30R06*) with specifications of 600V repetitive peak reverse voltage, 30A average forward current and 70ns reverse recovery time were chosen to implement this bridge rectifier. A PCB was designed to achieve the connection between the bridge, the DC filter and the load. The photograph of the output rectifying stage is shown in Figure 7.17.
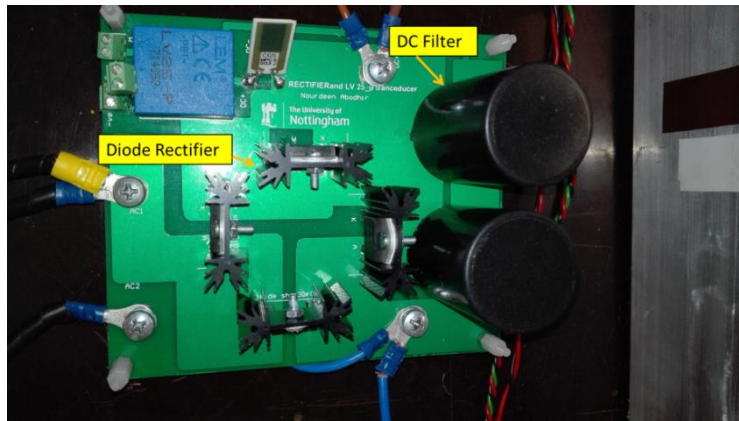
Figure 7.17 photograph of the output rectifying stage

Regarding the output filter, one capacitor cannot smooth all the ripple voltage (unless it was infinitely large). Therefore the capacitor has to be selected according to how much ripple voltage can be tolerated. A voltage ripple less than 5% has been chosen in this work. The required capacitance is 9.5μF. The design of the output filter capacitor is detailed in Appendix A. Two Polypropylene Film Capacitors of 4.7μF, 1500 V dc ±10%, (Cornell-Dubilier UNL series) are connected in parallel to build up the filter capacitor bank. This results in total capacitance of 9.5μF.

7.6.2 The Load Emulator

In the early stage of this project a variable resistor was used as a load to verify the proposed control methodology under variable load conditions. The variable resistance was changing from 41Ω to 25Ω in order to change the load quality factor from 3 to 5 respectively. This stage was implemented to validate the control methodology of maintaining soft switching under variable load

conditions. In order to emulate the magnetron characteristics, a power electronic prototype (chopper based magnetron emulator) was implemented as shown in figure (7.18).
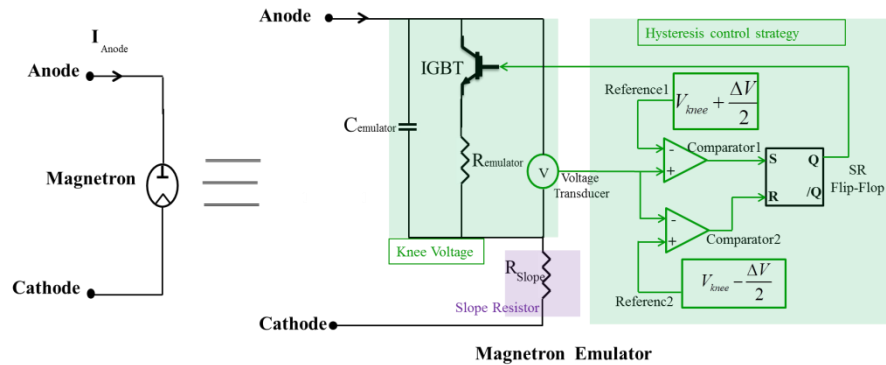
Figure 7.18 reduced scale prototype magnetron emulator

A PCB was designed to connect the IGBT (*FGH20N60SFD*) and its gate drive. The main function of this *IGBT* was to implement the hysteresis control by charging and discharging the emulator capacitor (160µF) to obtain the required hysteresis band voltage. The emulator resistor $R_{emulator}$ was composed of four 15Ω/1.5kW high power resistors connected each two in series and all in parallel, resulting in a total resistance of 15Ω/3kw. The slope resistor R_{slope} was composed of three 15Ω/1.5kW high power resistors connected in parallel, resulting in a total resistance of 5Ω/4.5kW. The photograph of the load emulator is shown in Figure 7.19.
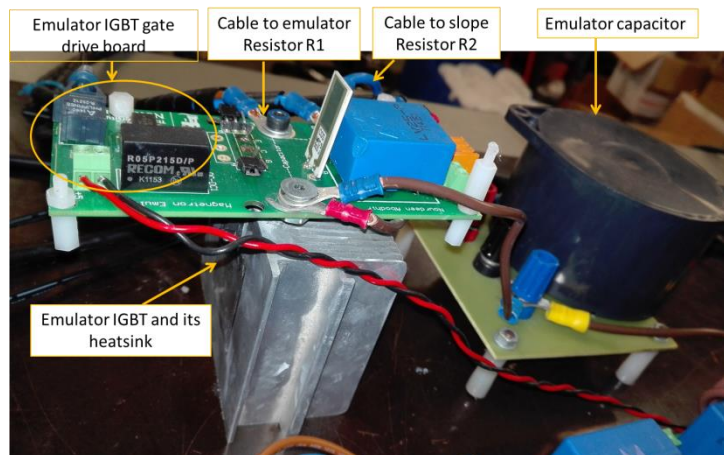
Figure 7.19 photograph of the load emulator

7.7 Experimental Setup

Figure 7.20 shows an overview of the experimental setup of a resonant series converter based topology for an industrial magnetron drive. The converter prototype comprises of a three phase rectifier, DC link capacitors, H-Bridge inverter, resonant tank, transformer, rectifier, filter, associated measurement and control system.
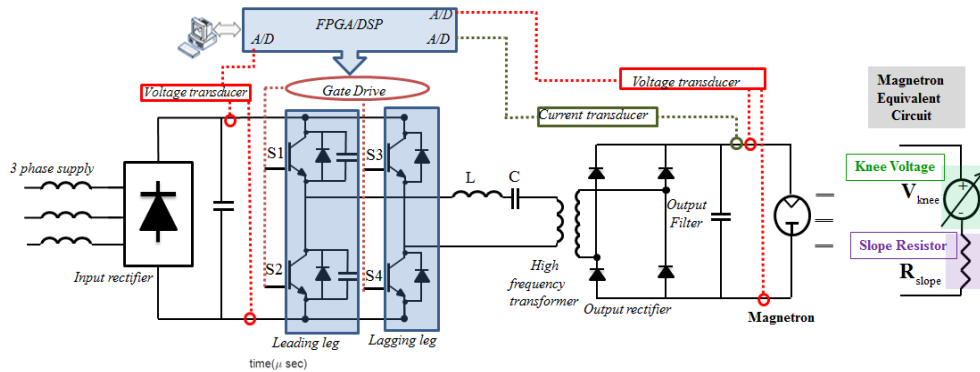
Figure 7.20 SRSL based power converter topology for industrial magnetron drive

A reduced voltage prototype converter was developed and implemented in order to validate the proposed novel control method. Table 7.1 presents the power supply specifications and design results.

The proposed load emulator was used to emulate the changing characteristics of the magnetron when different levels of RF power are used. The reduced voltage prototype was set up according to figure 7.20, with a fixed DC source representing the rectified supply from the mains. The transformer was omitted and the resonant tank was directly connected to the rectifier bridge to minimise the cost. The image of 3kW experimental prototype converter is shown in Figure 7.21.

The output voltage and current were measured and sampled to estimate the quality factor Q. In addition, the input DC link voltage was measured and sampled to implement the closed loop current controller. Furthermore, the knee voltage was measured and sampled in order to implement the hysteresis controller.

Table 7.1 the power supply specifications and design results

	Description	Symbol	Value
	Load voltage	V_o	180V-300V
	Load voltage ripple	V_r	<5%
power	Load current	I	6A-10A
supply	Output power	P	1.8kW-3kW
specifications	Quality factor	Q	2.5 - 5
	Switching frequency	f_{sw}	21.2-24.kHz
	DC-Link	V_{DC}	400V
	Tank inductor	L	0.787mH
Design	Tank capacitor	C	72 nF
Results	Resonant Frequency	f_o	21.14kHz
	Magnetron filter capacitance	C_f	9.6μF
	Emulator capacitor	$C_{emulator}$	160 μF
	Emulator resistor	$R_{emulator}$	15 ohm
	Slope resistor	R_{slope}	5 ohm
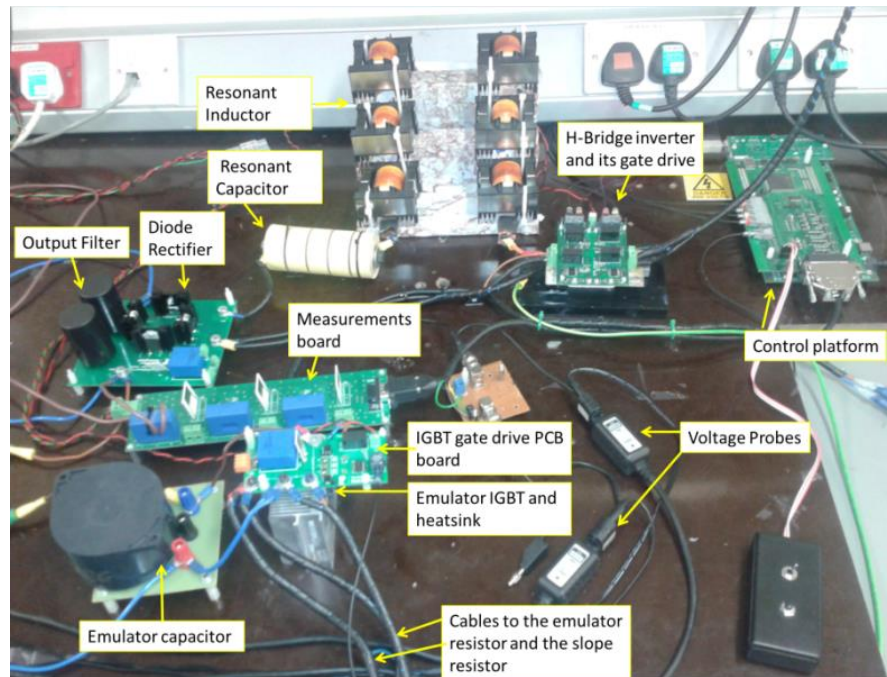
Figure 7.21 overview of the experimental prototype converter

The voltage and the current of the resonant tank were examined for validation of the ZCS. By using the differential voltage probe (*Model-4235 from SJ electronics*), the voltage data measurements were accomplished.

A *LEM-LA55-P* current transducer was used to measure the current data. The following chapter presents a series of practical waveforms which are obtained from the prototype converter.

7.8 Conclusion

This chapter has presented the implementation of a 3kW laboratory prototype in order to verify the proposed control for the SRSL converter under variable load conditions. The converter hardware construction was discussed in detail. Control software implementation and measurement devices have also been introduced. The magnetron emulator has been implemented in order to practically emulate the magnetron characteristics. Finally, the experimental set-up of the prototype is provided, while the experimental results will be presented in Chapter 8.

Chapter 8

EXPERIMENTAL RESULTS

8.1 Introduction

In this Chapter, experimental results are obtained by using the reduced scale prototype described in Chapter 7. The results are presented to illustrate the performance of the proposed SRSL resonant converter and its control method. The following sections present a series of practical waveforms which are obtained from the prototype converter. In addition, the experimental results for the prototype converter will be correlated with the simulation results to validate the proposed converter topology and its control methodology.

8.2 Experimental Waveforms

Experimental results have been obtained. The load emulator proposed in chapter 7 is used to emulate the changing characteristic of the magnetron when different levels of RF power are used. The tank voltage and current are plotted using an oscilloscope (*LeCroy Waverrunner 64xi*). In order to verify the ZCS a Lecroy voltage probe (*ADP300*) and a LeCroy current probe (*CP030*) are utilised to measure the resonant tank voltage and current. The output voltage and current, the quality factor *Q*, the knee voltage and the modulation index waveforms are taken by using *the Host Port Interface HPI*. The experiment was carried out under the closed loop control with a range of switching frequency approximately between 21.2 kHz to 24 kHz and a 400V DC link.

8.2.1 Tank Current and Voltage Waveforms

In order to validate the effectiveness of the variable *Q* based CFPM modulation method, the switching waveforms of the IGBTs (S1, S2, S3, and S4 as shown in Figure 7.20 are inspected, where S1, and S2 are the leading leg (leg A) switches and S3 and S4 are the lagging leg switches (leg B). The voltage across each IGBT is obtained; however, the current through these devices could not be measured as a result of restrictions imposed by the IGBT module. Instead measuring the input current to the resonant tanks, the current through the IGBTs

can be obtained. Figure 8.1 shows the voltage applied on the S3 and the resonant tank current.
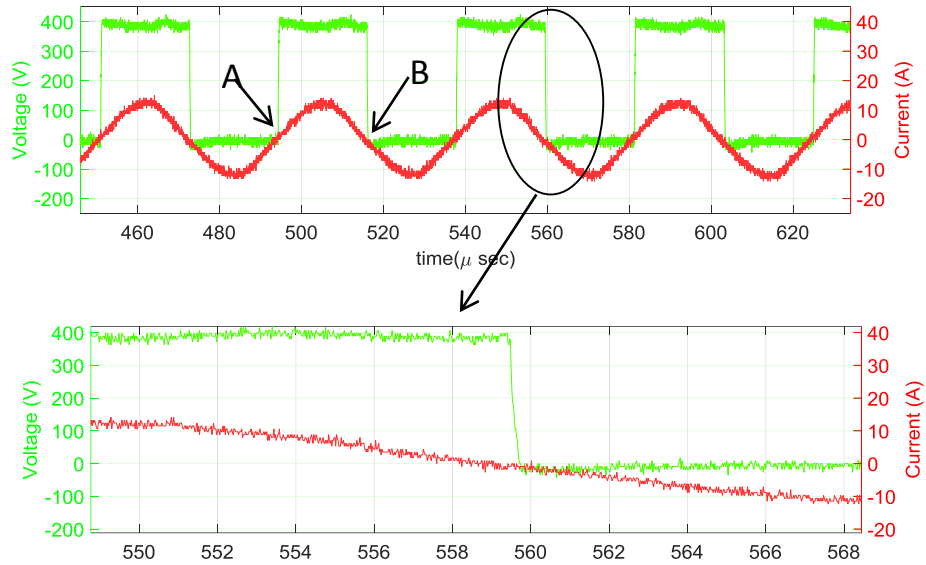
Figure 8.1 voltage applied on the IGBT S3 and the resonant tank current.

The point A in the figure 8.1 shows that the switch voltage rises from 0V to 400V which means that S3 turns OFF and S4 turns ON. At this switching instant, the currents through S3 and S4 are zero (the resonant tank current is zero). This proves that at the point A the S3 is ZCS turned OFF and at the point B S3 is ZCS turned ON. A zoomed-in plot of the voltage across S3 and the resonant tank current is shown to prove that the switching transitions are nearly lossless. It can be seen from the above figure that the loss occurred in the IGBT virtually zero when it was turned ON and OFF.

Figure 8.2 shows the voltage applied on S4 and the resonant tank current. Similarly, at the points A and B S4 switches at zero current, proving that this commutation is soft switched.
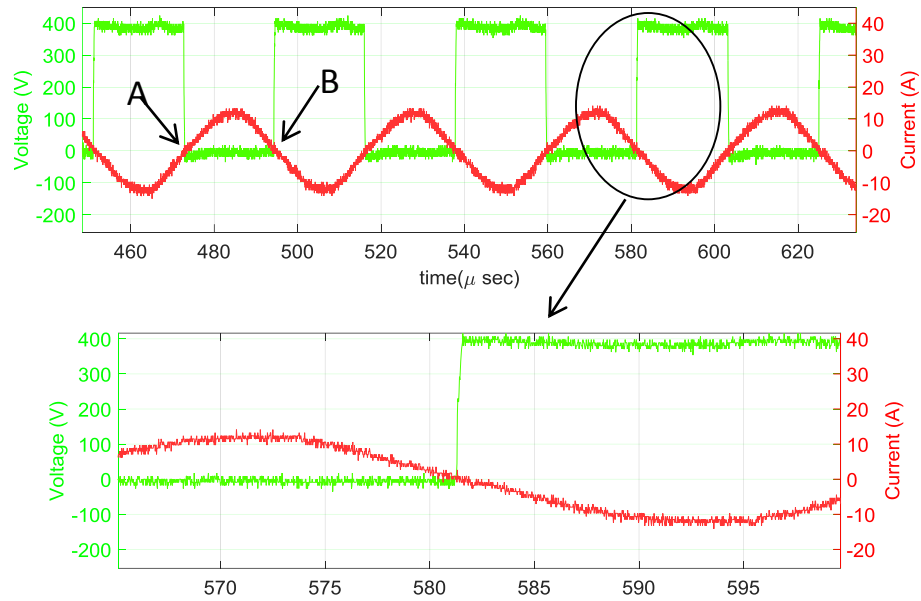
Figure 8.2 voltage applied on the IGBT S4 and the resonant tank current

From the switching waveforms it can be concluded that the control strategy proposed in this study allows the converter lagging leg to achieve approximate ZCS all time.

Figure 8.3 shows the experimental current and voltage waveforms of the resonant tank.
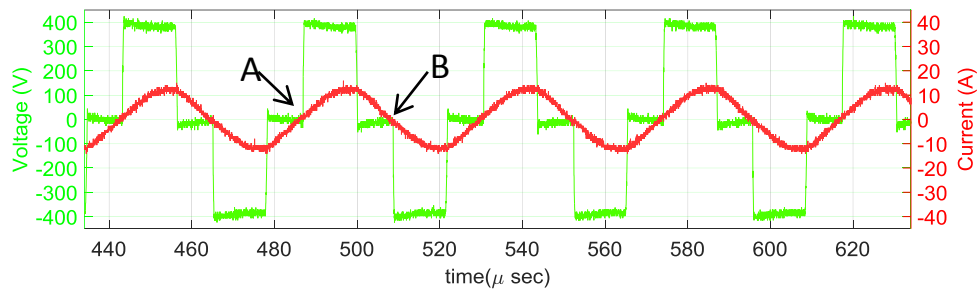
Figure 8.3 resonant tank voltage and current, experimental verification

It is clear from figure 8.3 that the IGBTs in the lagging leg are always switched at the zero crossing point of the tank current, while the ones in the leading leg have soft switching-ON and hard switching-OFF

Figure 8.4 shows the voltage applied to the leading leg switch S1 and the resonant tank current.
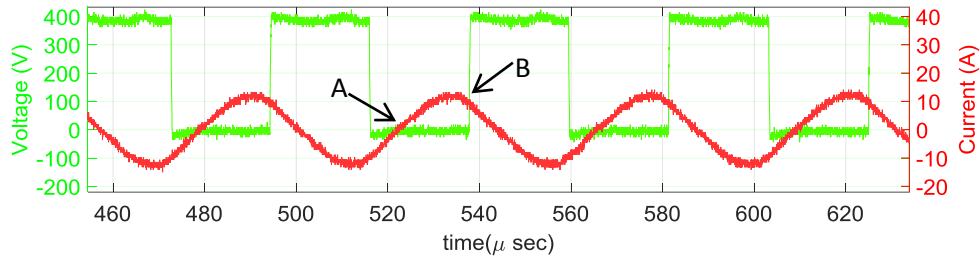
Figure 8.4 voltage applied S1 and the resonant tank current.

It should be noted that at point A S1 is turned ON under ZVS conditions, however, at point B it is turned OFF at significant current. In practice, the placement of snubber capacitor across S1 and S2 will delay the voltage rise resulting in switching loss reduction. Consequently, soft-switching can be obtained at full power in all the IGBTs, which ensures high conversion efficiency. In order to show the voltage rise delay and the current through S1, a current transducer should be connected in series with S1. However, this is practically difficult to be implemented as a result of restrictions imposed by the IGBT module. Experimentally S1 and S2 maintained soft switching due to the implementation of the designed snubber capacitor, which enables delaying voltage rise preventing switching losses as discussed in section 5.3.2.

8.2.2 Load Current and Voltage Waveforms

Figure 8.5 shows an experimental result for the dynamic and steady state response of the Knee voltage to verify the hysteresis controller operation of the magnetron emulator. The hysteresis controller is able to change the knee voltage from 214V to 205V. It should be noted however, that the output current remains constant as the current controller demand was set at a fixed value (7.3A).
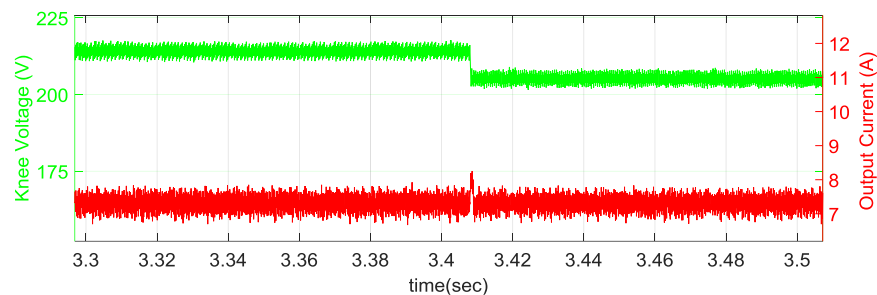
Figure 8.5 response of the knee voltage to the hysteresis control demand

In addition, figure 8.6 shows the knee voltage waveforms with the resonant converter actuator signal or the modulation index. All results in this section are tested under closed loop control condition and the current controller demand was set at a fixed value (7.3A). It is clear in figure 8.6 that the knee voltage and the modulation index have directly proportional relationship, the lower the knee voltage the lower the modulation index.
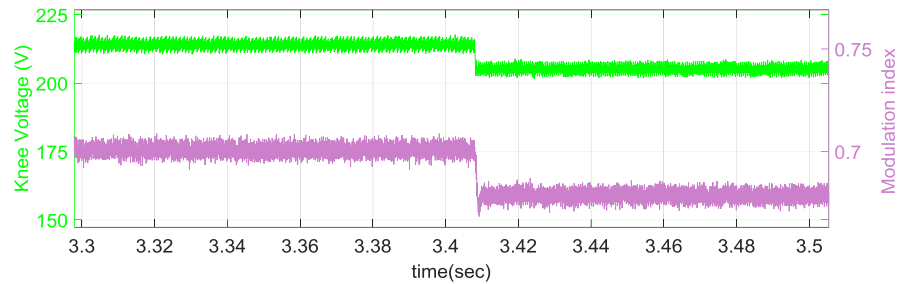
Figure 8.6 the knee voltage waveforms with SRSL modulation index

For the same fixed value of the output current, the lower the knee voltage, the higher the quality factor, as the relationship is inversely proportional. The modulation index in figure 8.6 is to illustrate that when the knee voltage demand changes, the SRSL resonant converter modulation index changes in order to calculate the new soft switching point. This change is expected, when the knee voltage changes and the output current remains fixed, the Q of the circuit has changed, thus requiring the control to vary the modulation index to track the new soft switching point.

This is clear in figure 8.7, where the knee voltage is reduced from 214V to 205V and at the same time the quality factor increases from 3.7 to 4.
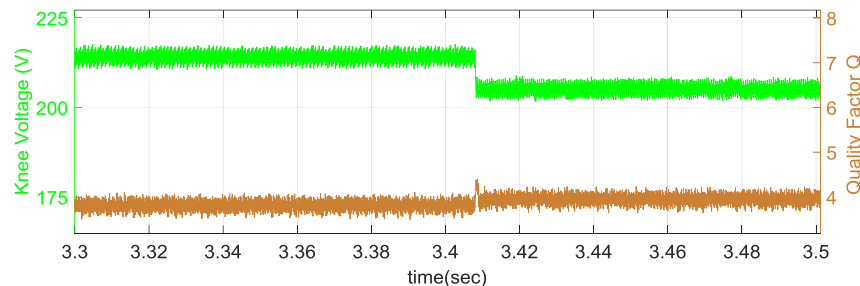
Figure 8.7 knee voltage waveforms with quality factor Q

8.2.3 Response to the Current Demand Changes

In order to test the current controller response practically, a demand change from 7.3A to 8.7A was applied. Figure 8.8 shows the output current and the reference current demand. It is clear that the output current follows the reference demand current. No overshoot during the transient appears in the load current as designed and expected.
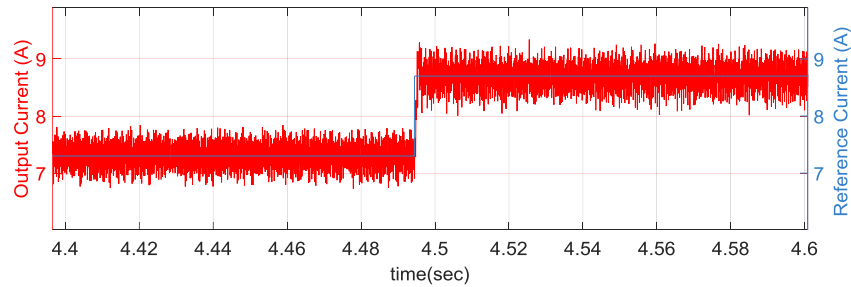
Figure 8.8 output current and the reference current demand

Figure 8.9 shows the waveforms of the knee voltage and the output current. When the hysteresis control is set at fixed value 205V and the output current demand is increased from 7.3A to 8.7A; the knee voltage remains constant. This illustrates that the current can be varied at a particular knee voltage in order to vary the output power of the magnetron.
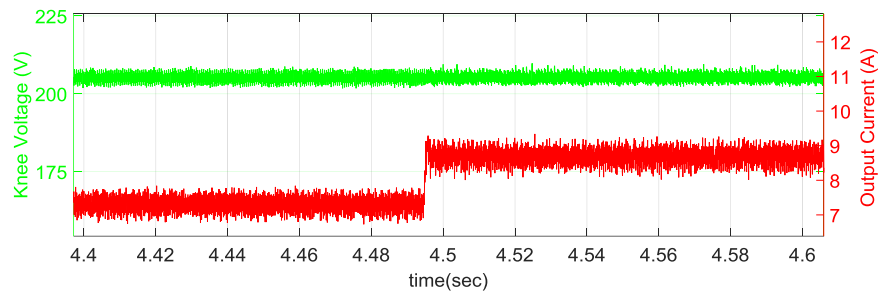
Figure 8.9 knee voltage and the output current

Figure 8.10 shows the output current and the load quality factor waveforms. At a particular knee voltage, the load quality factor is increased from 4 to 4.7 when the load current is increased from 7.3A to 8.7A.
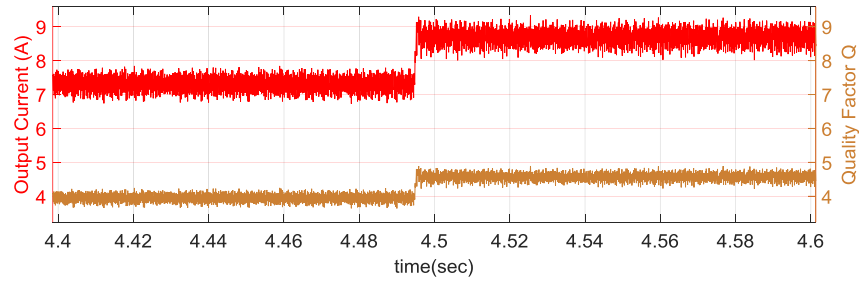
Figure 8.10 output current and the load quality factor waveforms

Figure 8.11 shows the relationship between the output current and the modulation index. By increasing the output current (magnetron anode current) the modulation index (actuator signal) is increased.
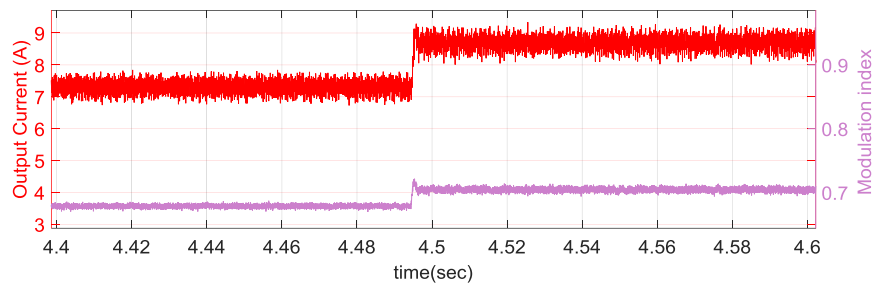
Figure 8.11 output current and the modulation index

This change in the modulation index and the load quality factor provides new values for both the normalized frequency, *F,* and the phase angle between the leading and the lagging legs. These new values impose the lagging leg to switch at zero current and maintain the knee voltage at a fixed value.

Figure 8.12 shows the experimental current and voltage waveforms of the resonant tank when the output current (anode current) is demanded by the current controller to change and the hysteresis controller is demanded to maintain the knee voltage at constant value. This lead to variable load condition (variable Q).
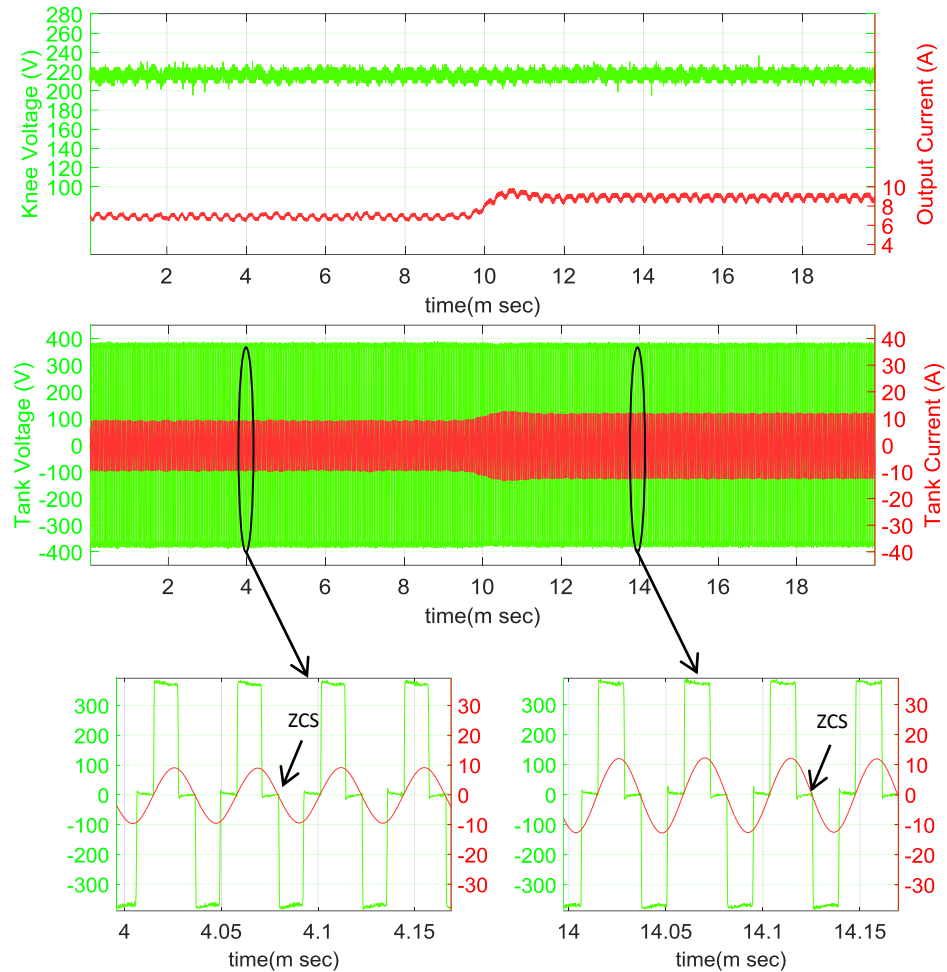
Figure 8.12 the experimental current and voltage waveforms

From figure 8.12 it can be noted that although *Q* is changed, the IGBTs in the lagging leg are always switched at the zero crossing point of the tank current. This proves that the proposed control methodology is able to maintain soft switching when the load is changed.

8.3 Correlation between the Simulation and the Experimental Results

Figure 8.13 shows the knee voltage including the output ripple voltage ΔV for both simulation and experimental conditions. Figure 8.13a shows a PLECS simulation for the knee voltage when the hysteresis control is set to give a 214V average knee voltage with 2V output voltage ripple. Figure 8.13b shows an experimental result for the same setting. It is clear that the hysteresis controller could regulate the knee voltage accurately.
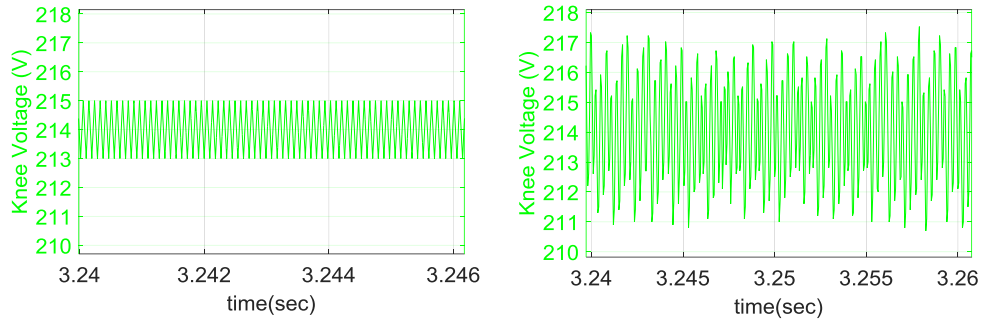
Figure 8.13 knee voltage in steady state, (a) simulation results, (b) experimental results

Figure 8.14 shows a PLECS simulation and experimental result for the knee voltage when the hysteresis control is set to give 214V average knee voltage with 2V output voltage ripple. The hysteresis controller is able to change the knee voltage from 214V to 205V. As discussed in chapter 6, the change in the knee voltage will emulate the change in the magnetic field applied to the tube in the real magnetron.
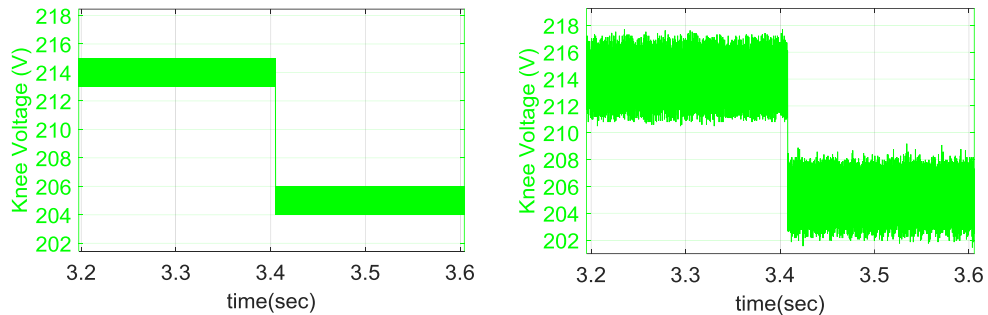
Figure 8.14 knee voltage in transient, (a) PLECS simulation, (b) Experimental verification

Figure 8.15 shows a step change of the output current reference from 7.3A-8.7A (consequently the Q, of the resonant circuit undergoes a step change) in order to test the transient behaviour of the control method and also to prove that the resonant converter control could drive a variable load. The change in the reference current will emulate the change in the anode current demand in a real magnetron. A combination of both the knee voltage and the reference current can be applied in order to find the most efficient *RF* generation point for a given load as discussed in chapter 6.
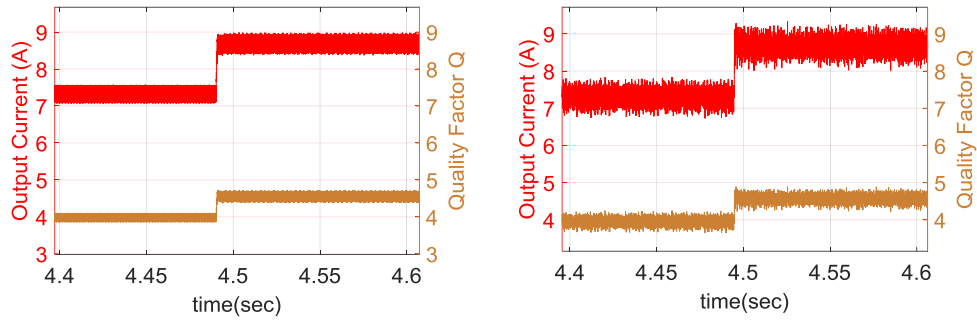
Figure 8.15 step change of the output current reference and consequently Q (a) simulation results (b) experimental verification

Figure 8.16 shows the simulation and experimental current and the voltage waveforms of the resonant tank. The IGBTs in the lagging leg are always switched at the zero crossing point of the tank current, while the ones in leading leg have soft switching ON and hard switching OFF. A snubber capacitor is utilized to achieve ZVS in the off commutation. Consequently, soft-switching can be obtained at full power in all the IGBTs. The experimental results present a very close match with the simulation results.
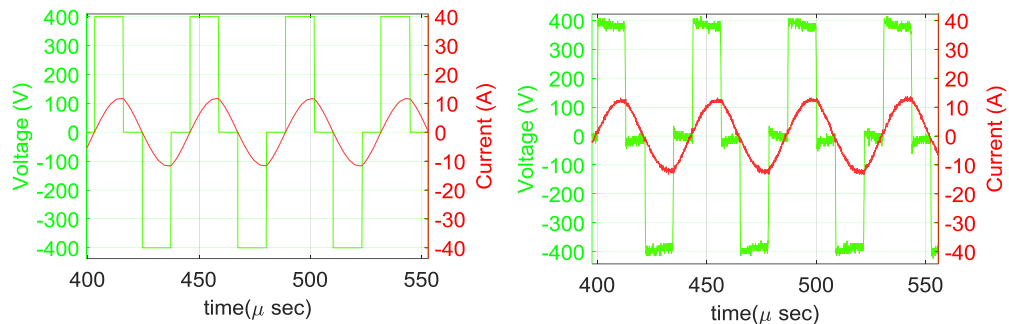
Figure 8.16 resonant tank voltage and current, (a) simulation results, (b) experimental verification

8.4 Conclusion

This chapter has presented the experimental verification for the proposed converter and the magnetron emulator. A vast amount of experimental results were taken to evaluate the control performance and the operation of the magnetron emulator. Soft switching was achieved for all power devices ensuring a high efficiency. Moreover, the stability of the proposed controls (variable Q based CFPM modulation method and the hysteresis control for the magnetron emulator) were also successfully verified. Furthermore, in order to validate the

modelling approach, control design and modulation method, a correlation between simulation and experimental results is demonstrated. It can be concluded that the proposed converter topology and the control approach are feasible in practice for a higher power system.

Chapter 9

CONCLUSIONS AND FURTHER WORK

9.1 Conclusion

In the last decade, the development in power electronics has significantly progressed in many areas, including semiconductor devices, circuit topologies and control techniques. With these advances there has been an increased demand in various fields to develop power converters with high efficiency and high operating frequency; the general aim being to produce compact and highly efficient architectures for such applications.

Resonant power converters have been considered in many cases to replace traditional approaches, owing to their high efficiency and high power density features. The main advantage of using the resonant converters is the potential to operate power switching semiconductors at high switching frequencies without significantly compromising converter efficiency. For various applications, different resonant converter topologies with associated modulation and control techniques have been proposed in the literature.

This thesis presented research on a compact and efficient power supply for variable load conditions, such as those that may be present in industrial microwave processing systems. The conventional power supplies for these systems rely on a large line frequency transformers (for scaling and isolation) and require large passive filters to attenuate low frequency harmonic voltages and currents at the load connection.

In this study the operating principle of the industrial magnetron and its performance chart were discussed in order to provide good understanding of the load characteristics. Then, some microwave heating applications were presented. The previous work in resonant power converters for RF tube modulators that was carried out by PEMC research group at the University of Nottingham was briefly introduced in order to develop a novel topology, which

may overcome the previous work limitations. The design of the proposed compact power supply for RF applications has been considered. This proposed converter was based on a series resonant series loaded (SRSL) resonant topology. It offers a numerous advantages over the conventional topologies. The use of the input passive rectifier and the DC link capacitor guarantee constant power absorption. The series resonant tank capacitor blocks any DC components produced by the inverter and prevents the high voltage transformer from saturation. As the topology is comprised of a resonant DC-AC current source inverter, there is no need for the output inductive filter. The operation at high frequency offers a significant reduction in the reactive component of the output filter.

Several modulation techniques were used to modulate the load resonant converters, a combined frequency and phase shift modulation technique (CFPM) is preferable to reduce the switching losses for the H-Bridge. By utilising the CFPM modulation, the lagging leg devices of the H-Bridge maintains soft switching. With regard to the leading leg devices, a capacitive snubber was added to delay the voltage rise at the turn off transition resulting in significant reduction of the switching losses. The leading leg switching losses decreased significantly when the designed snubber capacitor was used.

The use of the CFPM technique presented in previous literature has assumed that the load is constant and the corresponding quality factor Q of the resonant circuit is fixed. This assumption could be limiting factor in some applications where the ability to operate with variable load conditions for different output requirements may be advantages such as in cavity magnetrons. In order to avoid this limitation, a novel variable Q based CFPM modulation technique was developed in this work. The accurate Q was online tracked through the load voltage and current characteristics. As a result, although the converter drives a variable load condition, the soft switching can be always maintained. It was clear from the simulation and experimental results that the modulation technique enables efficient operation of the proposed converter under variable load conditions, by maintaining soft switching in the lagging leg devices of the converter across this operational load range.

In order to enable closed loop controller design for the converter, a DQ modelling method was adopted to model the proposed converter due to its simpler mathematical derivation and reduced computational effort compared with the other methods used to model the load resonant converter. In this work the DQ modelling method was used to derive the relationship between the converter output current and the tank input voltage. Based on this model the system transfer function was obtained and the state space equations were formulated to enable the design of the closed loop output current controller. The PLECS simulation platform was used to verify the DQ modelling approach. The simulation results obtained for the models (DQ, actual converter and state space representations models) were a close match and therefore concluded that the DQ model is suitable for this high order system and that it can be used to analyse the steady state and dynamic performance for load resonant converter accurately. According to the plant transfer function obtained from the DQ model, a PI current controller was designed for the converter by using the SISO tool in MATLAB.

Based the characteristics of the magnetron, an emulator prototype was proposed and developed to represent the magnetron load behaviour in a lower voltage laboratory environment. Simulation results using PLECS were provided for full power scale of the proposed magnetron power supply (SRSL DC-DC power converter) and magnetron emulator in order to demonstrate their feasibility. The simulation results showed that the soft switching was achieved for all power devices of the resonant converter ensuring a high efficiency. Moreover, the stability of the proposed controls was also successfully verified.

A laboratory prototype converter rated at 3kW was designed and developed in order to verify the proposed control for the SRSL converter under variable load conditions. This avoids the issues related with the production of high voltage whilst still enabling validation of the proposed control methodologies.

A vast amount of experimental results under closed loop control were obtained and compared with simulation results. Good correlation between experimental and simulation results were achieved. With the use of the proposed control methodology, the ZCS turn ON and turn OFF for the lagging leg were achieved

despite the load was being changed, allowing operation at high frequency with minimum losses which validates the control design and the novel modulation approach . It can be therefore concluded that the proposed converter and its control methodology operates as intended and suitable for the practical implementation of a high power converter.

9.2 Further Work

Although the concept of the novel modulation technique and the feedback control strategy has been proved successfully in practice, there are still some tasks need to be considered.

- The prototype could be extended to higher powers by increasing the component rate to meet the real industrial magnetron rating in order verify the approach for a higher power level and investigate operation with a real magnetron load.
- The work only considers steady state relationship for complex circuit which may be subjected to component value changes due to aging (for example). Further closed loop control methods should be considered to nullify these effects.
- Consideration of the effect of the high voltage high frequency transformer on the tank parameters.

9.3 Publications

1- Author

o Nourdeen A. Abodhir, Alan J. Watson, Jon C. Clare, "Control of HV Series Resonant Power Supply for Industrial Magnetrons", IET-PEMD 2014.

o Nourdeen A. Abodhir, Alan J. Watson, Chao Ji, Jon C. Clare, '' Resonant Converter Based Modulator Control for Magnetron with Variable Load'', IEEE-EPE 2014.

o Nourdeen A. Abodhir, Alan J. Watson, Chao Ji, Jon C. Clare, '' Design and Implementation of Magnetron Power Supply and Emulator '', IEEE-EPE 2016.

2- Co-Author

o Alan J. Watson, Chao Ji, Nourdeen A. Abodhir, Jon C. Clare, E. Reyes-Moraga "Resonant Power Electronics for Pulsed Power and High Voltage Applications", UK Pulsed Power Symposium, 2014.

o Chao Ji, Alan J. Watson, Nourdeen A. Abodhir, Jon C. Clare, "High Efficiency Operating Point Tracking Techniques for Resonant Power Converters in High Power RF Applications", UK Pulsed Power Symposium, 2014

Appendix A

The output filter design

Figure A.1 shows the output stage and the waveforms of the output filter.
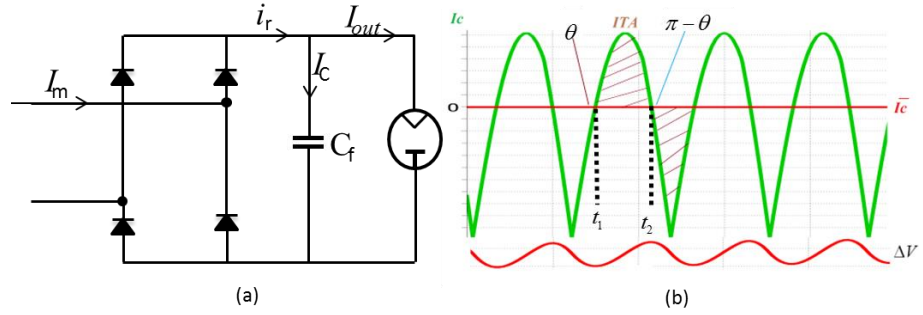
Figure A.1 (a) the output stage, (b) the waveforms of the output capacitor filter

From the waveforms of the output capacitor filter shown in figure A.1, the filter size is designed as following:

$$i_r = I_c + I_{out} \tag{A.1}$$

$$i_r = I_m \sin\theta \tag{A.2}$$

$$I_{out} = \frac{V_o}{R} \tag{A.3}$$

$$\bar{I}_c = 0 \tag{A.4}$$

From (A.1), (A.2) and (A1.3) the equation (A.5) is obtained.

$$I_m \sin\theta - \frac{V_o}{R} = 0 \Rightarrow \sin\theta = \frac{2}{\pi} \tag{A.5}$$

The current time area (ITA), can be obtained as:

$$ITA = \int_{t_1}^{t_2} (I_m \sin\omega t - \frac{V_o}{R}) \, dt \tag{A.6}$$

Where, $t_1 = \dfrac{\theta}{\omega}$ and $t_2 = \dfrac{\pi - \theta}{\omega}$. t_2.

Filter capacitance is given by (A.7). Where, ΔV is peak to peak voltage ripple.

$$C = \frac{ITA}{\Delta V} \tag{A.7}$$

Appendix B

SRSL Analysis

The SRSL converter is shown in figure B.1
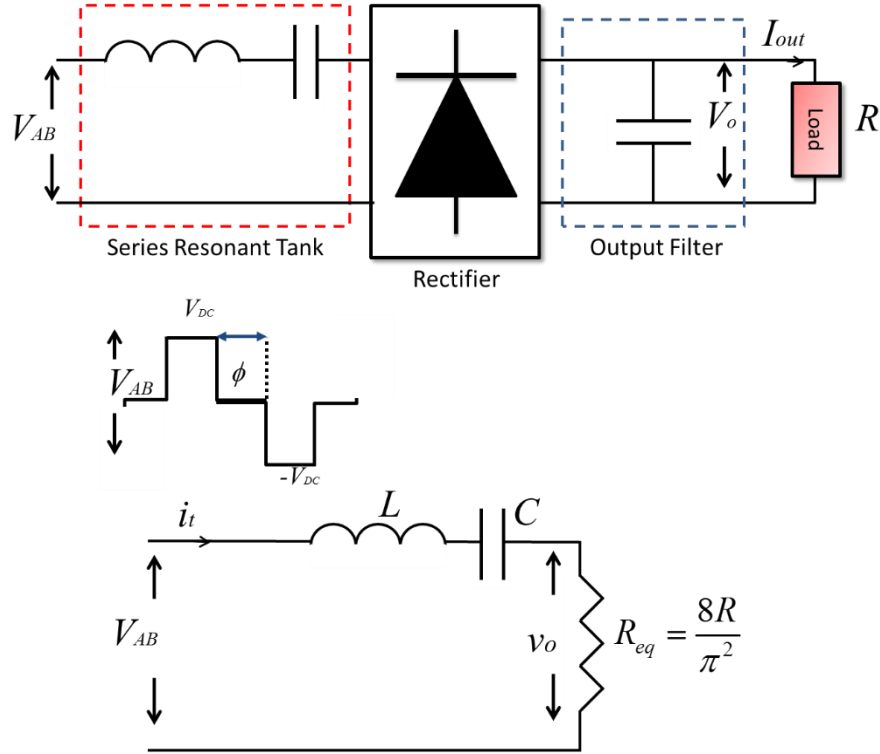
Figure B.1 the SRSL converter

The tank input voltage given by

$$V_{AB} = \frac{4V_{DC}}{\pi} \cos\frac{\phi}{2}$$

(B.1)

The tank output voltage given by

$$v_o = \frac{4V_o}{\pi}$$

(B.2)

The output load current given by

$$I_{out} = \frac{2\hat{i}_t}{\pi}$$

(B.3)

The resonant frequency given by

$$\omega_o = \frac{1}{\sqrt{LC}}$$

(B.4)

The characteristic impedance given by

$$z_o = \sqrt{\frac{L}{C}} = \omega_o L = \frac{1}{\omega_o C} \qquad \text{(B.5)}$$

The quality factor given by

$$Q = \frac{Z_o}{R_{eq}} \qquad \text{(B.6)}$$

The normalised frequency given by

$$F = \frac{\omega}{\omega_o} \qquad \text{(B.7)}$$

The tank impedance given by

$$\mathbf{Z} = R_{eq} + j(X_L - X_c) = R_{eq} + j(\omega L - \frac{1}{\omega C}) = R_{eq} + jZ_o\left(F - F^{-1}\right) \qquad \text{(B.8)}$$

$$|Z| = R_{eq}\sqrt{1 + Q^2(F - F^{-1})^2} = Z_o\sqrt{\frac{1}{Q^2} + (F - F^{-1})^2} \qquad \text{(B.9)}$$

From figure B.2, the tank phase shift is given as in (B.10)
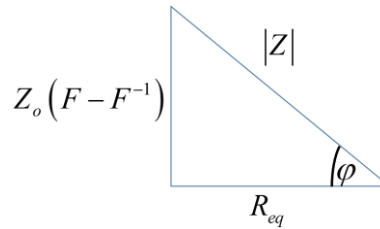
Figure B.2 the tank phase shift

$$\varphi = \arctan[Q.(F - F^{-1})] \qquad \text{(B.10)}$$

$$R_{eq} = Z\cos\varphi \qquad \text{(B.11)}$$

$$X = Z\sin\varphi \qquad \text{(B.12)}$$

$$\cos\varphi = \frac{1}{\sqrt{1 + Q^2(F - F^{-1})^2}} \qquad \text{(B.13)}$$

147

Lagging leg commutation current

Commutation current in the lagging leg when Q is incorrect. Assume M is given and F, ϕ_{nom} result in ZCS for the correct value of Q. Let nominal Q_{nom} = correct value of Q. Vary Q and keep F and ϕ_{nom} constant, phase shift of the tank for correct Q is equal to φ_{nom}, where $\varphi_{nom} = \dfrac{\phi_{nom}}{2}$. At any other phase shift, the current at commutation is given by

$$I_{com} = \hat{i}_t \sin(\varphi - \varphi_{nom}) \tag{B.14}$$

Where φ is the new tank phase shift.

φ_{nom} Is given by

$$M_{nom} = \cos^2 \varphi_{nom} \tag{B.15}$$

$$\sin(\varphi - \varphi_{nom}) = \sin\varphi\cos\varphi_{nom} - \cos\varphi\sin\varphi_{nom} \tag{B.16}$$

$$\cos\varphi_{nom} = \sqrt{M_{nom}} \tag{B.17}$$

$$\sin\varphi_{nom} = \sqrt{1 - M_{nom}} \tag{B.18}$$

$$\cos\varphi = \frac{1}{\sqrt{1 - Q^2(F - F^{-1})^2}} \tag{B.19}$$

$$\sin\varphi = \frac{Q(F - F^{-1})}{\sqrt{1 - Q^2(F - F^{-1})^2}} \tag{B.20}$$

Then

$$\sin(\varphi - \varphi_{nom}) = \frac{Q(F - F^{-1})\sqrt{M_{nom}} - \sqrt{1 - M_{nom}}}{\sqrt{1 + Q^2(F - F^{-1})^2}} \tag{B.21}$$

It is given that

$$I_{out} = \frac{MV_{DC}}{R} \tag{B.22}$$

$$R = \frac{\pi^2 R_{eq}}{8} = \frac{\pi^2 Z_o}{8Q} \tag{B.23}$$

$$\hat{i}_t = \frac{\pi}{2} I_{out} \tag{B.24}$$

The peak tank current can be written as:

$$\hat{i}_t = \frac{4MV_{DC}Q}{\pi Z_o} = \frac{4MV_{DC}Q}{\pi\sqrt{\dfrac{L}{C}}} \tag{B.25}$$

From (B.14) and (B.21) the commutation current is given as in (B.26).

$$I_{com} = \frac{4MV_{DC}Q}{\pi Z_o}\left[\frac{Q(F-F^{-1})\sqrt{M_{nom}} - \sqrt{1-M_{nom}}}{\sqrt{1+Q^2(F-F^{-1})^2}}\right] \tag{B.26}$$

Also it is derived that

$$\tan\varphi_{nom} = Q(F-F^{-1}) = \sqrt{\frac{1}{M_{nom}} - 1} \tag{B.27}$$

$$(F-F^{-1}) = \frac{1}{Q_{nom}}\sqrt{\frac{1}{M_{nom}} - 1} \tag{B.28}$$

By substituting (B.27) and (B.28) into (B.26) the lagging leg commutation current can be written as:

$$I_{com} = \left(\frac{4V_{DC}Q}{\pi\sqrt{\dfrac{L}{C}}}\right)\left(\frac{\left(\dfrac{Q}{Q_{nom}} - 1\right)\left(\sqrt{1-M_{nom}}\right)}{\sqrt{\left(1+(\dfrac{Q}{Q_{nom}})^2\right)\left(\dfrac{1}{M_{nom}} - 1\right)}}\right) \tag{B.29}$$

Leading leg commutation current

When operating at ZCS on the other leg (lagging leg). Then the tank phase angle is defined as:

$$\varphi = \frac{\phi}{2} \tag{B.30}$$

$$V_o = V_{DC}\cos^2\varphi \tag{B.31}$$

And modulation index is defined as:

$$M = \frac{V_0}{V_{DC}} = \cos^2\varphi \tag{B.32}$$

Commutation current is given by

$$I_{com} = \hat{i}_t\sin\phi = \hat{i}_t\sin 2\varphi \tag{B.33}$$

$$\sin 2\varphi = 2\sin\varphi\cos\varphi \tag{B.34}$$

Then

$$\cos \varphi = \sqrt{M} \tag{B.35}$$

$$\sin \varphi = \sqrt{1-M} \tag{B.36}$$

$$I_{com} = 2\hat{i}_t \sqrt{M} \sqrt{1-M} \tag{B.37}$$

Where

$$\hat{i}_t = \frac{I_{out}\pi}{2}, I_{out} = \frac{V_o}{R} \Rightarrow I_{out} = \frac{MV_{DC}}{R} \tag{B.38}$$

And

$$R = \frac{\pi^2 R_{eq}}{8} = \frac{\pi^2 Z_o}{8Q} \tag{B.39}$$

From the above two equations the tank current is given by

$$\hat{i}_t = \frac{4MV_{DC}Q}{\pi Z_o} = \frac{4MV_{DC}Q}{\pi \sqrt{\dfrac{L}{C}}} \tag{B.40}$$

Then the leading leg commutation current can be written as:

$$I_{com} = \frac{8MV_{DC}Q}{\pi Z_o} \sqrt{M} \sqrt{1-M} \tag{B.41}$$

Switching loss

The output power is given by

$$P_{out} = I_{out}MV_{DC} \tag{B.42}$$

The output load current is given by

$$I_{out} = \frac{8MV_{DC}Q}{\pi^2 Z_o} \tag{B.43}$$

The output power is rewritten as

$$P_{out} = \frac{8M^2(V_{DC})^2 Q}{\pi^2 Z_o} \tag{B.44}$$

The device switching loss is given by

$$P_{loss} = \frac{I_{com}V_{DC}t_{fall}}{2} f \tag{B.45}$$

The total switching loss of the leading leg

$$2P_{loss} = I_{com}V_{DC}t_{fall}f \tag{B.46}$$

The commutation loss normalised to the output power

$$\frac{I_{com}}{P_{out}} = \frac{\pi}{V_{DC}} \sqrt{\frac{1}{M} - 1} \tag{B.47}$$

The leading leg switching loss normalised to the output power

$$\frac{2P_{loss}}{P_{out}} = \left(\pi \sqrt{\frac{1}{M} - 1} \right)(t_{fall})f \tag{B.48}$$

E_{off}^{n} Is the normalised turn-off energy loss and measured by (nJ/VA). This value can be taken from the datasheet of given device.

The device turn-off loss is given by

$$P_{loss} = I_{com} V_{DC} E_{off}^{n} f \tag{B.49}$$

The device turn-off loss normalised to the output power is given by.

$$\frac{P_{loss}}{P_{out}} = \left(\pi \sqrt{\frac{1}{M} - 1} \right)(E_{off}^{n})f \tag{B.50}$$

The leading leg turn-off loss normalised to the output power is given by.

$$\frac{2P_{loss}}{P_{out}} = \left(2\pi \sqrt{\frac{1}{M} - 1} \right)(E_{off}^{n})f \tag{B.51}$$

Leading leg switching loss when the snubber is used

The maximum commutation current is given by

$$I_{com}^{max} = \frac{8V_{DC}Q_{max}}{\pi Z_o} M \sqrt{M} \sqrt{1-M} \tag{B.52}$$

The snubber capacitive is given by

$$C = \frac{I_{com}^{max} t_{fall}}{2V_{DC}} \tag{B.53}$$

V_C', is the voltage on the snubber capacitor when the commutation current is zero and it is given as.

$$V_C' = (\frac{I_{com}}{2})(\frac{t_{fall}}{2C}) \tag{B.54}$$

From the above two equations and if M=constant the V_C' is given by:

$$V_C' = (\frac{I_{com}}{I_{com}^{max}})(\frac{V_{DC}}{2}) = (\frac{Q}{Q_{max}})(\frac{V_{DC}}{2}) \tag{B.55}$$

The device switching loss when the snubber is used is given by:

$$P_{loss} = (\frac{I_{com}V'_C t_{fall}}{24})f \qquad (B.56)$$

By substituting (B.52) and (B.55) into (B.56) the device switching loss can be written as:

$$P_{loss} = (\frac{V_{DC}^2 Q^2 M \sqrt{M} \sqrt{1-M}}{3\pi Z_o Q_{max}})t_{fall}f \qquad (B.57)$$

The output power is given as:

$$P_{out} = \frac{8M^2(V_{DC})^2 Q}{\pi^2 Z_o} \qquad (B.58)$$

The normalised leading leg switching loss to the output power when the snubber is used is given by

$$\frac{2P_{loss}}{P_{out}} = (\frac{\pi}{12}\frac{Q}{Q_{max}}\sqrt{\frac{1}{M}-1})\,t_{fall}\,f \qquad (B.59)$$

Appendix C

DQ Equation Derivation

The combined complex equivalent circuit shown in Figure 6.3 can be transformed into the DQ domain by using equations (6.14), (6.15) and (6.16). The equation derivation for each circuit component is presented as following, where θ is selected to be equal to ωt.

Voltage Source Vs

$$
\begin{aligned}
V_{s_{dq}} &= V_{s_d} - V_{s_q} \cdot j \\
&= (V_s \cos \omega t + V_s j \sin \omega t) e^{-j\omega t} \\
&= V_s + j0
\end{aligned}
\tag{C.1}
$$

Resonant Inductor L

$$
V_\alpha + jV_\beta = L\frac{d}{dt}(i_{t_\alpha} + ji_{t_\beta})
\tag{C.2}
$$

$$
\begin{aligned}
(V_d - jV_q)e^{j\omega t} &= L\frac{d}{dt}\left[e^{j\omega t}\left(i_{t_d} - ji_{t_q} \right) \right] \\
&= Le^{j\omega t}\left[\frac{di_{t_d}}{dt} - j\frac{di_{t_q}}{dt} \right] + Le^{j\omega t} j\omega\left[i_{t_d} - ji_{t_q} \right]
\end{aligned}
\tag{C.3}
$$

Cancelling $e^{j\omega t}$ yields,

$$
\begin{aligned}
V_d &= L\frac{di_{t_d}}{dt} + L\omega i_{t_q} \\
V_q &= L\frac{di_{t_q}}{dt} - L\omega i_{t_d}
\end{aligned}
\tag{C.4}
$$

Resonant Capacitor C

$$
i_{t_\alpha} + ji_{t_\beta} = C\frac{d}{dt}(V_{c\alpha} + jV_{c\beta})
\tag{C.5}
$$

$$
\begin{aligned}
(I_d - jI_q)e^{j\omega t} &= C\frac{d}{dt}\left[e^{j\omega t}\left(V_{cd} - jV_{cq} \right) \right] \\
&= Ce^{j\omega t}\left[\frac{dV_{cd}}{dt} - j\frac{dV_{cq}}{dt} \right] + Ce^{j\omega t} j\omega\left[V_{cd} - jV_{cq} \right]
\end{aligned}
\tag{C.6}
$$

Cancelling $e^{j\omega t}$ yields,

$$I_d = C\frac{dV_{cd}}{dt} + C\omega V_q$$

$$I_q = C\frac{dV_{cq}}{dt} - C\omega V_d \qquad (C.7)$$

Voltage source v_o

$$v_{o\alpha\beta} = \left(\frac{4V_o}{\pi n}\right)\left(\cos(\omega t - \varphi) + j\sin(\omega t - \varphi)\right) \qquad (C.8)$$

$$(v_{od} - jv_{oq})e^{j\omega t} = \left(v_{o\alpha} + v_{o\beta}\right) = \frac{4V_o}{\pi n}e^{j(\omega t - \varphi)} \qquad (C.9)$$

$$(v_{od} - jv_{oq}) = \frac{4V_o}{\pi n}e^{-j\varphi} \qquad (C.10)$$

$$v_{od} = \frac{4V_o}{\pi n}\cos\varphi \qquad (C.11)$$

$$v_{oq} = \frac{4V_o}{\pi n}\sin\varphi \qquad (C.12)$$

Appendix D

Resonant inductor design

Several steps have been carried out in order to design the resonant inductor. The first step is identifying the required inductor specifications, the second step is selecting the magnetic core and the last step is calculation the winding and verifying the structure design.

Inductor Specifications

The inductors used in the resonant tanks should meet the following specifications:

The required inductance L=0.799mH.

The voltage applied on the inductor is Q multiplied by input tank voltage V_{AB}.

The operating frequency: $f \approx 20\text{kHz}$.

The Magnetic Core Selection

In order to select the core for the design of resonant inductor, the area product method is used. It is based on calculation of product area (A_p) by assuming the windows utilization factor (K_u) and the maximum flux density (B_m) [78]. Moreover, it is assumed that the inductor voltage and current are sinusoidal with the angular frequency ω. The amplitude voltage across an inductor (V_m) is given by:

$$V_m = \omega * L * I_m = \omega * N * \phi = \omega * N * A_c * B_m \tag{D.1}$$

Where, A_c the cross sectional area of the magnetic core, B_m is the maximum flux density, ϕ is the magnetic flux, L is the inductance and I_m is the maximum current through the inductor.

Therefore from the inductor specifications, the required current rating was calculated as:

$$I_m = \frac{(2500)}{2*\pi*20000*0.000799} = 25.25A.$$

The area product A_p is given by:

$$A_p = A_c * W_a \tag{D.2}$$

Where, W_a is the window area which can be obtained from the selected core dimensions and given as:

$$W_a = \frac{N * A_w}{K_u} \tag{D.3}$$

Where, A_w is the cross sectional area of the winding wire. The amplitude current density through the windings is given by:

$$J_m = \frac{I}{A_w} \tag{D.4}$$

Where I is the *RMS* current. In order to obtain the cross sectional area of the winding wire A_w, the amplitude current density through the windings J_m was chosen to be 4 A/mm^2, Hence, $A_w = 3.004$mm2.

From the previous equations, the area product A_p can be written as:

$$A_p = \frac{L * I_m * A_w}{B_m * K_u} \tag{D.5}$$

Hence,

$$A_p = \frac{(0.799/1000) * 25.25 * (3.004/1000000)}{0.2 * 0.4} * (100)^4 = 75cm^4$$

Six cores of (Ferrites *ETD 59/31/22*, each one have A_p=25.25cm^4) have been chosen to be connected in series in order fulfil the requirements of total A_p =25.25*6=151cm^4 and also to distribute the voltage stress as the applied voltage on the inductor in the *SRSL* converter is equal ($Q*v_o$). Therefore the inductance for each inductor becomes 0.133mH. The ferrite core layout of the *ETD59* is shown in figure E.1.
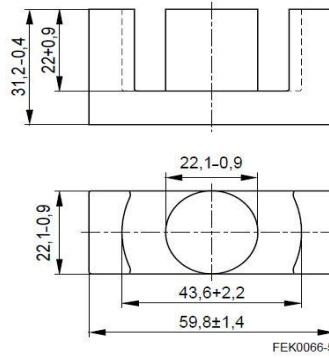
Figure D.1 the ferrite core layout of the *ETD59*

Calculating the number of turn of the winding

By choosing the air gap I_g to be *3mm,* the number of turns required by the inductor is calculated as:

$$N = \sqrt{\frac{L * I_g}{\mu_o * A_c}}$$ (D.6)

Where, $\mu_o = 4 * \pi * 10^{-7}$ H/m is the free space permeability.

Then

$$N = \sqrt{\frac{\frac{0.133}{1000} * \frac{3}{1000}}{4 * \pi * 10^{-7} * \frac{368}{1000000}}} = 29.3$$

It is decided to choose the number of turns N=29 turns. The amount of fringing flux created by the air gap is given by:

$$F = 1 + \frac{I_g}{\sqrt{A_c}} lin(\frac{2G}{I_g})$$ (D.7)

$$F = 1 + \frac{3}{\sqrt{368}} lin(\frac{2 * 44}{3}) = 1.52$$

Where, *G* can be found from core dimensions, in the case of *EDT59* ferrite core G= 2*22*mm* which is the coil length in (*mm*).

By considering the fringing flux, the new number of turns can be calculated as:

157

$$N = \sqrt{\dfrac{L * \dfrac{I_g}{F}}{\mu_o * A_c}} \qquad\qquad (D.8)$$

Then

$$N = \sqrt{\dfrac{\dfrac{0.133}{1000} * \dfrac{3}{(1000)*1.52}}{4*\pi*10^{-7} * \dfrac{368}{1000000}}} = 23.6.$$

As a result, N=24 turns is chosen. This value is reduced when compared with the previous value because of the effect of fringing flux coupling through the inductor winding. In this inductor a copper foil conductor is used in order to reduce the skin-effect.

REFERENCES

[1]   N. Vishwanathan and V. Ramanarayanan, "High voltage DC power supply topology for pulsed load applications with converter switching synchronized to load pulses," in *Power Electronics and Drive Systems, 2003. PEDS 2003. The Fifth International Conference on*, 2003, pp. 618-623 Vol.1.

[2]   F. Carastro, A. Castellazzi, J. Clare, and P. Wheeler, "High-Efficiency High-Reliability Pulsed Power Converters for Industrial Processes," *Power Electronics, IEEE Transactions on,* vol. 27, pp. 37-45, 2012.

[3]   H. Wang, P. Zanchetta, J. Clare, and C. Ji, "Modelling and control of a zero current switching high-voltage resonant converter power supply for radio frequency sources," *Power Electronics, IET,* vol. 5, pp. 401-409, 2012.

[4]   N. Mohan, T. M. Undeland, and W. P. Robbins, *Power electronics : converters, applications, and design / Ned Mohan, Tore M. Undeland, William P. Robbins*: John Wiley & Sons, 2003.

[5]   Marian K. Kazimierczuk and D. Czarkowski., *Resonant power converters*: Hoboken, N.J. : Wiley 2011.

[6]   C. Ji, A. Watson, N. Abodhir, and J. Clare "High Efficiency Operating Point Tracking Techniques for Resonant Power Converters in High Power RF Application " *UK Pulsed Power Symposium,* 2014.

[7]   M. J. Bland, J. C. Clare, P. Zanchetta, P. Wheeler, and J. S. Pryzbyla, "A high frequency resonant power converter for high power RF applications," in *Power Electronics and Applications, 2005 European Conference on*, 2005, pp. 10 pp.-P.10.

[8]   T. S. Wu, M. D. Bellar, A. Tchamdjou, J. Mahdavi, and M. Ehsani, "A review of soft-switched DC-AC converters," in *Industry Applications Conference, 1996. Thirty-First IAS Annual Meeting, IAS '96., Conference Record of the 1996 IEEE*, 1996, pp. 1133-1144 vol.2.

[9]   S. R. Jang, H. J. Ryoo, J. S. Kim, and S. H. Ahn, "Design and analysis of series resonant converter for 30kW industrial magnetron," in *IECON 2010 - 36th Annual Conference on IEEE Industrial Electronics Society*, 2010, pp. 415-420.

[10]   F. Carastro, J. C. Clare, A. Goodman, P. Wheeler, and J. Leach, "Control and implementation of a high voltage series resonant power supply for industrial electrostatic precipitators," in *Energy Conversion Congress and Exposition (ECCE), 2010 IEEE*, 2010, pp. 2797-2802.

[11]   C. Ji, P. Zanchetta, J. Clare, and F. Carastro, "High performance pulsed power resonant converter for radio frequency applications," in *Energy Conversion Congress and Exposition (ECCE), 2011 IEEE*, 2011, pp. 3516-3521.

[12]   W. A. Reass, D. M. Baca, M. J. Bland, R. F. Gribble, H. J. Kwon, Y. S. Cho, D. I. Kim, J. McCarthy, and K. B. Clark, "Operations of polyphase resonant converter-modulators at the Korean Atomic Energy Research Institute," *Dielectrics and Electrical Insulation, IEEE Transactions on,* vol. 18, pp. 1104-1110, 2011.

[13]   T. Filchev, D. Cook, P. Wheeler, A. Van den Bossche, J. Clare, and V. Valchev, "High power, high voltage, high frequency transformer / rectifier for HV industrial applications," in *Power Electronics and Motion Control Conference, 2008. EPE-PEMC 2008. 13th*, 2008, pp. 1326-1331.

[14]   S. R. Jang, S. H. Ahn, H. J. Ryoo, and J. S. Kim, "Design of High-efficiency Soft-switching Converters for High-power Microwave Generation," *Journal of the Korean Physical Society,* vol. 59, pp. 3688-3693, Dec 2011.

[15]   J.T. Bradley, D. Rees, and R.S. Przeklasa, "Design, Construction And Operational Results Of The IGBT Controlled Solid State Modulator High Voltage Power Supply Used In The High Power Rf Systems Of The Low Energy Demonstration Accelerator Of The Accelerator Production Of Tritium (Apt) Project," *Linear Accelerator Conference, 1998*.

[16]   H. Wang and N. University of, *Multivariable state feedback control for resonant long-pulse modulator / Hao Wang*, 2009.

[17]   H. Wang, J. Clare, P. Zanchetta, P. Wheeler, D. Cook, and M. Bland, "State space ZCS control for three-phase resonant converter," in *Industrial Electronics, 2008. IECON 2008. 34th Annual Conference of IEEE*, 2008, pp. 977-982.

[18]   Z. Yingqi and P. C. Sen, "D-Q models for resonant converters," in *Power Electronics Specialists Conference, 2004. PESC 04. 2004 IEEE 35th Annual*, 2004, pp. 1749-1753 Vol.3.

[19]   G. B. Collins., *Microwave magnetrons*: New York : McGraw-Hill,, 1948.

[20]   R. J. Meredith, "Engineers' handbook of industrial microwave heating," *Institution of Electrical Engineers,* 1998.

[21]   A. P. Wynn, D. E. Blank, P. S. Campbell, R. R. Lentz, W. T. Main, S. G. Tantawi, K. G. Kato, H. K. Beutel, K. W. Brown, D. D. Crouch, G. K. Jones, and R. B. McDonald, "Development of a 300 kW CW L-band industrial heating magnetron," in *Vacuum Electronics Conference, 2004. IVEC 2004. Fifth IEEE International*, 2004, pp. 164-165.

[22]   S. R. Jang, H. J. Ryoo, S. H. Ahn, J. Kim, and G. Rim, "Development and Optimization of High-Voltage Power Supply System for Industrial Magnetron," *IEEE Transactions on Industrial Electronics,* vol. 59, pp. 1453-1461, 2012.

[23]   Y. R. Yang, "A magnetron power supply with transition-mode ZVS inverter," in *Power Electronics and Drive Systems (PEDS), 2013 IEEE 10th International Conference on*, 2013, pp. 876-880.

[24]   "e2v," *http://www.e2v.com*.

[25]   S.-K. Kwon, B. Saha, S.-P. Mun, K. Nishimura, and M. Nakaoka, "Series resonant ZCS-PFM DC-DC converter using high frequency transformer parasitic inductive components and lossless inductive snubber for high power microwave generator," *Journal of Power Electronics,* vol. 9, pp. 18-25, 2009.

[26]   B. M. Hasanien and K. F. A. Sayed, "Current source ZCS PFM DC-DC converter for magnetron power supply," in *Power System Conference, 2008. MEPCON 2008. 12th International Middle-East*, 2008, pp. 464-469.

[27]   H. Pfeffer, L. Bartelson, K. Bourkland, C. Jensen, Q. Kerns, P. Prieto, G. Saewert, and D. Wolff, "A Long Pulse Modulator For Reduced Size And Cost," in *Power Modulator Symposium, 1994., Twenty-First International*, 1994, pp. 48-51.

[28]   D. A. Jones, T. P. Lelyveld, S. D. Mavrofidis, S. W. Kingman, and N. J. Miles, "Microwave heating applications in environmental engineering—a review," *Resources, Conservation and Recycling,* vol. 34, pp. 75-90, 2002.

[29]   W. A. G. Voss, "Industrial Microwave Applications," in *Microwave Conference, 1974. 4th European*, 1974, pp. 16-25.

[30]   M. S. Shaheen, A. H. El-Ghorab, F. M. Anjum, and K. F. El-Massry, *Microwave applications in thermal food processing*: INTECH Open Access Publisher, 2012.

[31]   H. Ramaswamy and J. Tang, "Microwave and radio frequency heating," *Food Science and Technology International,* vol. 14, pp. 423-427, 2008.

[32]   E. Binner, E. Lester, S. Kingman, C. Dodds, J. Robinson, T. Wu, P. Wardle, and J. P. Mathews, "A Review of Microwave Coal Processing," *Journal of Microwave Power and Electromagnetic Energy,* vol. 48, pp. 35-60, 2014.

[33]   J. Robinson, E. Binner, A. Saeid, M. Al-Harahsheh, and S. Kingman, "Microwave processing of Oil Sands and contribution of clay minerals," *Fuel,* vol. 135, pp. 153-161, 2014.

[34]   J. P. Robinson, S. W. Kingman, C. E. Snape, R. Barranco, H. Shang, M. S. A. Bradley, and S. M. Bradshaw, "Remediation of oil-contaminated drill cuttings using continuous microwave heating," *Chemical Engineering Journal,* vol. 152, pp. 458-463, 2009.

[35]   R. G. Carter, "Acceleration technologies for charged particles: an introduction," *Contemporary Physics,* vol. 52, pp. 15-41, 2011.

[36]   R. Electronics. (2013). *http://www.rell.com/microwave.html*.

[37]   J. Eckoldt, "Long Pulse Modulators," 2015.

[38]   A. Watson, C. Ji, J. Clare , P. Wheeler , E. Moraga-Reyes , and N. Abodhir, "Resonant Power Electronics for Pulsed Power and High Voltage Applications," *UK Pulsed Power Symposium, 2014*.

[39]   D. J. Cook, M. Catucci, J. C. Clare, P. Wheeler, and J. Przybyla, "Design of A Direct Converter for High Power, RF Applications," in *Particle Accelerator Conference, 2005. PAC 2005. Proceedings of the*, 2005, pp. 4033-4035.

[40]   B.-M. Song, M.-H. Kye, and R.-Y. Kim, "Design of a cost-effective DC-DC converter with high power density for magnetron power supplies," in *Power Electronics Conference (IPEC), 2010 International*, 2010, pp. 137-141.

[41]   M. Bland, J. Clare, P. Wheeler, and B. Richardson, "A 25kV, 250kW Multiphase Resonant Power Converter for Long Pulse Applications," in *Plasma Science, 2007. ICOPS 2007. IEEE 34th International Conference on*, 2007, pp. 944-944.

[42]   E. Reyes-Moraga, A. Watson, J. Clare, and P. Wheeler, "Predictive control of a direct resonant converter with output voltage compensation for high voltage DC power supply applications," *Power Electronics and Applications (EPE), 2013 15th European Conference on,* 2013

[43]   U. Mumtahina and P. Wolfs, "A comparison study between series resonant and zero-voltage-resonant-transition DC-DC converters," in *Power Engineering Conference (AUPEC), 2015 Australasian Universities*, 2015, pp. 1-6.

[44]   M. M. Walters and W. M. Polivka, "Extending the range of soft-switching in resonant-transition DC-DC converters," in *Telecommunications Energy Conference, 1992. INTELEC '92., 14th International*, 1992, pp. 343-350.

[45]   J. Lu, D. J. Perreault, D. M. Otten, and K. K. Afridi, "Impedance Control Network Resonant DC–DC Converter for Wide-Range High-Efficiency Operation," *IEEE Transactions on Power Electronics,* vol. 31, pp. 5040-5056, 2016.

[46]   " Parasitic Capacitance Effects in Step-Up Transformer Design," *www.linear.com/docs/4131*, 1990.

[47]   Y. A. Ang, D. Stone, C. Bingham, and M. Foster, "Rapid Analysis Design Methodologies of High-Frequency LCLC Resonant Inverter as Electrodeless Fluorescent Lamp Ballast," in *2007 7th International Conference on Power Electronics and Drive Systems*, 2007, pp. 139-144.

[48]   C. M. Bingham, Y. A. Ang, M. P. Foster, and D. A. Stone, "Analysis and Control of Dual-Output Resonant Converters With SignificantLeakage Inductance," *IEEE Transactions on Power Electronics,* vol. 23, pp. 1724-1732, 2008.

[49]   A. Kasliwal, R. Banwari, S. Kotaiah, T. Pandit, and A. Upadhyay, "Utilizing Multiplier Stack's Reflected Parasitic Capacitance to Achieve ZVS Operation of Resonant."

[50]   T. B. Soeiro, M. J, hlethaler, J. Linn, P. Ranstad, and J. W. Kolar, "Automated Design of a High-Power High-Frequency LCC Resonant Converter for Electrostatic Precipitators," *IEEE Transactions on Industrial Electronics,* vol. 60, pp. 4805-4819, 2013.

[51]   H. Q. S. Dang and N. University of, *A new implementation of high frequency, high voltage direct power converter / by Dang Huy Quoc Si*, 2006.

[52]   H. Sarnago, O. Lucia, A. Mediano, and J. M. Burdio, "Efficient and Cost-Effective ZCS Direct AC–AC Resonant Converter for Induction Heating," *IEEE Transactions on Industrial Electronics,* vol. 5, pp. 2546-2555, 2014.

[53]   P. W. Wheeler, J. Rodriguez, J. C. Clare, L. Empringham, and A. Weinstein, "Matrix converters: a technology review," *IEEE Transactions on Industrial Electronics,* vol. 49, pp. 276-288, 2002.

[54]   L. Hao Leo, A. P. Hu, and G. A. Covic, "A Direct AC-AC Converter for Inductive Power-Transfer Systems," *Power Electronics, IEEE Transactions on,* vol. 27, pp. 661-668, 2012.

[55]   M. J. Bland, J. C. Clare, and P. Wheeler, "Multiphase Resonant Power Converter for Long Pulse Applications," in *Pulsed Power Symposium, 2006. The Institution of Engineering and Technology*, 2006, pp. 19-23.

[56]   C. Ji, P. Zanchetta, F. Carastro, and J. Clare, "Repetitive Control for High Performance Resonant Pulsed Power Supply in Radio Frequency Applications," *Industry Applications, IEEE Transactions on,* pp. 1-1, 2013.

[57]   !!! INVALID CITATION !!!

[58]   S. N. Biju and S. Indian Institute of, *Analysis, simulation and design of series resonant converter for high voltage applications*, 1999.

[59]   A. D. Andreev and K. J. Hendricks, "Particle-in-cell (PIC) simulation of CW industrial heating magnetron," *Journal of Microwave Power and Electromagnetic Energy,* vol. 44, pp. 114-124, 2010.

[60]   A. S. Gilmour and I. ebrary, *Klystrons, traveling wave tubes, magnetrons, crossed-field amplifiers, and gyrotrons [electronic resource] / A.S. Gilmour*: Artech House, 2011.

[61]   M. J. Bland, J. C. Clare, P. Wheeler, and R. Richardson, "A 25kV, 250kW multiphase resonant power converter for long pulse applications," in *Pulsed Power Conference, 2007 16th IEEE International*, 2007, pp. 1627-1630.

[62]   T. Soeiro, J. Biela, M. J, x00Fc, hlethaler, J. Linn, x00E, P. Ranstad, and J. W. Kolar, "Optimal design of resonant converter for Electrostatic Precipitators," in *Power Electronics Conference (IPEC), 2010 International*, 2010, pp. 2294-2301.

[63]   P. Ranstad, H. P. Nee, and J. Linner, "A novel control strategy applied to the series loaded resonant converter," in *Power Electronics and Applications, 2005 European Conference on*, 2005, pp. 10 pp.-P.10.

[64]   H. Kifune, Y. Hatanaka, and M. Nakaoka, "Cost effective phase shifted pulse modulation soft switching high frequency inverter for induction heating applications," *Electric Power Applications, IEE Proceedings -,* vol. 151, pp. 19-25, 2004.

[65]   S. Pholboon, "A resonant power converter for DC magnet power supply applications " *University of Nottingham,* 2012.

[66]   N. Abodhir, A. Watson, and J. Clare, "Control of HV Series Resonant Power Supply for Industrial Magnetrons," *IET-PEMD 2014*.

[67] T. R. McComb, "A Test to Measure the Effect of Self-Heating on the Scale Factor of a Measuring System for High Direct Voltage Based on a Resistor Divider," in *Precision Electromagnetic Measurements Digest, 2004 Conference on*, 2004, pp. 573-574.

[68] M. Tomse, N. D. Trip, A. Schiop, and C. Gordan, "Modeling and Simulation of a Series Resonant Inverter," in *EUROCON, 2007. The International Conference on "Computer as a Tool"*, 2007, pp. 1512-1517.

[69] Y. Sihun, K. Goto, Y. Imamura, and M. Shoyama, "Dynamic characteristics model of bi-directional DC-DC converter using state-space averaging method," in *Telecommunications Energy Conference (INTELEC), 2012 IEEE 34th International*, 2012, pp. 1-5.

[70] E. van Dijk, J. N. Spruijt, D. M. O'Sullivan, and J. B. Klaassens, "PWM-switch modeling of DC-DC converters," *Power Electronics, IEEE Transactions on,* vol. 10, pp. 659-665, 1995.

[71] W. Siu-Chung and A. D. Brown, "Analysis, modeling, and simulation of series-parallel resonant converter circuits," *Power Electronics, IEEE Transactions on,* vol. 10, pp. 605-614, 1995.

[72] Seddik Bacha, Iulian Munteanu, and A. I. Bratcu., "Power electronic converters : modeling and control," 2014.

[73] M. Z. Youssef and P. K. Jain, "Sampled Data Model for a Self-oscillating Series-parallel Resonant Converter with the Parasitic Effects in the Clamped and Unclamped Conduction Modes," in *Power Electronics Specialists Conference, 2005. PESC '05. IEEE 36th*, 2005, pp. 1037-1045.

[74] R. Oruganti and F. C. Lee, "Resonant Power Processors, Part I---State Plane Analysis," *Industry Applications, IEEE Transactions on,* vol. IA-21, pp. 1453-1460, 1985.

[75] A. S. Nise, "Control Systems Engineering, Sixth Edition," *JohnWiley & Son,2011.*

[76] R. C. D. a. R. H. Bishop, *Addison Wesley Longman, 1998.,* Modern Control Systems, Eighth Edition.

[77] J. D. P. Gene F. Franklin, Abbas Emami-Naeini., "Feedback control of dynamic systems," 2015.

[78] M. K. Kazimierczuk and H. Sekiya, "Design of AC resonant inductors using area product method," in *Energy Conversion Congress and Exposition, 2009. ECCE 2009. IEEE*, 2009, pp. 994-1001.